A Study of The Correspondence Problem and Relevant Applications in Computer Vision and Graphics

by

Somenath Das

(Under the Direction of Suchendra M. Bhandarkar)

Abstract

Correspondence determination between different objects plays a pivotal role in a wide range of applications in the field of computer vision and computer graphics. In this dissertation, we address some key problems in computer vision and computer graphics that are dependent on accurate correspondence determination between the underlying objects under consideration. Following a general introduction to the correspondence problem in Chapter 1, in Chapter 2, we introduce a pairwise geodesic distance-based global shape representation for 3D shapes and employ the spectrum of this representation to address correspondence determination between isometric 3D shape pairs, self-symmetry detection and detection of stable regions within 3D shapes. A surface differential-oriented global shape representation is introduced in Chapter 3 and the spectrum of this representation is further employed for symmetry detection and correspondence determination

between isometric 3D shapes. Furthermore, a novel criterion is introduced to measure the compatibility of the representation spectrum in the context of deformation transfer.

In Chapter 4, we present a comparative study of the performance of the shape representations introduced in Chapters 2 and 3 in the presence of noise. We also introduce a novel shape representation spectrum based surface point feature. In addition, in chapter 4 we employ the spectrum of the proposed shape representation to address deformation transfer between a source and a target shape.

In Chapter 5, we address non-rigid structure from motion, a very important problem in computer vision, that estimates 3D information from a 2D image sequence. To address this problem we impose a constraint on the distribution of the 2D correspondences between consecutive frames of the temporal image sequence. Finally, we conclude in Chapter 6 by giving an outline of some possible direction towards future extensions of the works presented.

All the problems and applications of computer vision and computer graphics considered in this dissertation, are influenced by accurate correspondence determination between the different objects under consideration. The results of the proposed framework in each chapter are compared to those from other relevant state-of-the-art schemes. It is shown that the proposed schemes perform competitively when compared with their state-of-the-art counterparts.

INDEX WORDS: Computer Vision, Computer Graphics, Shape analysis, Symmetry detection, Correspondence problem, Non-Rigid Structure from Motion

A Study of The Correspondence Problem and Relevant Applications in Computer Vision and Graphics

by

Somenath Das

B.Tech., West Bengal University of Technology, 2006

M.E., Jadavpur University, 2012

A Dissertation Submitted to the Graduate Faculty

of The University of Georgia in Partial Fulfillment

of the

Requirements for the Degree

Doctor of Philosophy

Athens, Georgia

2018

A Study of The Correspondence Problem and Relevant Applications in Computer Vision and Graphics

by

Somenath Das

Approved:

Major Professor: Suchendra M. Bhandarkar

Committee: Liming Cai
Khaled Rasheed

Electronic Version Approved:

Suzanne Barbour
Dean of the Graduate School
The University of Georgia
August 2018

A Study of The Correspondence Problem and Relevant Applications in Computer Vision and Graphics

Somenath Das

August 2018

I have known love through my family. My Masterpiece, will be dedicated to them.

I dedicate this work, which I consider a stepping stone, to myself.

Acknowledgments

My life is indebted so much to so many people for so many reasons that a mere formal Acknowledgement seems to be an injustice to them, like a cold business transaction, without conveying the much needed human emotion behind it. However, it is my responsibility to convey my gratitude to those, without whom the work described in this dissertation would not have been completed.

First, let me convey my sincere gratitude to Dr. Suchendra M. Bhandarkar for allowing me pursue an independent research area. Without his guidance and encouragement my training as an independent researcher would have been incomplete. I thank all the faculties and stuff of the Department of Computer Science for their dedicated support towards making a student's academic pursuit pleasurable. I convey my gratitude to Dr. Ananda Shankar Chowdhury of Jadavpur University for being a constant source of inspiration and guidance. I thank specially all the members of my lab, Mr. Arun Kumar Chockalingam Santhakumar, Mr. Manu Nair, Dr. Karan Sharma, and lab alumni Dr. Kyle Krafka and Dr. Anirban Mukhopadhyay for their support, and intellectual contributions towards my research. Thanks Anne Steward for each time you provided us with much needed

technical support with an ever friendly smile. Thanks to Samantha Varghese for handling the student's requirement so efficiently.

The UGA Science and General library is a treasure trove of knowledge with virtually all the books one might need for the quest of knowledge. I convey my sincere gratitude to all the library members for their support. In the end, I also acknowledge the memory of many pleasurable evenings spent with my Dell Inspiron workstation in the VPCL lab without which I could not have known the pleasure of computing.

Contents

List of Figures

List of Tables

Chapter 1

Introduction and Literature Review

Establishing meaningful correspondence between analyzable objects is central to many applications within the fields of computer vision and graphics. The correspondence problem had been well studied in the context of image analysis, shape analysis, statistical modeling of objects, and even within some pure mathematical disciplines such as Algebraic Topology and Algebraic Geometry. The principle underlying correspondence models varies depending on the application objectives. The objects analyzed by a correspondence problem formulation vary depending on the context of the underlying application area. For instance, 3D shapes are examples objects analyzed by a correspondence problem formulation in computer graphics applications whereas in context of computer vision the objects are images or image streams. This dissertation is a study of the correspondence problem in the context of applications in the fields of computer graphics and computer vision. The correspondence problem in computer graphics applications deals primarily

with points on a 3D shape, or a region map between 3D shapes. This dissertation proposes novel shape representations or shape descriptors that address the correspondence problem by formulating a spectral structure for the 3D shapes under consideration. Furthermore, the study also explores associated applications of the correspondence problem using the proposed representations. In addition, the shape representation is exploited to represent correspondence between 2D images to address Non-Rigid Structure from Motion (NRSfM), a central problem in the field of computer vision.

Sampled features are quintessential in establishing meaningful correspondence between objects. The concept of a *feature* is very general and varies widely across applications. However, in the context of correspondence determination between shapes, features may refer to specific structures imposed upon the shape such as local geometry sampled at specific points, whereas in image-oriented applications, features could indicate low-level pixel cues, or higher-level edges and orientation information. In most of the related applications in computer graphics and vision a higher level mathematical structure, namely, a shape descriptor is widely used to represent and process the accumulated object features in a meaningful way so that an optimized correspondence is achieved.

In this chapter a brief introduction to shape descriptors is provided along with a survey of the most salient applications of correspondence determination that are supported by these shape descriptors. Since shape descriptors primarily influence many applications in computer graphics, the focus of the survey will be confined within the scope of computer graphics. This chapter is concluded with a brief

survey of the NRSfM problem in computer vision citing the most prominent works in the field, especially those that have influenced the present optimization structure for NRSfM, and are supported by the shape representations proposed in this dissertation.

1.1 Shape Descriptors and Applications

In the context of computer graphics the objects of interest, i.e., 3D shapes, are represented as 3D point clouds or triangulated meshes that are assumed to provide explicit low-level geometric information. However, low-level information alone is not discriminating enough for a wide range of shapes varying in size, geometry, and critical topological detail. Therefore it is infeasible to use low-level geometric information explicitly to represent a 3D shape within a general parameterized space. However, shape descriptors can be employed for the purpose of categorizing surface regions of 3D shapes to facilitate different applications in 3D shape analysis.

One desirable property of a shape descriptor is the ability to capture capture the unique properties of the underlying 3D shape surface while providing robustness or invariance to undesirable local geometric perturbations. The feature information that is unique to the localized surface region, are represented by the shape descriptor over the 3D shape can be used to establish correspondence between surface regions of different shapes. There exist several variations of the correspondence model in the literature Van Kaick et al. [2011a] that differ widely from each other, both in regard to the underlying principle and types of shape

descriptors used. Particularly in context of a 3D shape a useful shape descriptor should capture the local geometric changes over the global shape faithfully such that it can be used to recognize the corresponding surface region between shapes even after it has undergone considerable local geometric changes under noise. It should represent faithfully the given local geometry of the 3D shape and be robust to noise and sampling errors. The other sources of error a robust descriptor should consider are geometric noise caused by changes in mesh topology, mesh connectivity noise, and global topology noise (imposed on the mesh by creation of loops and tunnels, Heider et al. [2011a]). The existing surface descriptors in the literature can be categorized into different classes based on the manner in which they construct and evaluate a local neighborhood around a sample point (i.e., whether they consider local surface data or global surface data). Note that the term *surface data* is dependent on the choice of distance metric defined between surface vertex pairs over the shape.

Shape descriptors play a fundamental role in addressing the correspondence problem in shape analysis. In Figure 1.1, the gradual development in the models used to establish correspondence is depicted. Methods to establish correspondence between rigid shapes are relatively well explored and benefit from mathematically well defined objective functions. The deformations the objects in this category can undergo are affine in nature and thus have a pure geometric formulation. Correspondence between shapes, that might not be rigid but isometric to each other can also be addressed by solving purely a geometric optimization problem. Therefore, recent research on the above shape categories focuses on improving efficiency and

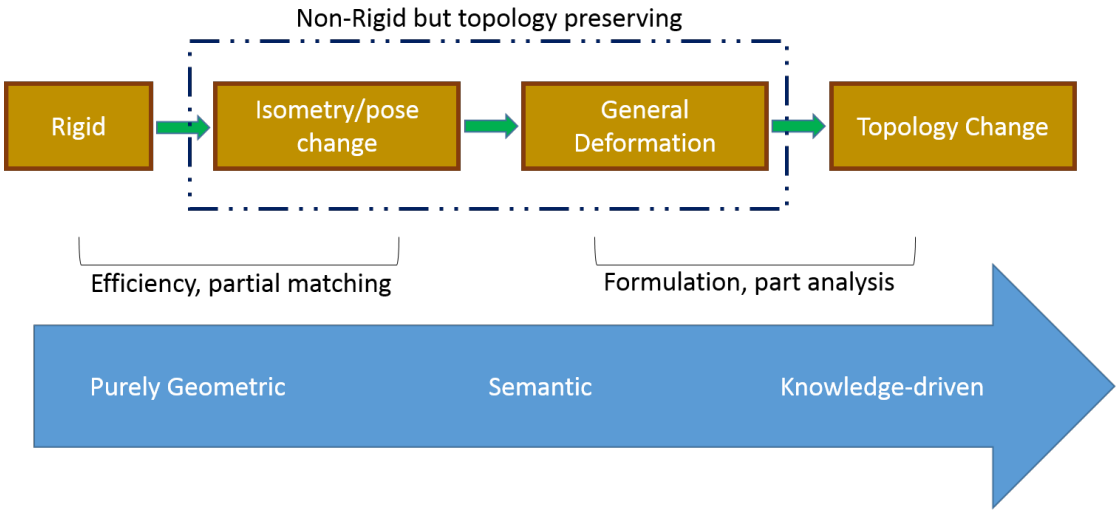

Figure 1.1: Evolving shape correspondence models. Van Kaick et al. [2011a]

accuracy of correspondence determination and/or focuses on a difficult subproblem such as partial shape matching. Establishing correspondence between shapes belonging to the same category but differing significantly in geometry, topology, and structure, however, remains a challenge. The optimization criteria used in establishing correspondence between these shapes cannot depend simply upon pure geometric features, thus shifting the definition of the correspondence determination problem towards hypothesis-oriented approaches. These approaches utilize a combination of higher- and lower-level information to address *semantic* aspects of a 3D shape based on the presence of heterogeneous surface segments, geometric and topological characterization of the surface, and ontology modules designed specifically for a certain genre of shapes. A lot of emphasis is laid upon utilizing prior learned information for establishing meaningful correspondence. This is

reflected in the recent increased attention towards learning-based models such as Kalogerakis et al. [2010]; Van Kaick et al. [2011b] for determining correspondence.

In this section, following a brief discussion on some of the applications of correspondence problem we briefly highlight the different categories of shape descriptors that vary in their underlying principle. The description of these applications also indicate the close relation between the application goal and the desirable properties of the adopted shape descriptor. The principles governing the properties of the shape descriptors used for each of the following applications are derived from spectral analysis of the shape descriptor. The motivation behind this brief survey is to demonstrate the effectiveness of spectrum based shape descriptors in correspondence related applications.

1.1.1 Applications of Correspondence Problem

The following applications are connected in terms of the principles of the underlying shape descriptors used. All of the cited applications rely, to varying degrees, on the spectral analysis of the underlying shape descriptors.

Shape registration

From an initial set of scans of a 3D object from arbitrary positions, a registration process matches corresponding regions across the scans (Van Kaick et al. [2011a]). The final target 3D object is reconstructed using the alignment between the corresponding regions. Shape registration has two different categories; in rigid registration (Rusinkiewicz and Levoy [2001]), shapes do not change during the scanning

process whereas in case of non-rigid registration (Anguelov et al. [2005]; Jain et al. [2007]; Brown and Rusinkiewicz [2007]; Chang and Zwicker [2008]; Huang et al. [2008]), the 3D shapes are free to deform between successive surface scans.

Shape interpolation/morphing

In shape interpolation or shape morphing, one shape is gradually transformed into another. The transformation has to be gradual between successive interpolated shapes, i.e. the shape transformation procedure should have a sense of continuity imposed upon interpolated shapes to create a visually pleasing aspect(Alexa [2002]). The correspondence model can address sparse or dense point correspondence between source and target shapes(Kraevoy and Sheffer [2004]). However, the correspondence between reference and target shape should retain a semantic equivalence between different parts of the shapes.

Symmetry detection

Detecting symmetries within a 3D shape can further be very effectively used for various mesh editing applications within a geometry processing pipeline such as registration, segmentation, compression and modeling (Golovinskiy et al. [2009]). Detecting symmetry within a shape is equivalent to finding correspondence between elements of the same shape. Computationally, this task is to determine a set of non-mutative transformations that, when applied over the shape, do not modify its geometry. The transformations used for symmetry detection methods can be extrinsic (Mitra et al. [2006]; Podolak et al. [2006]), intrinsic (Xu et al.

[2009]; Kim et al. [2010]), or may utilize spectral embeddings(Ovsjanikov et al. [2008]; Lipman et al. [2010a]).

Information transfer

Attributes or features of a shape, if efficiently reused, can reduce the computational overhead for many graphics pipeline operations such as continuous modeling of shapes widely used in animation industry. To facilitate attribute reusability, information transfer is becoming a common task across various graphics pipelines. The information may refer to the deformation (Sumner et al. [2005]), style(Xu et al. [2010]), or the texture(Dinh et al. [2005]) defined on the source shape. The usefulness of a robust correspondence model is evident for this class of tasks since the attribute on the source mesh can only be transferred to target mesh through a well defined set of point or region correspondences between the source and target shapes.

Recognition and retrieval

Scene understanding and object recognition from range images is a central problem in computer vision (Forsyth and Ponce [2003]). Spectral model based shape correspondence can be effectively used for this task. Based on a combination of dominant basis shapes derived from the spectral analysis of a query shape one can recognize the existence and location of the query shape embedded within a given 3D scene. For determining the confidence level of the recognition task a certain measure of correspondence quality between the query shape and retrieved shape

model is necessary. This principle is generally used for retrieving a shape within a scene as well (Funkhouser and Shilane [2006]).

Time varying surface reconstruction

Surface reconstruction pipeline refers to the task of reconstructing a 3D surface from a temporally related scans of a rigid or non-rigid 3D model. For a non-rigid model the surface can deform between successive scans following a free-form transformation. The final task is to combine the scans into a 3D surface model. A robust correspondence model is central to this family of tasks since since the points based correspondence across scans needed to be finally mapped to the reconstructed 3D surface. Some of relevant works in this field are due to Mitra et al. [2007]; Wand et al. [2007]; Sharf et al. [2008]; Pekelny and Gotsman [2008]; Li et al. [2009]; Chang and Zwicker [2009]; Tevs et al. [2009]; Zheng et al. [2010].

Change detection

Correspondence determination can be applied to track changes in a shape (e.g., displacements or growth) over time. For example, tracking organ deformation to infer the nature of a disease is particularly useful in diagnostic medicine. One relevant medical application is to track the changes in the number and density of moles on a patient's skin for the purpose of cancer prediction (Mirzaalian et al. [2009]). Change detection can also be used in remote sensing, where tracing variation in city layout with land usage is useful for efficient city planing(Leclerc et al. [2000]).

Statistical shape modeling

Shape recognition and shape retrieval under different degrees of variability in form, size and appearance are important tasks in anatomical studies where the target shapes are human organs or bones. A statistical 3D model with a measurable degree of deformation for different regions is suitable for tasks such as retrieval of objects within a image. Formation of a 3D statistical model is typically done by optimizing the correspondence between different shapes having a common structure (Davies et al. [2008]; Hasler et al. [2009]; Ward and Hamarneh [2007]).

1.2 Shape Descriptors

A shape descriptor may be local or global depending on the the features it computes over the shape. In this section, a brief survey of the some prominent shape descriptors from each family is provided. It is to be emphasized that these descriptors are useful in the context of correspondence based computer graphics applications as mentioned in Section. 1.1.

Local shape descriptors can be categorized into different classes based on their approach towards the encoding of the underlying local surface geometry. One prominent category is **ring-based descriptors** that typically employ a parametrically controlled surface metric based on geometric object such as *blowing bubbles* (Mortara et al. [2004]) or geodesic diameter (Pottmann et al. [2009a]). Some variants within this class use surface normal vectors as local surface features computed at discrete points on the surface mesh (Gatzke et al. [2005]; Stein and

Medioni [1992]; Ong and Seghouane [2011a]). These descriptors typically employ an external frame of reference over the mesh Yamany and Farag [1999]; Chua and Jarvis [1997]; Yamany and Farag [2002] or auxiliary geometric parameter such as local surface curvature Gatzke et al. [2005]; Ong and Seghouane [2011b] to compute the local surface feature. **Expanding descriptors**, on the other hand fit a hypothesis-based parametric model where the sampled feature values are considered as parameters. These descriptors commonly employ features such as geodesic distance (Mortara et al. [2004]; Cipriano et al. [2009]), volume or surface area (Connolly [1986]; Pottmann et al. [2009b]) to characterize a local surface region. Some variants of *Expanding Descriptors* use measures such as mesh smoothing (Li and Guskov [2005]) or mesh saliency (Lee et al. [2005]) to sample local surface features. **Iterative operator-based descriptors** capture local geometric changes within a surface region by manipulating the entire mesh using strategies such as smoothing (Li and Guskov [2005]), estimation of local diffusion geometry (Bronstein et al. [2010]) over the mesh surface, or diffusion based variation (Rustamov [2007]) within the surface mesh.

A **global shape representation** is important to effectively characterize the global shape and determine the correspondence between shapes. However, typically a global shape representation represents a global shape by collectively representing local sampled features. A variation in this trend, i.e., surface descriptors based on the eigenspectrum of the Laplace-Beltrami operator, have gained popularity in the context of the correspondence problem due their natural robustness to noise and their flexibility in dealing with surface perturbations. Some well

known surface descriptors from this class employ a Laplace-Beltrami operator-guided spectral process that samples geometry by computing the distance between surface points using a distance metric. Variants within this class of descriptors employ a mesh connectivity based surface metric along the geodesic curves on the 3D surface mesh (Rustamov [2007]) or diffusion geometry (Bronstein et al. [2010]) over the surface to measure the point-to-point length along a specific path on the surface mesh. Smeets et al. [2012] present a geodesic distance-based global shape representation that demonstrates robustness to nearly isometric deformations. Surface point signature based shape descriptors based on the *heat kernel signature* (HKS) due to Sun et al. [2009]; Bronstein and Kokkinos [2010]; Boscaini et al. [2016] employ the heat diffusion model in conjunction with the eigenspectrum of the Laplace-Beltrami operator to characterize the global shape. The other well known variant of point signature based shape descriptor is *wave kernel signature* (WKS) proposed by Aubry et al. [2011] that employs the principles of quantum mechanics, in conjunction with the Laplace-Beltrami eigenspectrum to characterize the 3D shape.

1.3 Correspondence for Non-Rigid Structure from Motion

Non-Rigid Structure from Motion (NRSfM hereof) refers to the problem of recovering 3D shape information from 2D image streams, typically a video sequence. The state-of-the-art approaches for such a problem depend upon accurate point-based correspondence determination between consecutive image frames. Seminal work

in this field by Bregler et al. [2000] determines correspondence across the video frames by factorizing the accumulated data into camera pose and 3D shape space to achieve final reconstruction of 3D shapes. Single value decomposition (SVD) based factorization methods (Akhter et al. [2009a]; Yan and Pollefeys [2008]; Bartoli et al. [2008]) for NRSfM have gained much attention due to the simplicity and robustness of the underlying assumption that temporally related object data cannot deform arbitrarily. Specialized variants of these methods have been proposed to recover shape data for articulated objects such as the human model (Tresadern and Reid [2005]; Paladini et al. [2009]). To address 3D shape recovery in the presence of deformation with high variance, particular attention has been given to introduce statistical(Torresani et al. [2008]), shape basis (Xiao et al. [2006]), and 3D affine priors (Del Bue [2008]) that could be combined with the factorization method as well. In this dissertation we explore a novel correspondence based factorization method, in conjunction with motion constraints imposed upon the deformable object, to enhance the accuracy of the final 3D shape reconstruction.

Chapter 2

Local Geometry Inclusive Global Shape Representation

Somenath Das[1], Dr. Suchendra M. Bhandarkar

[1]First Author. Accepted by Proceedings of International Conference of Computer Vision 2017 (ICCV) workshops, Reprinted here with permission of publisher, October, 2017

2.1 Abstract

In this chapter, a local geometry-inclusive global representation of 3D shapes based on the shortest quasi-geodesic paths between all possible pairs of points on the shape manifold is proposed. In the proposed representation, the normal curvature values along the quasi-geodesic paths are shown preserve the local shape geometry. The eigenspectrum of the proposed global representation is exploited to characterize the shape self-symmetry. The commutative property of the shape descriptor spectrum is exploited to address region-based correspondence determination between isometric 3D shapes without requiring prior correspondence maps and to extract stable regions between 3D shapes that differ from one another by a high degree of isometry transformation. eigenspectrum-based characterization metrics are proposed to quantify the performance of the proposed 3D shape descriptor for correspondence determination and self-symmetry detection in comparison to its relevant state-of-the-art counterparts. The proposed shape descriptor spectrum and the optimization criterion based on spectral commutativity are observed to yield competitive performance compared to relevant state-of-the-art methods.

2.2 Introduction

In the field of shape analysis, the computation of an optimal global description of a 3D shape is critically dependent upon the underlying application. Applications based on shape similarity computation typically rely on a suitably formulated global metric to characterize shape similarity. On the other hand, local shape

geometry is important for applications where it is essential to establish point-to-point correspondence between candidate shapes. Based on the objective(s) of the application and nature or modality of the underlying shape data/information (i.e., geometric, topological, etc.), 3D shape analysis applications can be broadly categorized as purely geometric, semantic or knowledge-driven Van Kaick et al. [2011a]. However, a large number of 3D shape analysis applications that belong to these categories or lie within their intersections are compelled to address a fundamental problem, i.e., that of determining accurate correspondence between the 3D shapes under consideration. Typical examples of such applications include rigid and non-rigid shape registration (Chang and Zwicker [2008]; Gelfand et al. [2005]), shape morphing (Kraevoy and Sheffer [2004]), self-symmetry detection (Gal and Cohen-Or [2006]), shape deformation transfer (Sumner and Popović [2004]), 3D surface reconstruction (Pekelny and Gotsman [2008]), shape-based object recognition and retrieval (Jain and Zhang [2007]), to name a few. In each of the aforementioned applications, shape descriptors play a critical role in determining the required 3D shape correspondence. Depending on the nature of the application, 3D shape descriptors could be purely geometric and used to capture the *local* 3D geometry of the shapes whereas others may incorporate prior knowledge about the *global* 3D shape. Ideally, a 3D shape descriptor should demonstrate robustness to topological noise while simultaneously capturing the underlying invariant shape features that are useful in computing the correspondence between 3D shapes.

In this chapter, we address an important problem, i.e., that of determining correspondence between isometric 3D shapes (i.e., 3D shapes that have undergone

isometry deformation or transformation with respect to each other) *without* requiring any prior knowledge about the underlying shapes. To this end, we propose a 3D shape descriptor based on estimation of the approximate geodesic distance between all point pairs on the 3D shape manifold. The proposed representation is used to address the computation of 3D self-symmetry, determination of correspondence between isometric 3D shapes and detection of the most stable parts of the 3D shape under varying degrees of isometry (i.e, non-rigid pose) transformation between shapes. Since the geodesics over a 3D shape manifold are defined as surface curves of constant normal curvature, they are observed to naturally encode the local surface geometry along the curve. On a discrete triangulated 3D surface mesh, the discrete approximation to a geodesic is characterized by an optimal balance of the distribution of angles on either side of the discrete geodesic computed over the local neighborhood of each mesh point on the geodesic as depicted in Figure 2.2. This balance of the local angular distribution is observed to encode the local geometry of the triangulated mesh along the discrete geodesic. The aforementioned approximation to a geodesic computed over a discrete 3D triangulated mesh is referred to as a *quasi-geodesic* cf. Martínez et al. [2005]. The proposed global shape descriptor represents the 3D shape by computing the quasi-geodesic paths between all point pairs on the discrete 3D triangulated surface mesh.

The all-point-pairs geodesic matrix representation of 3D shapes displays a symmetrical pattern as shown in Figure 2.1. We employ the eigenspectrum of this representation to detect self-symmetry within a shape. Furthermore, we investigate the commutative property of the eigenvectors of the shape descriptor spectrum,

which are shown to be approximately orthogonal to each other, for discrete settings such as the triangulated mesh-based representations of 3D shapes. Approximate orthogonality refers to the fact that for two distinct eigenvectors of the shape descriptor spectrum ϕ_i and ϕ_j (where $i \neq j$), $|\langle \phi_i, \phi_j \rangle| < \epsilon$ where $\langle \cdot, \cdot \rangle$ denotes the scalar inner product of the vector arguments and $\epsilon \approx 0$. It should be noted that the eigenspectrum of the proposed representation is distinct from the well known Laplace-Beltrami eigenspectrum that has been used extensively in several 3D shape analysis and 3D shape synthesis applications. In our case, we exploit the commutative property of the shape descriptor eigenspectrum to establish the correspondence between isometric 3D shapes. It should also be emphasized that, unlike many related approaches (Kovnatsky et al. [2013]; Ovsjanikov et al. [2012]), the proposed optimization criterion used to establish the correspondence between isometric 3D shapes does not exploit nor require prior user-specified correspondence maps between the 3D shapes.

We use the proposed correspondence optimization scheme to test the hypothesis that the presence of implicit isometry between 3D shapes can be characterized using a global quasi-geodesic-based shape representation that encodes local shape geometry. Furthermore, we also contend that the proposed representation can be exploited to address problems such as self-symmetry detection and characterization, correspondence determination and stable part or region detection under isometry deformation without resorting to prior knowledge of correspondence maps. To the best of our knowledge, the problem of correspondence determination in the absence of prior knowledge had not been addressed in the research

literature. In some of our experiments, we obtain poor results for correspondence determination as a consequence of not requiring any prior knowledge in the face of high variability in the isometry transformations. However, our experiments show that the proposed correspondence determination technique is able to detect stable corresponding parts or regions between shapes, i.e., corresponding parts or regions that have undergone the least degree of isometry deformation (Section 2.6).

The remainder of the chapter is organized as follows. In Section 2.3, we present a brief survey of the most relevant works on 3D shape description that can be effectively used to address 3D shape correspondence determination with an added emphasis on related work on coupled quasi-harmonic bases by Kovnatsky et al. [2013]. Section 2.4 describes the specific contributions of our work. The mathematical model on which the proposed technique is based is detailed in Section 2.5. In Section 2.6, we present the experimental results for 3D self-symmetry detection and characterization, 3D correspondence determination between isometric shapes, and stable 3D part or region detection. We conclude the chapter in Section 2.7 with an outline of directions for future work.

2.3 Related Work and Background

The proposed global shape descriptor is based on the computation of quasi-geodesics between all pairs of points over the discrete triangulated 3D surface mesh that can encode the local geometry at discrete points over the surface mesh as well. The eigenspectrum of the descriptor is exploited to address shape self-symmetry

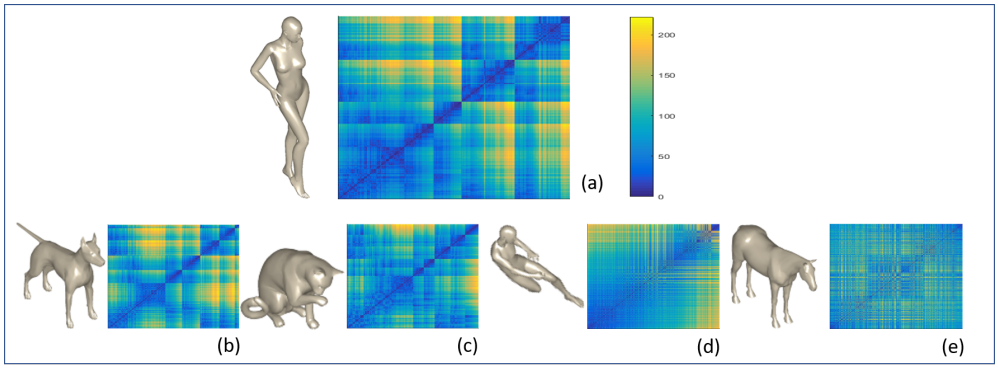

Figure 2.1: Global representation of 3D shapes using quasi-geodesics computed over a discrete triangulated 3D surface mesh. The 3D shape models shown are (a) *Victoria* (b) *Dog* (c) *Cat* (d) *Michael* and (e) *Horse*. The all-point-pairs quasi-geodesic matrix representation of the 3D shapes is observed to be approximately symmetric and the resulting eigenspectrum is observed to preserve self-symmetry over the discrete triangulated 3D mesh-based representation of the 3D shapes.

and correspondence determination between isometric shapes. In this section, we first present a brief survey of relevant local shape representation schemes and spectrum-based shape correspondence models (Heider et al. [2011b]; Van Kaick et al. [2011a]). We also discuss relevant work on coupled quasi-harmonic bases proposed by Kovnatsky et al. [2013], which exploits the commutativity of the isometric shape eigenspectrum to establish correspondence between approximately isometric shapes.

2.3.1 Local shape descriptors

The different classes of local shape descriptors can be categorized based on their approach towards sampling of the underlying local surface geometry. **Ring-based descriptors** are typically based on local sampling of a predefined metric over the discrete 3D surface mesh, however, they differ in their strategies for evaluation of the metric. Some of the prominent descriptors belonging to this class employ *blowing bubbles* (Mortara et al. [2004]; Pottmann et al. [2009a]) centered around a sample surface point, whereas others use the geodesic diameter to sample the surface metric in a local neighborhood (Pottmann et al. [2009a]). These descriptors explicitly control the radius parameter of the bubbles or discs which in turn determines the size of the sample surface region.

Some ring-based descriptors (Gatzke et al. [2005]) use the local surface normal vectors computed at discrete points on the surface mesh to capture the local surface features. *Geodesic fan descriptors* sample a local surface metric based on the values of the local surface curvature or the outward surface normal vector within regions of varying radii defined over the 3D surface mesh (Gatzke et al. [2005]; Ong and Seghouane [2011b]). *Splash descriptors* employ values of the surface normal vector as the primary metric for local surface characterization (Stein and Medioni [1992]) whereas *point descriptors* (Yamany and Farag [1999]; Chua and Jarvis [1997]; Yamany and Farag [2002]) encode the local geometric features on the surface mesh defined by the relative local surface normal at a sample point with respect to a superimposed plane or line segment at the sample points. One of the more prominent examples from this category of shape descriptors is the point

descriptor proposed by Kokkinos et al. [2012] where feature points are represented by local geometric and photometric fields.

Expanding descriptors fit a hypothesis-based model to a surface region in order to characterize it. Important shape descriptors from this category typically employ a parametric model involving features such as geodesic distance (Cipriano et al. [2009]; Mortara et al. [2004]), volume and/or surface area (Connolly [1986]; Pottmann et al. [2009b]). Some variants of this descriptor use a mesh smoothing (Li and Guskov [2005]) or mesh saliency computation (Lee et al. [2005]) procedure that is employed over a specific region on the 3D surface mesh.

Iterative operator-based descriptors capture the geometric changes within a shape by manipulating the entire mesh surface. As a manipulation strategy they employ techniques such as smoothing (Li and Guskov [2005]) or estimation of local diffusion geometry (Bronstein et al. [2010]) over the mesh surface. The well known Laplace-Beltrami operator proposed by Rustamov [2007] is typically employed to compute the diffusion-based shape descriptors within this class.

2.3.2 Global shape representation

In most situations, knowledge of local surface geometry alone is insufficient to characterize the entire shape. Consequently, a global shape representation based upon local surface features is necessary to effectively address the correspondence problem, which is fundamental to many computer vision and computer graphics applications. In recent times, surface descriptors based on the eigenspectrum of the Laplace-Beltrami operator have gained popularity in the context of the

correspondence problem. Some well known examples of surface descriptors from this class are based on the formulation of a diffusion process. The diffusion process is guided by the Laplace-Beltrami operator (Rustamov [2007]) that samples a surface metric, such as the mesh connectivity, along the geodesic curves on the 3D surface mesh. In related work, Bronstein et al. [2010] used diffusion geometry to measure the point-to-point length along a specific path on the surface mesh using a random walk model.

Surface descriptors based on the *heat kernel signature* (HKS) proposed by Sun et al. [2009]; Bronstein and Kokkinos [2010] employ the heat diffusion model in conjunction with the eigenspectrum of the Laplace-Beltrami operator to characterize global shape. In an anisotropic variation, due to Boscaini et al. [2016] use the eigenspectrum of a directional version of the Laplace-Beltrami operator for shape representation. The *wave kernel signature* (WKS) (Aubry et al. [2011]) is another popular category of shape descriptors based on the Laplace-Beltrami eigenspectrum, that employs the principles of quantum mechanics instead of heat diffusion to characterize the shape. Smeets et al. [2012] address the global representation of shape by computing the geodesic distances between sample points on the 3D surface mesh resulting in a shape representation scheme that is shown to achieve robustness against nearly isometric deformations. The level set-based deformable shape model proposed by Lucas et al. [2013], is a variant of the diffusion-based shape descriptor, has been successfully employed in various applications such as surface segmentation, surface registration and object tracking.

2.3.3 Joint diagonalization of the commutative eigenspectrum

Point- or region-specific correspondence between isometric shapes can be addressed by exploiting the commutative property of the shape spectrum representation. In this section we briefly describe the technique by laying emphasis on relevant work on coupled quasi-harmonic bases (Kovnatsky et al. [2013]) that employs the commutative property of the isometric (or near isometric) shape spectrum to address the problem of correspondence determination between isometric shapes.

Commutative eigenspectrum

Formally, the commutative property implies that given two unitary (i.e., Hermitian or orthogonal) operators Φ_X and Φ_Y defined over an isometric pair of shapes X and Y, one can determine a joint diagonalizer Ψ that diagonalizes both $\Psi^T\Phi_X\Psi$ and $\Psi^T\Phi_Y\Psi$ (Cois Cardoso [1995]). The joint diagonalizer Ψ represents the common eigenbases between the isometric shape spectra Φ_X and Φ_Y. Shapes represented as discrete triangulated meshes need not be exactly isometric to each other due to discretization error. Therefore, in the discrete case, the corresponding shape spectra would be *approximately commutative*. In this chapter, the term *approximately commutative* is used in the following sense: The spectra Φ_X and Φ_Y of the triangulated shapes X and Y are approximately commutative if $||\Phi_X\Phi_Y - \Phi_Y\Phi_X||_F \approx 0$ where $||\Lambda||_F$ represents the Frobenius norm of matrix Λ.

A detailed treatment of the common eigenbases for approximately commutative spectral operators can be found in related work proposed by Cois Cardoso [1995]; Yeredor [2002]. Some recent important works by Kovnatsky et al. [2015, 2013]

employ the commutative principle to formulate a least-squares optimization criterion which is then used to extract a common spectral bases to address the problem of correspondence determination between isometric shapes. In the following subsection, we specifically describe the coupled quasi-harmonic bases formulated by Kovnatsky et al. [2013].

Coupled quasi-harmonic bases

The coupled quasi-harmonic bases address the problem of correspondence determination between two approximately isometric 3D shapes X and Y by determining the common bases that exist within their respective eigenspectra. The proposed optimization criterion determines bases $\widehat{\Phi}_X$ and $\widehat{\Phi}_Y$ that jointly diagonalize the Laplacians Δ_X and Δ_Y defined over the approximately isometric 3D shapes X and Y respectively. The common eigenbases $\widehat{\Phi}_X$ and $\widehat{\Phi}_Y$ are extracted via minimization of the optimization criterion in eqn. (2.1).

$$\begin{aligned} \underset{\widehat{\Phi}_X, \widehat{\Phi}_X}{\operatorname{argmin}} \Big\{ & \operatorname{off}(\widehat{\Phi}_X^T W_X \widehat{\Phi}_X) + \operatorname{off}(\widehat{\Phi}_Y^T W_Y \widehat{\Phi}_Y) + \\ & ||F^T \widehat{\Phi}_X - G^T \widehat{\Phi}_Y||_F^2 \Big\} \\ \text{such that } & \widehat{\Phi}_X^T D_X \widehat{\Phi}_X = I \text{ and } \widehat{\Phi}_Y^T D_Y \widehat{\Phi}_Y = I \end{aligned} \tag{2.1}$$

In eqn. (2.1), $\operatorname{off}(A) = \sum_{1 \leq i \neq j \leq n} |a_{ij}^2|$ for an $n \times n$ matrix A with elements a_{ij}. Matrices W and D are components of the discrete cotangent Laplacians Δ_X and Δ_Y of the discrete surface meshes X and Y respectively such that $\Delta_X = W_X^{-1} D_X$

and $\Delta_Y = W_Y^{-1} D_Y$. The cotangent discretization scheme for the mesh-based Laplacian proposed by Meyer et al. [2003] is used to compute the values of Δ_X and Δ_Y. The third term in the optimization criterion (eqn. (2.1)) represents the coarse correspondence between the 3D shapes X and Y provided that prior knowledge of the point-wise mapping between the shapes X and Y is stored in matrices F and G.

In this chapter, we employ the principle of common eigenbases between shape spectrum corresponding to isometric shapes to establish region wise correspondence. However, in contrast to the coupled quasi-harmonic bases (Kovnatsky et al. [2013]) described is eqn. (2.1), the optimization criterion proposed in the chapter does not require any prior knowledge of the correspondence between the shapes under consideration. We further elaborate upon the optimization scheme for correspondence determination in Section 2.5.2.

2.4 Contributions of the work

In this chapter, we propose a global shape representation $D_g(X)$ for a 3D manifold X that incorporates local surface geometry. The proposed representation is based on the computation of the shortest quasi-geodesic distances between all point pairs on the shape manifold. The proposed shape representation is shown to preserve the local surface geometry at each point on the 3D surface mesh. Furthermore, we effectively exploit the eigenspectrum of the proposed shape representation in the following applications:

(1) *Self-symmetry characterization*: We address the problem of self-symmetry characterization by exploiting the eigenspectrum of the proposed global shape descriptor $D_g(X)$.

(2) *Correspondence determination*: We determine the region-wise correspondence between isometric 3D shapes without requiring the user to determine and specify *a priori* the point-wise mapping between the two 3D shapes.

(3) *Isometry deformation characterization*: We exploit the results of the region-wise correspondence to characterize and quantify the extent of isometry deformation between the 3D shapes.

(4) *Stable part or region detection:* We exploit the commutative property of the eigenfunctions of $D_g(X)$ to extract pose-invariant stable parts or surface regions within non-rigid 3D shapes under high degree of isometry transformation.

2.5 Local Geometry Inclusive Shape Operator

In the proposed scheme, a discrete 3D shape manifold X is characterized by an operator $D_g(X)$, that is computed by determining the quasi-geodesics over the discrete manifold X. It is known that along a geodesic over a continuous manifold, only the normal component of the local curvature is dominant when compared to the tangential component. A discrete 3D shape manifold X, in the form of a triangulated 3D surface mesh, can be represented by a C^2 differentiable function $f : \mathbb{R}^3 \rightarrow \mathbb{R}$ as $X = \{f(x_1), f(x_2), ..., f(x_n)\}$ where n denotes the number of vertices $x_i, 1 \leq i \leq n$ of X Azencot et al. [2014]; Martinez Esturo et al.

[2014]. The quasi-geodesic computed for a discrete path $x_i \rightsquigarrow x_j$ minimizes the distance measure $d(f(x_i), f(x_j))$ between the vertices x_i and x_j of X. The proposed shape representation $D_g(X)$ records all such quasi-geodesics, computed between all vertex-pairs or point-pairs over the surface mesh X. Furthermore, the matrix representation of $D_g(X)$ reveals an implicit symmetrical form, as is evident for the example 3D shapes shown in Fig. 2.1.

For discrete meshes, the computation of geodesics is enabled by stable schemes proposed by Martínez et al. [2005]. The local geometry along a quasi-geodesic over a discrete mesh is preserved as follows: Fig. 2.2 depicts two scenarios where a probable quasi-geodesic (marked in red) crosses a neighborhood of triangular meshes. In either case, one can measure the discrete geodesic curvature at a point P as follows:

$$\kappa_g(P) = \frac{2\pi}{\theta}(\frac{\theta}{2} - \theta_r) \tag{2.2}$$

In eqn. (2.2), θ denotes the sum of all angles incident at point P where the geodesic crosses the surface mesh. In both cases, depicted in Figs. 2.2(a) and 2.2(b), the quasi-geodesics generate angular distributions θ_l and θ_r such that $\theta_l = \sum_i \beta_i$ and $\theta_r = \sum_i \alpha_i$. Since the normal curvature is dominant along the quasi-geodesics, we can compute an optimum balance between θ_l and θ_r that minimizes the discrete geodesic curvature κ_g, which is the tangential curvature component along the quasi-geodesic. This optimal balance between angular distributions along the quasi-geodesic approximately encodes the local angular distribution and hence, the local geometry at surface point P as depicted in Figs. 2.2(a) and 2.2(b).

The spectral decomposition of the symmetric shape operator $D_g(X)$ results in the eigenspectrum Φ_X for shape X as follows:

$$D_g(X)\Phi_X = \Delta_X \Phi_X \tag{2.3}$$

where $\Delta_X = \text{diag}(\gamma_1, \gamma_2, ..., \gamma_n)$ denotes the diagonal matrix of eigenvalues $\gamma_i, 1 \leq i \leq n$ and $\Phi_X = \{\Phi_X^1, \Phi_X^2, ..., \Phi_X^n\}$ denotes the eigenvectors $\Phi_X^i, 1 \leq i \leq n$ of shape X with n surface vertices.

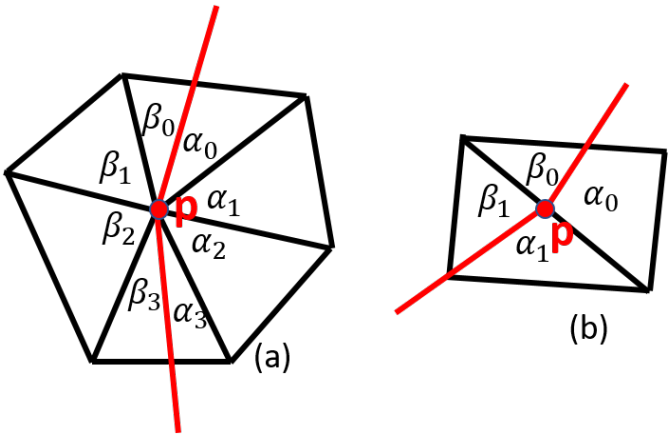

Figure 2.2: The right and left angular distributions θ_l and θ_r generated by a geodesic at point P on the surface mesh. The angular measures θ_l and θ_r encode the local geometry on a discrete surface mesh.

2.5.1 Self-symmetry characterization

We characterize self-symmetric regions over shape X as follows. Two regions $X_1, X_2 \subset X$ are possible candidates for being symmetric regions if for some upper

bound ε:

$$\left| \sum_{k=1}^{k_0} \Phi_X^k(p) - \sum_{k=1}^{k_0} \Phi_X^k(q) \right|_2 \leq \varepsilon \quad \forall p \in X_1,\ \forall q \in X_2 \tag{2.4}$$

where $|\cdot|_2$ denotes the $\mathcal{L}^2$ norm. Using spectral analysis one can find a tight bound on ε such that $\varepsilon \leq \sum_{p,q \in X_1,\, r,s \in X_2} |d(p,q) - d(r,s)|_2$ for a C^2 distance metric d (Dunford and Schwartz [1963]). Parameter ε depends upon the variance of geodesic error computed over the entire shape manifold X. Therefore, for shape manifold X, ε is a measure of the degree of isometry deformation of X vis-a-vis the baseline shape. We report the bounds on ε computed for different meshes in the Experimental Results section (Section 2.6). For characterizing self-symmetry we restrict ourselves to the lower-order eigenvectors characterized by $k_0 \leq 20$. Furthermore, the above characterization can be also used to jointly analyze the correspondence between two candidate isometric shapes X and Y (Section 2.5.2).

2.5.2 Correspondence determination between isometric shapes

Determining the compatibility between the eigenbases of various shapes plays a critical role in applications dealing with analysis of multiple 3D shapes; in particular, determining the correspondence between 3D shapes. In related work, Ovsjanikov et al. [2012] represent the correspondence between two shapes by a parametric map between their functional spaces. However, functional map-based methods typically rely on user-specified prior knowledge of the mapping between the shapes for optimization of the correspondence criterion (Nguyen et al. [2011];

Ovsjanikov et al. [2012]). In contrast, the proposed approach does not assume any user-specified prior mapping between the shapes under consideration.

For correspondence determination between two isometric shapes X and Y we exploit the fact that the eigen decomposition of symmetric shape operators $D_g(X)$ and $D_g(Y)$ leads to approximately commutative eigenspectra Φ_X and Φ_Y. The characterization "approximately commutative" is on account of the discretization or triangulation of the surface meshes describing the shapes and follows the formal definition given in Section 2.3.3. We couple Φ_X and Φ_Y by the commutative terms $\Phi_X^T \Delta_Y \Phi_Y$ and $\Phi_Y^T \Delta_X \Phi_X$ to solve the following optimization problem:

$$\bar{\Phi}_X, \bar{\Phi}_Y = \underset{\phi_x, \phi_y}{\operatorname{argmin}} \left\{ |\phi_x^T \Delta_Y \phi_y|_F + |\phi_y^T \Delta_X \phi_x|_F \right\} \tag{2.5}$$

where $\phi_x \subset \Phi_X$, $\phi_y \subset \Phi_Y$ and $|\cdot|_F$ denotes the Frobenius norm. It should be emphasized that eqn. (2.5) does not require that *a priori* correspondence maps be provided. The optimized maps $\bar{\Phi}_X$ and $\bar{\Phi}_Y$ over shapes X and Y encode the correspondence between them. From the optimized maps $\bar{\Phi}_X$ and $\bar{\Phi}_Y$, the relative correspondence error between shapes X and Y is given by $C_{X,Y} = \sum_{k=1}^{k_0} |\bar{\Phi}_X^k - \bar{\Phi}_Y^k|_2$. To compute $C_{X,Y}$ we consider the lower-order eigenvectors by setting $k_0 \leq 20$.

2.5.3 Stable 3D surface region or part detection

Relaxing the criterion for correspondence determination by not requiring a user-specified prior mapping between the shapes could result in poor correspondence

between shapes that differ significantly from each other via isometry transformation. However, the optimization criterion for correspondence determination can also be used to identify common stable surface regions or parts within the shapes. These stable surface regions or parts are deemed to be the ones that have undergone the least amount of isometry deformation as a result of pose variation. We present the following criterion to identify the stable regions $S_{X,Y}$ between shapes X and Y as follows:

$$S_{X,Y} = \bigcup_{p} |\bar{\Phi}_X(p) - \bar{\Phi}_Y(p)|_2 \leq \varepsilon \tag{2.6}$$

where region p represents a corresponding region in both shapes X and Y identified by the correspondence optimization criterion in eqn. (2.5). The parameter ε is computed as mentioned in Section 2.5.1. The stable part detection is quantified using the following criterion: $\bar{S}_{X,Y} = \sum_{p \in S_{X,Y}} \quad |\bar{\Phi}_X(p) - \bar{\Phi}_Y(p)|_2$.

2.6 Experimental Results

For our experiments we have chosen the TOSCA dataset consisting of ten non-rigid shape categories, i.e., *Cat*, *Dog*, *Wolf*, two *Human Males*, *Victoria*, *Gorilla*, *Horse*, *Centaur* and *Seahorse* (Ovsjanikov et al. [2009]). Within each shape category, the individual shapes represent different transformations such as isometry, isometry coupled with topology change, different mesh triangulations of the same shape etc. In this work, we consider shapes that are isometric to one another, i.e., shapes that differ via an isometry transformation. Examples of some shapes that differ

from one another via isometry transformations are shown in Fig. 2.3. Experimental results are presented for six different shape categories for each of the applications formally described in Sections 2.5.1, 2.5.2 and 2.5.3 using visual representations of the results followed by the corresponding numerical evaluations. We have experimented with coarse meshes that are reduced by more than 87% of their original size or resolution. The results of the proposed shape representation are compared with those from relevant state-of-the-art shape representation schemes. The comparable performance achieved by the proposed local geometry-inclusive global shape representation scheme without requiring any prior knowledge of point-to-point or region-wise correspondences validates the central hypothesis underlying the proposed scheme, namely that the implicit isometry within candidate shapes can be exploited for correspondence determination without requiring that the knowledge of coarse correspondence be provided a priori.

2.6.1 Results of 3D self symmetry detection

Fig. 2.4 depicts the self-symmetry maps obtained for the various shapes using eqn. (2.4). The maps in Fig. 2.4 correspond to the second eigenvector Φ_X^2 obtained from the spectral decomposition of the global operator $D_g(X)$ for each shape using eqn. (2.3). Table 2.1 presents the self-symmetry characterization measure, denoted by the upper bound ε in eqn. (2.4), for each shape category. This characterization measure represents the average degree of isometry transformation within a shape category vis-a-vis the baseline shape. Note that the shape category *Michael* represents one of the two *Human Male* shape categories in the TOSCA dataset.

Table 2.1: Self-symmetry characterization measure for different shape categories in the TOSCA dataset. The average degree of isometry transformation within the category *Horse* is observed to be at least 30% higher than the other categories.

Category	ε	Category	ε
Victoria	0.528	*Dog*	0.462
Cat	0.282	*Michael*	0.566
Horse	0.815	*Centaur*	0.203

2.6.2 Results of 3D correspondence between isometric shapes

Since the lower-order eigenvectors represent global shape geometry more accurately, we consider the first 20 eigenvectors to compute the global region-based correspondence between the isometric shapes. Fig. 2.5 shows the results of correspondence determination between the isometric *Human Male* shapes obtained via the optimization criterion described in eqn. (2.5). The correspondence maps between the shapes are shown to be consistent across the different order eigenvectors.

Table 2.2: Average relative error $C_{X,Y}$ in 3D correspondence determination between isometric shapes.

Category	Average $C_{X,Y}$	Category	Average $C_{X,Y}$
Victoria	0.069	*Dog*	0.0624
Cat	0.06	*Michael*	0.057
Horse	0.0559	*Centaur*	0.052

The relative correspondence error for these maps can be characterized by the

measure $C_{X,Y}$ defined in Section 2.5.2. Table 2.2 lists this measure for isometric shapes from different TOSCA shape categories. Lower $C_{X,Y}$ values denote a higher degree of correspondence accuracy achieved via the optimization described in eqn. (2.5). We emphasize here, that the correspondence accuracy is achieved without requiring any user-specified prior mapping between the shapes.

2.6.3 Results of 3D stable region or part detection

Shapes from different categories display varying degrees of isometry transformations between them. As a result, the accuracy of global correspondence deteriorates for shapes that exhibit a very high degree of isometry deformation. This is expected since the proposed scheme does not assume any prior mapping information that could potentially improve the correspondence. However, using the criterion outlined in eqn. (2.6) we can identify the stable corresponding surface regions or parts within the shapes that are least transformed by isometry. The detected stable regions or parts for the *Centaur* shape category are depicted in Fig. 2.6. For various poses of the *Centaur* shape model, the more dynamic regions such as the tail and the lower legs exhibit low correspondence accuracy and hence are rejected by the criterion described in eqn. (2.6). However, regions that are least affected by the isometry deformation are detected as stable regions. These stable regions exhibit high correspondence accuracy and are depicted in Fig. 2.6. We quantify the correspondence accuracy for the detected stable regions using the measure $\bar{S}_{X,Y}$ described in Section 2.5.3. However, in our experiments, we observed a high positive correlation between the measures $C_{X,Y}$ and $\bar{S}_{X,Y}$. Hence we contend that

the results in Table 2.2 hold for measure $\bar{S}_{X,Y}$ as well.

Table 2.3 compares the performance of the proposed representation scheme with the performance of other state-of-the-art representation schemes (Kim et al. [2011]; Sahillioglu and Yemez [2011]). The methods proposed by Kim et al. [2011]; Sahillioglu and Yemez [2011] were further combined with the functional map technique by Ovsjanikov et al. [2012] in order to improve their correspondence accuracy via functional map-based local refinement. The results of performance comparison for these combined approaches with the proposed representation are also presented in Table 2.3. The numerical values presented in Table 2.3 denote the highest percentage correspondence accuracy achieved by the various representation schemes along with the corresponding average geodesic error. The performance of the proposed representation scheme is observed to compare very well with the performance of the other state-of-the-art representation schemes. These results underscore the central hypothesis underlying the proposed shape representation, namely that competitive performance in self-symmetry detection and characterization, and correspondence map determination between isometric 3D shapes can be achieved by the proposed representation scheme without requiring prior knowledge of coarse correspondence mapping between the shapes unlike other state-of-the-art correspondence determination techniques Kim et al. [2011]; Sahillioglu and Yemez [2011].

Table 2.3: Comparison between the proposed scheme and other state-of-the-art schemes proposed by Kim et al. [2011], Sahillioglu and Yemez [2011] and their combinations with functional map by Ovsjanikov et al. [2012].

Methods	Geodesic Error	% Correspondence
Kim et al. [2011]	0.11	~ 95
Ovsjanikov et al. [2012] and Kim et al. [2011]	0.06	~ 95
Sahillioglu and Yemez [2011]	0.25	~ 90
Ovsjanikov et al. [2012] and Sahillioglu and Yemez [2011]	0.2	~ 90
Proposed Scheme	0.15	~ 94

2.7 Conclusions and Future Work

In this chapter we proposed a global shape representation scheme using quasi-geodesics computed over the entire discrete shape manifold. The eigenspectral decomposition of this representation is used effectively to identify self-symmetric regions on the discrete shape manifold. By exploiting the commutative property of the eigenbases of the proposed representation, we successfully demonstrated its use in correspondence determination between isometric shapes. We also proposed characterization metrics for self-symmetry identification and correspondence determination. Furthermore, stable surface regions within 3D shapes were identified for shape pairs that differed from each other by a high degree of isometry deformation. The results of correspondence determination obtained via the proposed

representation scheme were compared with those from relevant state-of-the-art representation schemes.

A key contribution of this work is the fact that no prior knowledge, in the form of user-specified mappings, was used for correspondence determination and self-symmetry detection. As an extension of the current scheme, we intend to explore and combine functional maps (Ovsjanikov et al. [2012]) with the proposed representation that may prove critical in exploring the group structure within isometric shapes. Furthermore, we intend to use this combined scheme to address correspondence determination between near-isometric shapes (Kovnatsky et al. [2013]).

Figure 2.3: Examples of isometry transformation for the shape categories *Human Male* and *Centaur* in the TOSCA dataset.

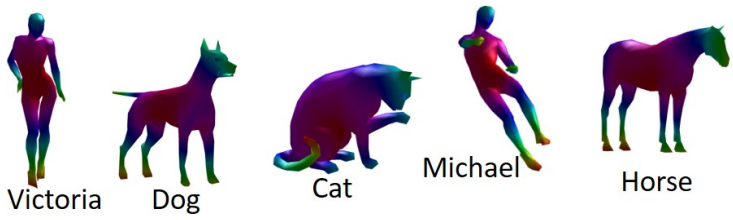

Figure 2.4: Self-symmetry detection for five different TOSCA shape categories using the spectrum of the global representation $D_g(X)$ for the shape X. Each map corresponds to the second eigenvector Φ_X^2 of the shape operator spectrum.

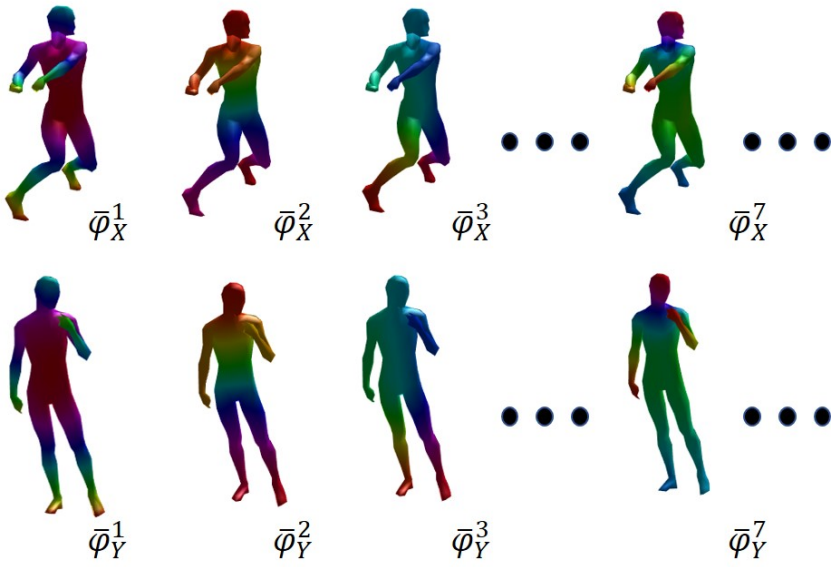

Figure 2.5: Pairwise consistency between corresponding eigenmaps of the *Human Male* shapes. For correspondence estimation, the optimization criterion described in eqn. (2.5) is used. Lower-order eigenvectors are considered for correspondence estimation since they effectively capture the global shape geometry.

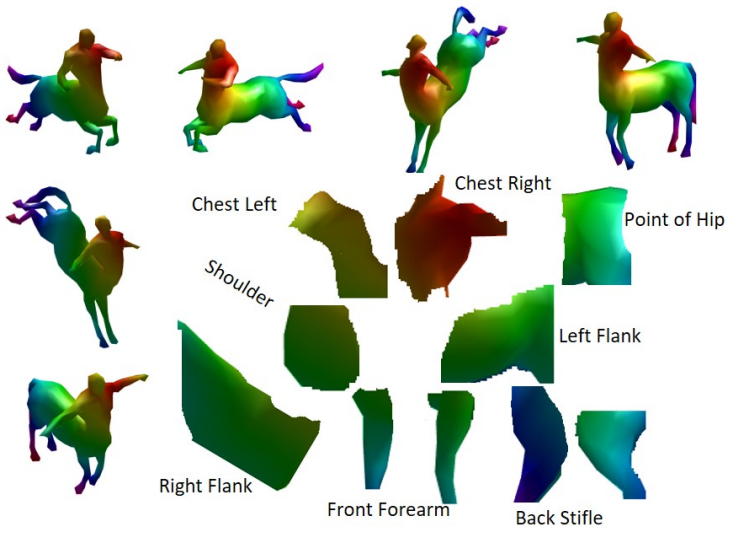

Figure 2.6: Stable region detection using the criterion outlined in eqn. (2.6). Stable surface regions are detected between isometric shapes where the correspondence accuracy is observed to deteriorate due to a high degree of isometry transformation between the shapes. Unstable regions are ones that exhibit a higher degree of isometry transformation between them, for example, parts of the lower legs, the tail, etc.

Chapter 3

Principal Curvature Guided Surface Geometry Aware Global Shape Representation

Somenath Das[1], Dr. Suchendra M. Bhandarkar

[1]First Author. Accepted by Proceedings of Computer Vision and Pattern Recognition 2018 (CVPR) workshops, Reprinted here with permission of publisher, To Appear

3.1 Abstract

In this chapter, a surface principal curvature preserving local geometry aware global shape representation for 3D shapes is proposed. The shape representation computes the shortest quasi-geodesic path between all possible pairs of points on the shape manifold that enforces minimal variation of geodesic curvature along the path. The normal component of the principal curvature along the quasi-geodesic paths is dominant and shown to preserve the local shape geometry. The eigen-spectrum of the proposed representation is exploited to characterize self-symmetry. The commutative property between shape spectra is exploited to compute region-based correspondence between isometric 3D shapes without requiring an initial correspondence map to be specified a priori. The results of the region-based correspondence are extended to characterize the compatibility of the commutative eigen-spectrum in order to address the problem of shape deformation transfer. eigenspectrum based characterization metrics are proposed to quantify the performance of the proposed 3D shape descriptor for self-symmetry detection and correspondence determination. The proposed shape descriptor spectrum-based optimization criterion is observed to yield competitive performance compared to relevant state-of-the-art correspondence determination techniques.

3.2 Introduction

In Computer Graphics, the study of surface geometry-aware global 3D shape descriptors is critical to enable various 3D shape analysis applications. A desirable

quality of a 3D shape descriptor is its ability to discriminate between local regions of a 3D shape, an essential requirement for applications that entail determination of point-wise correspondence between 3D shapes. Ideally, a 3D shape descriptor should demonstrate robustness to local topological noise while effectively capturing the underlying stable shape features that are essential for correspondence determination between 3D shapes. Based on the modality of the underlying shape data (i.e., geometric, topological, etc.) and objective(s) of the application, 3D shape analysis applications can be broadly categorized as purely geometric, semantic or knowledge-driven (Van Kaick et al. [2011a]). Several 3D shape analysis applications drawn from the aforementioned categories typically entail solving a fundamental problem, i.e., one of determining accurate correspondence between the 3D shapes under consideration. Examples of these applications include rigid and non-rigid shape registration (Chang and Zwicker [2008]; Gelfand et al. [2005]), shape morphing (Kraevoy and Sheffer [2004]), self-symmetry detection (Gal and Cohen-Or [2006]), shape deformation transfer (Sumner and Popović [2004]), 3D surface reconstruction (Pekelny and Gotsman [2008]), and shape-based object recognition and retrieval (Jain and Zhang [2007]) among others. The success of these applications is critically dependent on the shape descriptors used for 3D shape correspondence determination. Several of these applications, however, are also dependent upon prior specification of an initial shape correspondence.

In this chapter, we propose a global 3D shape descriptor based on estimation of the approximate geodesic distance between all point pairs on a triangulated mesh-based 3D shape manifold. The 3D shape descriptor represents all the ver-

tices on the 3D shape manifold by their differential coordinates. This allows the geodesics over a 3D shape manifold to be defined as surface curves along which the normal component of the principal curvature is dominant. This property of the geodesics is used to encode the local surface geometry along the curve. The proposed 3D shape descriptor is shown to effectively address the computation of 3D self-symmetry within a shape. The eigenspectrum of the 3D shape descriptor is exploited to address a very important problem, i.e., correspondence determination between isometric 3D shapes (i.e., 3D shapes that are related via an isometric transformation) *without* requiring any prior knowledge about the underlying shapes. Furthermore, the compatibility of the shape descriptor eigenspectra is formally characterized to generate continuous deformations of a given shape to enable applications such as 3D shape deformation transfer.

On a triangulated 3D surface mesh, the discrete approximation to a geodesic is characterized by an optimal balance of angular distributions over the surface on the either side of the geodesic. These angular distributions are computed in a local neighborhood of each mesh point on the geodesic as depicted in Fig. 3.2 (b) and (c). The balance of the local angular distribution is observed to encode the local geometry of the triangulated mesh along the discrete geodesic. The approximation to a geodesic computed over a discrete 3D triangulated mesh is referred to as a *quasi-geodesic* (Martínez et al. [2005]). The proposed shape descriptor represents the global 3D shape by computing the quasi-geodesic path between all point pairs on the discrete 3D triangulated surface mesh, along which the normal component of the principal curvature is dominant.

We use the eigenspectrum of the global quasi-geodesic-based shape descriptor that encodes that local shape geometry to characterize self-symmetry within a shape and to establish correspondence between isometric deformations of a shape without resorting to any a priori knowledge of the correspondence maps. The all-point-pairs geodesic matrix representation of 3D shapes displays a symmetrical pattern as shown in Fig. 3.1. We employ the eigenspectrum of the symmetrical pattern to detect self-symmetry within a shape. To determine the correspondence between isometric shapes, we exploit the commutative property of the eigenvectors corresponding to the shape descriptor eigenspectrum (Cois Cardoso [1995]). The commutative property is shown to demonstrate the approximate orthogonality between different isometric deformations of a discrete triangulated mesh-based 3D shape. Approximate orthogonality refers to the fact that for two distinct eigenvectors ϕ_i and ψ_j chosen from separate shape descriptor eigenspectra, $|\langle \phi_i, \psi_j \rangle| < \epsilon$ where $\langle \cdot, \cdot \rangle$ denotes the scalar inner product of the vector arguments and $\epsilon \approx 0$.

It should be noted that the eigenspectrum of the proposed descriptor is distinct from the well known Laplace-Beltrami eigenspectrum that has been used extensively in several 3D shape analysis and shape synthesis applications. In our case, we exploit the commutative property of the shape descriptor eigenspectrum to establish the correspondence between isometric 3D shapes. It should also be emphasized that, unlike many related approaches by Kovnatsky et al. [2013]; Ovsjanikov et al. [2012], the optimization criterion proposed to establish correspondence between isometric 3D shapes does not exploit nor require user-specified initial correspondence maps between the 3D shapes. Furthermore, we extend the

correspondence maps detected between isometric shapes to the other isometric deformations of the baseline shapes, with an objective to characterize the compatibility of the correspondence maps to generate smooth deformations of the baseline shapes to enable 3D shape deformation transfer. To the best of our knowledge, the problem of correspondence determination in the absence of prior knowledge of any point-wise mapping between the shapes had not been studied extensively in the research literature.

The remainder of the chapter is organized as follows. In Section 3.3, we present a brief survey of the most relevant works on 3D shape description with an emphasis on the commutative property of isometric shape eigenspectra employed in the proposed correspondence determination scheme. Section 3.4 describes the specific contributions of our work. The mathematical formulation of the proposed shape descriptor and the associated applications are detailed in Section 3.5. In Section 3.6, we present experimental results for 3D self-symmetry detection and characterization, 3D correspondence determination between isometric shapes, and the analysis of compatibility of the commutative eigenspectra used to generate a continuous deformation of a given shape. We conclude the chapter in Section 3.7 with an outline for future work.

3.3 Background and Related Work

The proposed global shape descriptor is based on the computation of quasi-geodesics between all pairs of points over the discrete triangulated 3D surface mesh where

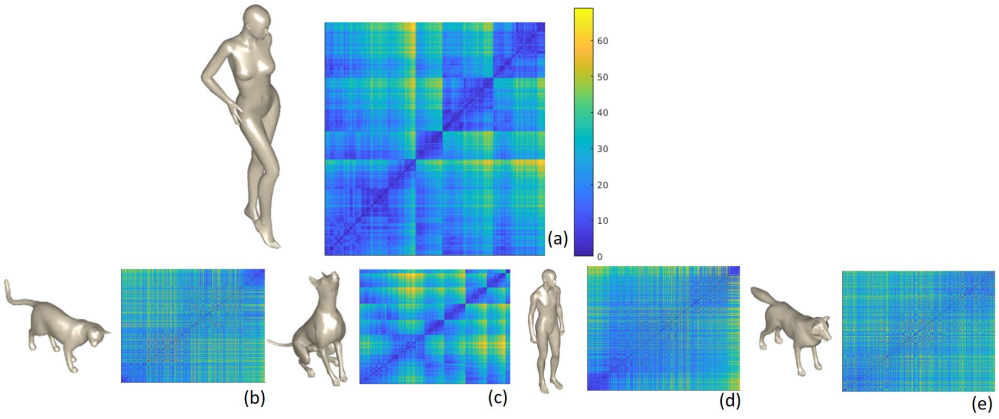

Figure 3.1: Global representation of 3D shapes using quasi-geodesics computed over a discrete triangulated 3D surface mesh. The 3D shape models shown are (a) *Victoria* (b) *Cat* (c) *Dog* (d) *David* and (e) *Wolf*. The all-point-pairs quasi-geodesic matrix representation of the 3D shapes is observed to be approximately symmetric and the resulting eigenspectrum is observed to preserve self-symmetry over the discrete triangulated 3D mesh-based representation of the 3D shapes.

each mesh vertex is represented by its neighborhood-based surface differential. The proposed shape descriptor effectively encodes the local geometry at discrete points over the surface mesh. The eigenspectrum of the descriptor is exploited to address shape self-symmetry, correspondence determination between isometric shapes and the formulation of a metric to characterize generation of smooth deformations of a baseline shape. In this section, we first present a brief survey of some relevant local and global shape descriptors, spectrum-based shape correspondence models and deformation transfer models (Van Kaick et al. [2011a]; Heider et al. [2011b]). We also discuss the principle underlying the commutative property between isometric shape eigenspectra and related work by Kovnatsky et al. [2013] that exploits this

principle to determine the correspondence between quasi-isometric shapes.

3.3.1 Local shape descriptors

The different classes of local shape descriptors can be categorized based on their approach towards the encoding of the underlying local surface geometry. **Ring-based descriptors** typically sample a local surface metric using a parametrically controlled local neighborhood based on *blowing bubbles* (Mortara et al. [2004]) or geodesic diameter (Pottmann et al. [2009a]). Some ring-based descriptors use the local surface normal vectors as surface features computed at discrete points on the surface mesh (Gatzke et al. [2005]; Stein and Medioni [1992]; Ong and Seghouane [2011a]), relative to a superimposed frame of reference over the mesh (Yamany and Farag [1999]; Chua and Jarvis [1997]; Yamany and Farag [2002]) or in combination with local surface curvature (Gatzke et al. [2005]; Ong and Seghouane [2011b]). **Expanding descriptors** fit a hypothesis-based parametric model based on features such as geodesic distance (Mortara et al. [2004]; Cipriano et al. [2009]), volume or surface area (Connolly [1986]; Pottmann et al. [2009b]) to characterize a surface region. Some variants of this descriptor use mesh smoothing (Li and Guskov [2005]) or mesh saliency (Lee et al. [2005]) applied over the surface mesh. **Iterative operator-based descriptors** capture the geometric changes within a shape by manipulating the entire mesh surface by employing strategies such as smoothing (Li and Guskov [2005]), estimation of local diffusion geometry (Bronstein et al. [2010]) over the mesh surface, or diffusion based variation (Rustamov [2007]) within the surface mesh.

3.3.2 Global shape representation

A global shape representation based upon local surface features is important to effectively characterize the global shape and determine the correspondence between shapes, a fundamental problem in many computer vision and computer graphics applications. Surface descriptors based on the eigenspectrum of the Laplace-Beltrami operator have gained recent popularity in the context of the correspondence problem. Some well known surface descriptors from this class employ a Laplace-Beltrami operator-guided diffusion process that samples a surface metric based on mesh connectivity along the geodesic curves on the 3D surface mesh (Rustamov [2007]) and diffusion geometry (Bronstein et al. [2010]) to measure the point-to-point length along a specific path on the surface mesh.

Surface descriptors based on the *heat kernel signature* (HKS) by Sun et al. [2009]; Bronstein and Kokkinos [2010]; Boscaini et al. [2016] employ the heat diffusion model in conjunction with the eigenspectrum of the Laplace-Beltrami operator to characterize the global shape. The *wave kernel signature* (WKS) (Aubry et al. [2011]) employs the principles of quantum mechanics, instead of heat diffusion, in conjunction with the Laplace-Beltrami eigenspectrum to characterize the 3D shape. Smeets et al. [2012] present a geodesic distance-based global shape representation that demonstrates robustness to nearly isometric deformations.

3.3.3 Deformation transfer models

Deformation transfer between shapes (Lévy [2006]; Sumner et al. [2005]) is an important application in computer graphics that employs global shape descriptors.

The principles of deformation transfer have been employed in many applications such as machine learning-based human motion modeling (Pons-Moll et al. [2015]) and sensor-based surface reconstruction (Zollhöfer et al. [2014]) to name a few. However, to the best of our knowledge, modeling large-scale deformations using spectral techniques without employing any prior knowledge of correspondence between the shapes has not been explored in detail. In this chapter, we propose a metric for characterization of commutative eigenspectra that can quantify the compatibility of the spectra in order to generate smooth deformations of a baseline shape to enable shape deformation transfer.

3.3.4 Commutative eigenspectrum for correspondence between shapes

Point- or region-based correspondence determination between isometric shapes can be addressed by exploiting the commutative property of the shape descriptor eigenspectrum. In this section we briefly describe the principle underlying the commutative eigenspectra between isometric shapes (Cois Cardoso [1995]).

Commutative eigenspectrum

Formally, the commutative property implies that given two unitary (i.e., orthogonal) operators Φ_X and Φ_Y defined over an isometric pair of shapes X and Y, one can determine a joint diagonalizer Ψ that diagonalizes both $\Psi^T \Phi_X \Psi$ and $\Psi^T \Phi_Y \Psi$ (Cois Cardoso [1995]). The joint diagonalizer Ψ represents the common eigenbases between the isometric shape eigenspectra Φ_X and Φ_Y. Shapes represented as discrete triangulated meshes need not be exactly isometric to each other due

to discretization error. Therefore, in the discrete case, the corresponding shape eigenspectra would be *approximately* commutative. In this chapter, the term *"approximately commutative"* is used in the following sense: The eigenspectra Φ_X and Φ_Y of the triangulated shapes X and Y are approximately commutative if $||\Phi_X\Phi_Y - \Phi_Y\Phi_X||_F \approx 0$ where $||\Lambda||_F$ represents the Frobenius norm of matrix Λ.

A detailed treatment of the common eigenbases for approximately commutative spectral operators can be found in frameworks proposed by Cois Cardoso [1995]; Yeredor [2002]. Some recent works (Kovnatsky et al. [2013, 2015]) employ the commutative principle to formulate a least-squares joint optimization criterion, to extract a common spectral bases that can address correspondence determination between isometric shapes. These applications, however, use prior knowledge of the correspondence to regularize the joint optimization criterion and employ the cotangent discretization scheme for the mesh-based Laplacian (Meyer et al. [2003]) to represent the shape operators.

In this chapter, we employ the principle of common eigenbases between commutative eigenspectra corresponding to isometric shapes to determine region-wise correspondence. However, in contrast to existing works by Kovnatsky et al. [2013], the proposed method employs a novel optimization criterion that does not use any prior knowledge of the correspondence between the shapes under consideration. We elaborate upon the optimization scheme for correspondence determination in Section 3.5.2.

3.4 Contributions in the Chapter

(1) *Self-symmetry characterization*: We address the problem of self-symmetry detection and characterization by exploiting the eigenspectrum of the proposed global shape descriptor.

(2) *Correspondence determination*: We determine region-wise correspondence between isometric 3D shapes without requiring the user to specify *a priori* an initial point-wise mapping between the two 3D shapes.

(3) *Isometry deformation characterization*: We exploit the results of the region-wise correspondence to formally characterize the extent of isometry deformation between the 3D shapes.

(4) *Compatibility characterization for smooth deformation generation:* We extend the commutative property of the eigenfunctions between baseline shapes to characterize the compatibility of the commutative eigenspectrum in order to address generation of smooth deformations of the baseline shapes.

3.5 Proposed Shape Operator and Applications

The proposed shape representation for a discrete 3D shape manifold X is denoted by the operator $D_g(X)$, that is computed by determining the quasi-geodesics between all vertex pairs on the discrete manifold X. For the shape representation, we first transform each vertex by its local neighborhood based surface differential so that the i^{th} vertex of shape manifold X is represented by $\delta x_i = x_i - \frac{1}{N}\sum_{y_j \in N(x_i)} y_j$ i.e. the differential coordinate where $N(x_i)$ is the neighborhood of size N for vertex

x_i and each $y_j \in N(x_i)$ is a neighboring vertex of x_i. Subsequently, a C^2 function $f : \mathbb{R}^3 \rightarrow \mathbb{R}$ (Azencot et al. [2014]; Martinez Esturo et al. [2014]) is associated with each vertex $x_i, (1 \leq i \leq n)$ of shape X comprising of n vertices. Consequently, a discrete, triangulated, 3D shape manifold X is represented by the vertices such that $X = \{f(\delta x_1), f(\delta x_2), ..., f(\delta x_n)\}$ where δx_i denotes the surface differential coordinates for the i^{th} vertex of X. The differential transformation ensures that each vertex location also defines the normal to the surface at the vertex as shown in Fig. 3.2 (a). Along a geodesic over a continuous manifold, only the normal component of the principle curvature is dominant compared to it's tangential component. The quasi-geodesic computed for a discrete path $x_i \rightsquigarrow x_j$ minimizes the geodesic distance measure $d(f(\delta x_i), f(\delta x_j))$ between vertices x_i and x_j of X. It should be emphasized that since each vertex x_i is represented by the surface differential coordinates the distance $d(f(\delta x_i), f(\delta x_j))$ represents a path $x_i \rightsquigarrow x_j$ that goes through a geometrically "flat" region over the surface with minimal variation in local geometry between neighboring points on the path. The proposed shape representation $D_g(X)$ records all such quasi-geodesic distances, computed between all vertex-pairs over the surface mesh X. The matrix representation of $D_g(X)$ reveals an implicit symmetrical form, as is evident for the example 3D shapes shown in Fig. 3.1.

For discrete meshes, the computation of geodesics is possible using the stable schemes proposed by Martínez et al. [2005]. The local geometry along a quasi-geodesic over a discrete mesh is preserved as follows. Fig. 3.2 (b) and (c) depicts two scenarios where a probable quasi-geodesic (marked in red) crosses a point P

within a neighborhood of triangular mesh facets. In either case, one can measure the discrete geodesic curvature at a point P as follows:

$$\kappa_g(P) = \frac{2\pi}{\theta}(\frac{\theta}{2} - \theta_r) \tag{3.1}$$

In eqn. (3.1), θ denotes the sum of all angles formed by the neighborhood of point P. In both the cases, as depicted in Fig. 3.2 (b) and (c), the quasi-geodesics generate angular distributions θ_l and θ_r such that $\theta_l = \sum_i \beta_i$ and $\theta_r = \sum_i \alpha_i$. Since the normal curvature is dominant along the quasi-geodesics, we can compute an optimum balance between θ_l and θ_r that minimizes the discrete geodesic curvature κ_g, which is the tangential component of the curvature along the quasi-geodesic. This optimal balance between angular distributions along a quasi-geodesic encodes the local angular distribution and hence, the local geometry at surface point P.

To test the robustness of the proposed correspondence scheme we experimented with coarse triangulated meshes. For a coarse mesh the variance between neighborhood surface normals increases significantly. Such a variation is visually represented in Fig. 3.3 where variation in surface normals are presented for two coarse meshes where vertices are reduced by 75.02% and 87.05% respectively from the original mesh. Table 3.1 presents the degree of coarseness in terms of normal variances computed for the entire mesh across different shape category. Therefore, to ensure the accurate computation of surface normals at each point of a coarse mesh we considered an additional error correcting scheme explained with an example in Fig. 3.2 (d). Fig. 3.2 (d) depicts a vertex p on the shape manifold with a neighborhood consisting of three vertices q, r and s. As a result, vertex p is shared

Table 3.1: Surface normal variances due to reduction in number of vertices for different shape category.

Shape Category	Variance in normals with		
	Original Mesh	75% reduction	87 % reduction
David	0.4399	0.8355	1.7191
Dog	0.5201	1.0624	1.7974
Cat	0.506	0.9432	1.827
Centaur	1.3003	2.0632	3.8868

between three planes defined by disks D_1, D_2 and D_3 with their corresponding normals $\bar{N}_1$, $\bar{N}_2$ and $\bar{N}_3$, respectively. Normals $\bar{N}_1$, $\bar{N}_2$ and $\bar{N}_3$ can be computed from the vertices p, q, r and s. The accuracy of the computed normal direction at a surface point may be severely affected due to the choice of a coarse triangulated mesh. Therefore, the error correcting scheme ensures that the resulting normal $\bar{N}_R$ is constrained to lie within the solid angle region shown in red in Fig. 3.2 (d) that is bounded by normals $\bar{N}_1$, $\bar{N}_2$ and $\bar{N}_3$.

The spectral decomposition of the symmetric shape representation $D_g(X)$ results in the eigenspectrum Φ_X for shape X such that,

$$D_g(X)\Phi_X = \Delta_X \Phi_X \tag{3.2}$$

where $\Delta_X = \text{diag}(\gamma_1, \gamma_2, ..., \gamma_n)$ denotes the diagonal matrix of eigenvalues $\gamma_i, 1 \leq i \leq n$ and $\Phi_X = \{\Phi_X^1, \Phi_X^2, ..., \Phi_X^n\}$ denotes the eigenvectors $\Phi_X^i, 1 \leq i \leq n$ of shape X with n surface vertices ordered by the corresponding eigenvalues.

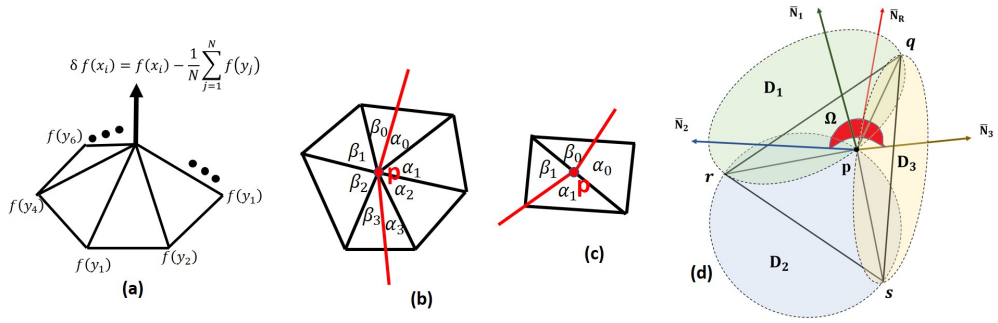

Figure 3.2: The proposed shape descriptor represents each vertex of the mesh by the discrete differential coordinates. (a) The resulting coordinate axis aligns with the normal on the surface at the vertex. Vertices y_j's belong to the neighborhood ring $N(x_i)$ of vertex x_i. (b) and (c) depicts two possible crossings of a geodesic at a point P on the surface. The balance between left and right angular distributions $\theta_l = \sum_i \beta_i$ and $\theta_r = \sum_i \alpha_i$ generated by a geodesic at point P on the surface mesh encode the local geometry of the discrete surface mesh at P. For coarse meshes, an additional scheme depicted in (d) is considered to ensure the accuracy of the surface normal computation. This scheme ensures that the resultant normal $\bar{N}_R$ is constrained to lie within the region in red defined by the disc normals $\bar{N}_1$, $\bar{N}_2$ and $\bar{N}_3$.

3.5.1 Self-symmetry characterization

We propose the following metric to characterize self-symmetric regions within a shape X. Two regions $X_1, X_2 \subset X$ are possible symmetric regions within X if for some upper bound ε:

$$\left| \sum_{k=1}^{k_0} \Phi_X^k(p) - \sum_{k=1}^{k_0} \Phi_X^k(q) \right|_2 \leq \varepsilon \quad \forall p \in X_1,\ \forall q \in X_2 \tag{3.3}$$

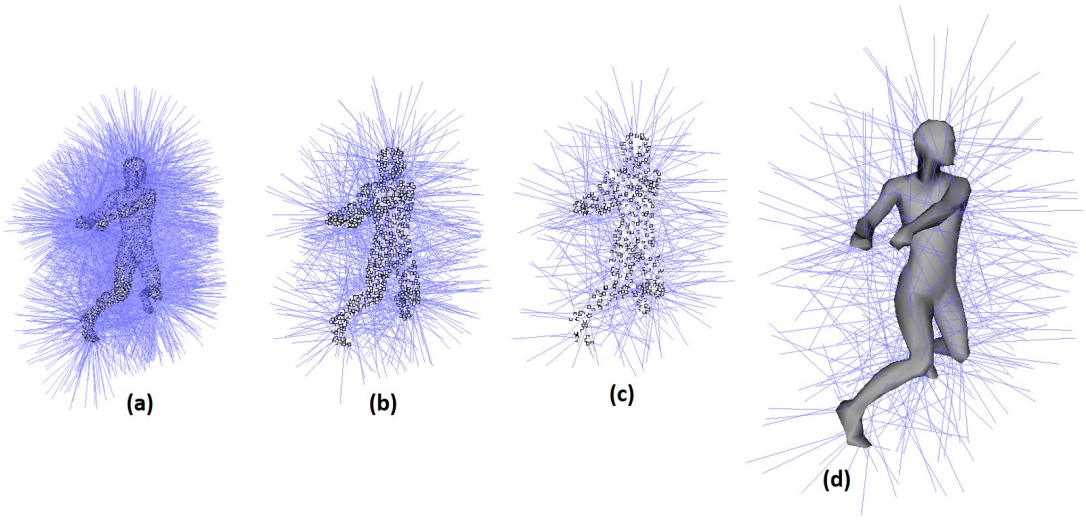

Figure 3.3: Gradual increase in variance of vertex normal due to reduction in vertices from (a) 100% to (b) 75.02% and (c) 87.05%. (d) Due to reduction by more than 87% even in geometrically "flat" region such as human torso the neighborhood vertex normals change direction with high degree.

where $|\cdot|_2$ denotes the $\mathcal{L}^2$ norm. Using spectral analysis one can find a tight bound on ε such that $\varepsilon \leq \sum_{p,q \in X_1,\, r,s \in X_2} |d(p,q) - d(r,s)|_2$ for a C^2 distance metric d (Dunford and Schwartz [1963]). This upper bound on ε is a measure of dissimilarity between regions X_1 and X_2 in terms of the geodesic distances computed between points within the regions. Since the geodesic distances capture the local geometry over the surface, this upper bound, therefore, captures the geometric dissimilarity between regions X_1 and X_2 as well. The parameter ε, aggregated over the entire mesh, indicates the variance of geodesic error computed over the entire shape manifold X. Consequently, ε is a measure of the degree of isome-

try deformation of X vis-a-vis the baseline shape. We report the bounds on ε computed for different meshes in the Experimental Results section (Section 3.6). Since the eigenvectors are ordered (in descending order of their eigenvalues) and lower-order eigenvectors (with larger eigenvalues) are known to effectively capture global shape features, we restrict ourselves to the lower-order eigenvectors such that $k_0 \leq 20$ for characterizing self-symmetry. Furthermore, the above characterization can also be used to jointly analyze the region-wise correspondence between two isometric shapes (Section 3.5.2).

3.5.2 Correspondence determination between isometric shapes

Determining the compatibility between the eigenbases of isometric shape spectra plays a critical role in applications that entail analysis of multiple 3D shapes; in particular, correspondence determination between 3D shapes. In related work, Ovsjanikov et al. [2012] represent the correspondence between two isometric shapes by a parametric map between functional spaces corresponding to the shapes. However, functional map-based methods typically rely on a set of point-wise correspondence maps between shapes provided a priori for optimization of the correspondence criterion (Ovsjanikov et al. [2012]; Nguyen et al. [2011]). In contrast, the proposed approach does not assume knowledge of any prior correspondence mapping between the shapes under consideration.

For correspondence determination between two isometric shapes X and Y we exploit the fact that the eigen decomposition of symmetric shape operators $D_g(X)$ and $D_g(Y)$ leads to approximately commutative eigenspectra Φ_X and Φ_Y respec-

tively. The characterization *"approximately commutative"* is on account of the triangulated discretization of the surface meshes describing the shapes and follows the formal definition given in Section 3.3.4.

We couple Φ_X and Φ_Y by the commutative terms $\Phi_X^T \Delta_Y \Phi_Y$ and $\Phi_Y^T \Delta_X \Phi_X$ to solve the following optimization problem:

$$\bar{\Phi}_X, \bar{\Phi}_Y = \underset{\phi_x, \phi_y}{\operatorname{argmin}} \left\{ |\phi_x^T \Delta_Y \phi_y|_F + |\phi_y^T \Delta_X \phi_x|_F \right\} \tag{3.4}$$

where $\phi_x \subset \Phi_X$, $\phi_y \subset \Phi_Y$; Δ_X, Δ_Y are diagonal matrices of eigenvalues (eqn. (3.2)) corresponding to shapes X and Y, respectively and $|\cdot|_F$ denotes the Frobenius norm. The optimization in eqn. (3.4) considers all pairs of subsets of eigenvectors $\{1, \ldots, k_0\}$ from the eigenspectra of shapes X and Y. It should be noted that eqn. (3.4) does not require that *a priori* correspondence maps be specified. The optimized maps $\bar{\Phi}_X$ and $\bar{\Phi}_Y$ over shapes X and Y encode the corresponding regions between them where corresponding regions are denoted by the same color (generated using a standard colormap library).

From the optimized maps $\bar{\Phi}_X$ and $\bar{\Phi}_Y$, the relative correspondence error between shapes X and Y is given by metric $C_{X,Y} = \sum_{k=1}^{k_0} |\bar{\Phi}_X^k - \bar{\Phi}_Y^k|_2$. To compute $C_{X,Y}$ we consider the lower-order eigenvectors by setting $k_0 \leq 20$. It is to be noted that $C_{X,Y}$ essentially represents the geometric difference due to isometric transformations between corresponding regions of shapes X and Y as captured by the spectrum of the shape representations. Thus, $C_{X,Y}$ is a measure of the degree of *isometric deformation* between shapes X and Y.

3.5.3 Compatibility of the commutative spectrum for deformation transfer

The proposed global shape descriptor is designed to encode the local surface geometry that can be used to establish correspondence between isometric deformations of a shape following commutative optimization as explained in Section 3.5.2. Based on this property of the descriptor, we hypothesize that the commutative spectra can be successfully utilized to generate all continuous deformations of a shape X from initial correspondence between two isometric deformations of X. The experimental setup for testing the hypothesis is explained in Fig. 3.4. The experiment first computes the commutative eigenspectra $\bar{\Phi}_1, \bar{\Phi}_2$ of two baseline isometric deformations S_1 and S_2 of a shape category following the optimization in eqn. (3.4). The optimized eigenspectra are then mapped on a set S, consisting of other isometric deformations $S_3, S_4, ...$ etc. of the baseline shape.

We propose the following metric that evaluates the correspondence established by the commutative eigenspectra $\bar{\Phi}_1, \bar{\Phi}_2$ between all shape pairs $\{S_i, S_j\}$ from set S:

$$D(S) = \frac{1}{|S|} \sum_{\substack{S_i, S_j \in S \\ i \neq j}} C_{S_i, S_j} \tag{3.5}$$

where $|S|$ is the size of the set S and C_{S_i,S_j} is the correspondence error between shapes S_i and S_j as described in Section 3.5.2. This quantitative characterization

$D(S)$ (eqn. (3.5)) is suggestive of whether the commutative shape descriptor spectrum of the baseline shapes can address correspondence between baseline shapes and other isometric deformations of the shape category. This characterization can be useful to effectively address the problem of deformation transfer (Sumner and Popović [2004]; Lévy [2006]; Sumner et al. [2005]).

3.6 Experimental Results

For our experiments we have chosen the TOSCA dataset consisting of eleven non-rigid shape categories, i.e., *Cat*, *Dog*, *Wolf*, two *Human Males*, *Victoria*, *Gorilla*, *Horse*, *Centaur*, *Lioness* and *Seahorse* (Ovsjanikov et al. [2009]). Within each shape category, the individual shapes represent different transformations of the baseline shape such as isometry, isometry coupled with topology change and different mesh triangulations, among others, of the baseline shape. In this work, we consider shapes that differ via an isometry transformation. Some examples of isometry transformations of shapes are shown in Fig. 3.5. Experimental results of each of the applications are formally described in Sections 3.6.1, 3.6.2 and 3.6.3 using visual validation of the results followed by the corresponding numerical evaluations. We have experimented with coarse meshes that are reduced by more than 87% of their original size or resolution. The results of the proposed shape representation are compared with those from relevant state-of-the-art shape representation schemes. The compatibility of the commutative eigenspectra to address deformation transfer is visually validated in Section 3.6.3.

3.6.1 3D self symmetry detection

Fig. 3.6 presents the self-symmetry maps obtained for different shape categories using eqn. (3.3). The maps in Fig. 3.6 correspond to the second eigenvector Φ_X^2 obtained from the spectral decomposition of the global operator $D_g(X)$ for each shape. Table 3.2 presents the self-symmetry characterization measure, denoted by the upper bound ε in eqn. (3.3), for each shape category. This characterization measure represents the deformation between symmetric regions within a shape that the characterization criteria would be able to address as explained in Section 3.5.1.

Table 3.2: Self-symmetry characterization measure for different shape categories in the TOSCA dataset. The average degree of isometry transformation within the category *Seahorse* is observed to be at least 19% higher than the other categories.

Category	ε	Category	ε
Lioness	0.0506	*Dog*	0.0486
Wolf	0.0485	*Michael*	0.0486
Seahorse	0.0603	*Centaur*	0.0485

3.6.2 3D correspondence determination

Since the lower-order eigenvectors represent global shape geometry more accurately, we consider the first 20 eigenvectors to compute the global region-based correspondence between the isometric shapes. Fig. 3.7 shows the results of correspondence determination between the isometric *Human Male* shapes obtained via the optimization criterion described in eqn. (3.4). Except for a small region at lower left leg, correspondence maps between the shapes are shown to be consistent

across eigenvectors of different order. It is to be noted that the eigenmaps for a single shape across different order of eigenvectors are very similar to each other as well. In Fig. 3.7, eigenvectors up to order 9 are shown to demonstrate this consistency both within a shape and between shapes. We also present the result of the commutative correspondence optimization over point cloud data as presented in Fig. 3.8. This provides experimental validation of the fact that the proposed descriptor spectrum effectively captures a global invariance within a shape that is robust to isometric transformations.

Table 3.3: Comparison of average relative correspondence error $C_{X,Y}$ between framework proposed by Das and Bhandarkar [2017] and the proposed method Das and Bhandarkar [2018] for correspondence determination between isometric shapes across different shape categories.

Category	Average $C_{X,Y}$ for framework by Das and Bhandarkar [2017]	Average $C_{X,Y}$ for present approach by Das and Bhandarkar [2018]
Victoria	0.069	0.045
Dog	0.0624	0.0474
Cat	0.06	0.0522
Michael	0.057	0.0363
Horse	0.0559	0.0179
Centaur	0.052	0.0261

The relative correspondence error for these maps can be characterized by the measure $C_{X,Y}$ defined in Section 3.5.2. Table 3.3 lists this measure for isometric shapes from different shape categories. Lower $C_{X,Y}$ values denote a higher degree of correspondence accuracy achieved via the optimization described in eqn. (3.4). We compare our method with recent work Das and Bhandarkar [2017] where the

shape representation is based upon geodesics between mesh vertices described using a Cartesian coordinate system. The proposed method shows significant improvement since the differential representation of the shape vertices capture the local geometry and topology variations more effectively. We emphasize here, that the correspondence accuracy is achieved without requiring any prior mapping between the shapes.

3.6.3 Deformation transfer compatibility characterization

Following the experimental setup described in Fig. 3.4 we tested the compatibility of commutative eigenspectra to address deformation transfer on various shape categories. One such experiment on the *Human* model is described in Fig. 3.9. The experiment first computes the commutative eigenspectra following the optimization in eqn. (3.4) on baseline shapes S_1 and S_2 as shown in Fig. 3.9. Subsequently, the optimized eigenspectra are mapped over different isometric deformations of shapes S_1 and S_2. The visual similarity of the maps suggest that the optimized eigenspectra can be effectively used to generate smooth deformations of baseline shapes and thus can be effectively employed for deformation transfer for the shape category (Lévy [2006]).

The quantitative characterization of this compatibility can be computed using eqn. (3.5). We observed that this metric for different shape categories followed closely the characterization metric depicted in Table 3.3 and was hence not tabulated in this section to avoid redundancy. Table 3.4 compares the performance of the proposed representation scheme with the performance of other state-of-the-art

representation schemes (Das and Bhandarkar [2017]; Kim et al. [2011]; Sahillioglu and Yemez [2011]). Methods proposed by Kim et al. [2011]; Sahillioglu and Yemez [2011] were further combined with the functional map technique by Ovsjanikov et al. [2012] in order to improve their correspondence accuracy via functional map-based local refinement. The results of correspondence for these combined approaches are also presented in Table 3.4. The numerical values presented in Table 3.4 denote the highest percentage correspondence accuracy achieved by the various representation schemes along with the corresponding average geodesic error. The performance of the proposed representation scheme is observed to compare very well with the performance of the other state-of-the-art representation schemes. These results underscore the central hypothesis underlying the proposed shape representation, namely that competitive performance in self-symmetry detection and characterization, and correspondence map determination between isometric 3D shapes can be achieved by the proposed shape representation without requiring prior knowledge of correspondence mapping between the shapes in contrast to other state-of-the-art correspondence determination techniques (Kim et al. [2011]; Sahillioglu and Yemez [2011]).

3.7 Conclusions and Future Work

In this chapter we proposed a global shape representation scheme using quasi-geodesics computed over the entire discrete shape manifold where each vertex of the manifold is represented by its neighborhood-based surface differential coordinates.

Table 3.4: Comparison between the proposed scheme and other state-of-the-art schemes by Das and Bhandarkar [2017], Kim et al. [2011] and Sahillioglu and Yemez [2011]. Correspondence results from methods proposed by Kim et al. [2011], Sahillioglu and Yemez [2011] combined with functional maps(Ovsjanikov et al. [2012]) are also compared.

Methods	Geodesic Error	% Correspondence
Kim et al. [2011]	0.11	~ 95
Ovsjanikov et al. [2012] and Kim et al. [2011]	0.06	~ 95
Sahillioglu and Yemez [2011]	0.25	~ 90
Ovsjanikov et al. [2012] and Sahillioglu and Yemez [2011]	0.2	~ 90
Das and Bhandarkar [2017]	0.15	~ 94
Proposed Scheme	0.27	~ 94.55

The spectral decomposition of this representation is used to identify self-symmetric regions of the shape. By exploiting the commutative property of the eigenbases of the proposed representation, we successfully computed region-wise correspondence between isometric shapes and compared the results to those from state-of-the-art correspondence models. Furthermore, we investigated the effectiveness of the commutative eigenspectra to address smooth deformation transfer between 3D shapes. We also proposed formal metrics for characterization of self-symmetry identification and correspondence determination.

A key contribution of this work is the fact that no prior mappings between shapes was exploited for correspondence and self-symmetry determination. As an extension of the current scheme, we intend to apply the shape representation

model, combined with functional maps (Ovsjanikov et al. [2012]) to address applications such as deformation transfer between isometric shapes in absence of any prior knowledge, and for correspondence determination between near-isometric shapes (Kovnatsky et al. [2013]).

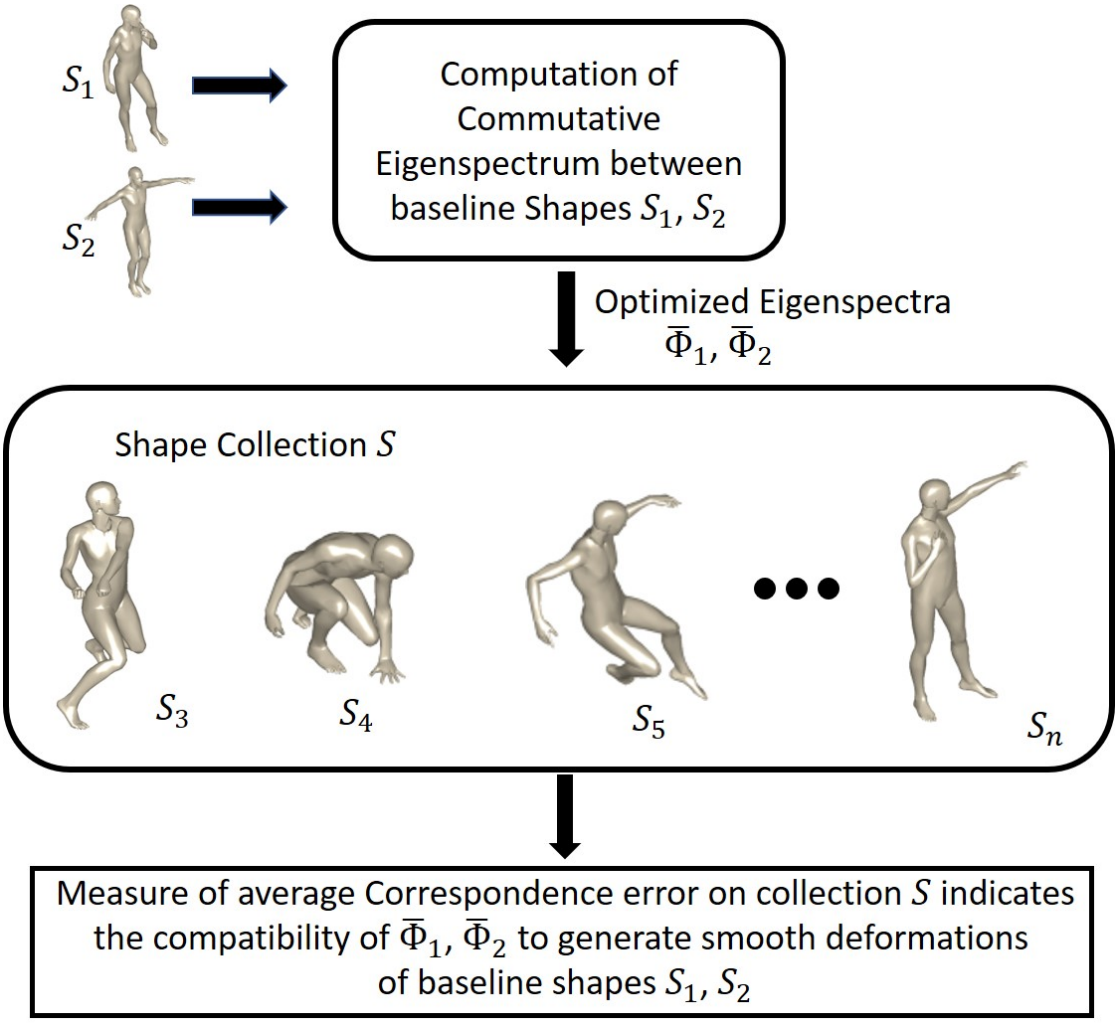

Figure 3.4: Characterization of compatibility of a commutative eigenspectrum to address continuous deformation of baseline shapes.

Figure 3.5: Examples of isometry transformation for the shape categories *Human Male* and *Centaur* from the TOSCA dataset.

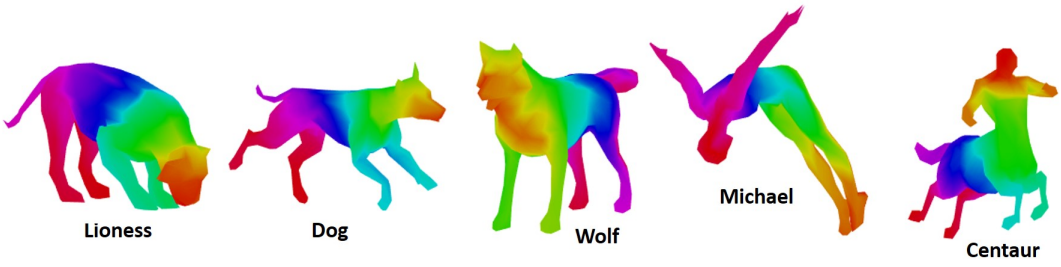

Figure 3.6: Self-symmetry detection for five different shape categories using the spectrum of the global representation $D_g(X)$ for the shape X. Each map corresponds to the second eigenvector Φ_X^2 of the shape operator spectrum.

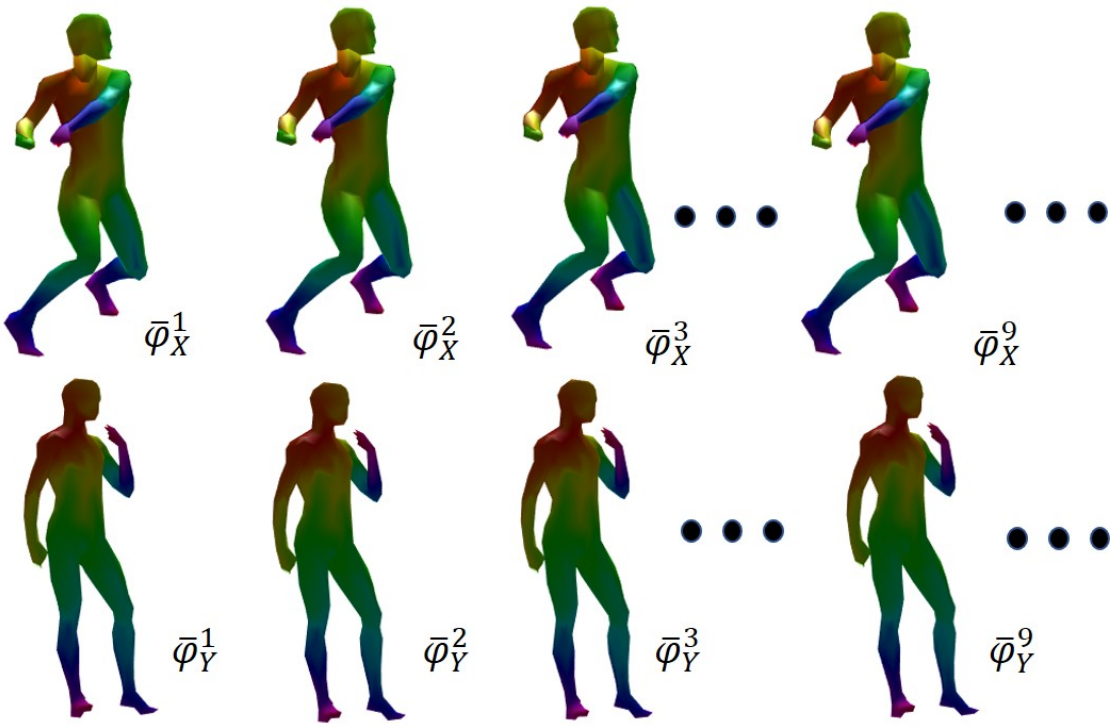

Figure 3.7: Pairwise consistency between corresponding eigenmaps on the isometric deformations of the *Human Male* shapes. For correspondence estimation, the optimization criterion described in eqn. (3.4) is used. Lower-order eigenvectors are considered for correspondence estimation since they effectively capture the global shape geometry. Maps across different order of eigen vectors on the same shape also demonstrate high degree of consistency.

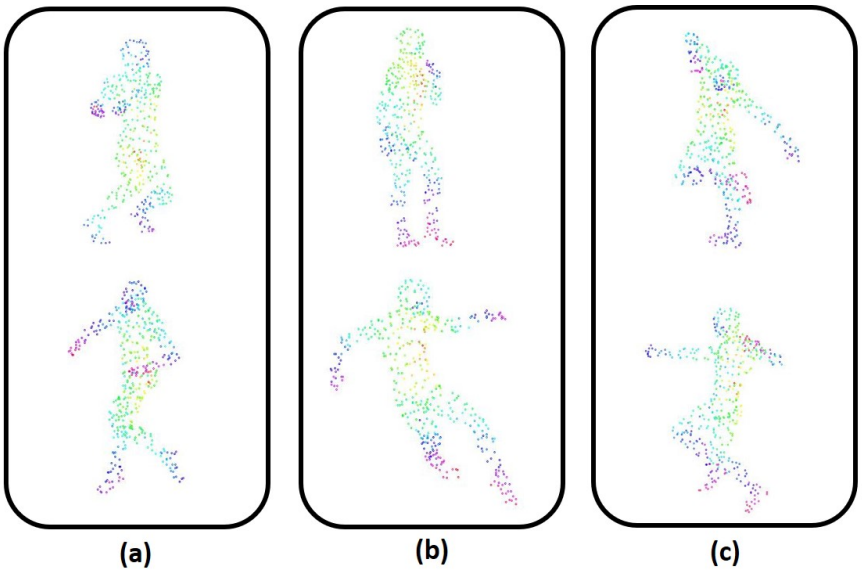

Figure 3.8: Pairwise correspondence for point cloud data representing isometric transformation pairs (a), (b) and (c) for human shapes

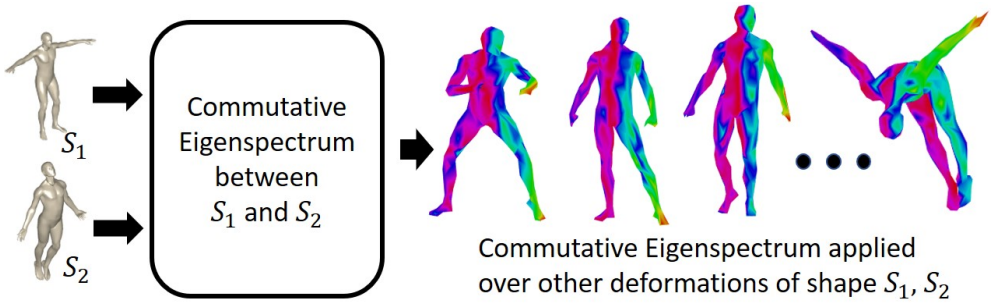

Figure 3.9: Experimental setup to characterize the effectiveness of commutative eigenspectrum for generating smooth deformations of a baseline shape. The results for *Human* models are shown.

Chapter 4

Comparison Between Shape Descriptor Performance, Analysis and Applications

Somenath Das[1], Dr. Suchendra M. Bhandarkar

[1]First Author. To be submitted to ACM Transactions of Graphics (TOG)

4.1 Abstract

In this chapter, we present an experimental analysis to justify the construction of the commutative optimization terms in eqn. (2.5) and eqn. (3.4) that have been successfully employed to establish correspondence between isometric shape pairs. Furthermore, we present a qualitative and quantitative performance comparison between shape representations described in Chapter 2 and Chapter 3 under different noise condition imposed upon the shape data. Some of the noise conditions considered for the comparison are Gaussian Noise, Poisson noise, shot noise, holes and micro-holes. A comparison between feature descriptors resulting from the proposed shape representations and the other well known feature descriptors is also presented. It was shown that the shape representation based feature descriptor performs comparably with the state-of-the-art descriptors. We also apply the shape representation in Chapter 3 to address deformation transfer between shape and conclude the chapter with a qualitative result of the deformation transfer application.

4.2 Symbols Used

The shape representations presented in Chapter 2 and Chapter 3 are fundamentally different despite the similarity of being represented by pairwise geodesics between all pairs of points on the surface. This fundamental difference is due to the fact that in Chapter 2 the shape representation represented the mesh considered vertices by their Cartesian locations. However, for the shape representation

Table 4.1: Symbols to represent shape operators in Chapters 2 and 3

Geodesic distance based surface operator in Chapter 2	S_g
Geodesic based surface representation in Chapter 3 with vertices transformed to surface differential	S_g^δ

in Chapter 3, the vertices are transformed into their surface differential coordinates as described in Fig. 3.2 (a). For the sake of comparison we will adopt two different symbols to represent these shape representation as defined in Table 4.1.

The reminder of the chapter is described as follows. In Section 4.3 some experimental validation using simple graphs is presented to justify the construction behind the commutative optimization terms eqn. (2.5) and eqn. (3.4). We extend these experiments in Section 4.4 to present the capability of the shape representations to capture graph topological features such as spectral diameter and algebraic connectivity. The performance of the representations S_g and S_g^δ under various noise conditions are compared in Section 4.5. Based on the geodesic fields created by spectrum of S_g and S_g^δ we present a point-wise shape feature in Section 4.6 and compare the performance of the shape feature with other relevant shape features using different performance metric. We conclude this chapter with relevant result for S_g^δ applied for shape deformation transfer.

4.3 Effect of Isometric Rigid Transformation and Vertex Ordering on Simple Graph Spectrum

In this section we explore the relations between the spectra of two isomorphic graphs. These graphs are represented as square distance matrices. The distance metric chosen is the L_2 norm between vertices of the graph. We explore the relations between the eigenspectra under two different experimental settings. First, the order of the vertices for these isomorphic graphs are changed. In the second experiment the isomorphic graphs are allowed to undergo affine transformations between them, resulting in different spectra. Subsequently, we study the relations between eigenspectra of isomorphic shapes resulting from these different settings. The result of the experiment shows that a subset of eigenvectors for both shapes shows orthogonality between them. From this observation we propose an optimization criteria to find an optimal set of eigenvectors that can be utilized for correspondence between shapes.

4.3.1 Eigenspectrum Orthogonality under Vertex Ordering

Computational models in computer graphics represent 3D shapes using an ordered list of vertices along with their 3D coordinates that compose the shapes. Based on the ordering of the vertices different different shape representations are computed. Although the appearance of the shapes remains same irrespective of the order of the vertices, the computable shape representations depend on the choices of vertex ordering. For instance let us consider a shape representation where a shape

with n vertices is represented by an $n \times n$ square matrix D where the element D_{ij} represents the L_2 distance between vertices with labels x_i and x_j within the shape. To illustrate, let us consider a simple square with the vertex labels x_1, x_2, x_3 and x_4 such that $x_1 = (1,1), x_2 = (2,1), x_3 = (2,2), x_4 = (1,2)$ as shown in Fig. 4.1(a). The corresponding shape representation is computed as shown by a 4×4 matrix D^l in eqn. (4.1). If the labels of the vertices are changed as shown in Fig. 4.1(b) then the same shape would be represented by a different 4×4 matrix D^r as shown in eqn. (4.1).

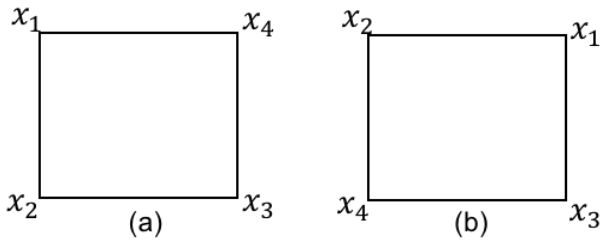

Figure 4.1: Two simple isometric graphs with varying vertex order

Both the matrices shown in eqn. (4.1) are symmetric matrices. Therefore, any pair of eigenvectors obtained from the eigen decomposition of these matrices would be orthogonal. This orthogonality property can be asserted between some eigenvectors of D^l and D^r as well i.e. there should exist one eigenvector v_i^l of D^l and another eigenvector v_j^r of D^r such that $\langle v_i^l \cdot v_j^r \rangle = 0$. However, this property may not hold between all pairs of eigenvectors of D^l and D^r. The **objective** of the experiment in the section is to report the pairs of eigenvectors from D^l and D^r those are orthogonal to each other.

$$D^l = \begin{bmatrix} 0 & 1 & \sqrt{2} & 1 \\ 1 & 0 & 1 & \sqrt{2} \\ \sqrt{2} & 1 & 0 & 1 \\ 1 & \sqrt{2} & 1 & 0 \end{bmatrix}; \qquad D^r = \begin{bmatrix} 0 & \sqrt{2} & 1 & 1 \\ \sqrt{2} & 0 & 1 & 1 \\ 1 & 1 & 0 & \sqrt{2} \\ 1 & 1 & \sqrt{2} & 0 \end{bmatrix} \tag{4.1}$$

The eigenspectra of D^l and D^r are shown by the 4×4 eigenvector arrays E^l and E^l in eqn. 4.2 where each column vector of these matrices represents an eigenvector.

$$E^l = \begin{bmatrix} 0.5 & 0.6996 & 0.1026 & -0.5 \\ -0.5 & -0.1026 & 0.6996 & -0.5 \\ 0.5 & -0.6996 & -0.1026 & -0.5 \\ -0.5 & 0.1026 & -0.6996 & -0.5 \end{bmatrix}; \quad E^r = \begin{bmatrix} -0.5 & 0.7051 & -0.0528 & 0.5 \\ -0.5 & -0.7051 & 0.0528 & 0.5 \\ 0.5 & -0.0528 & -0.7051 & 0.5 \\ 0.5 & 0.0528 & 0.7051 & 0.5 \end{bmatrix} \tag{4.2}$$

We report the result of orthogonality tests between the eigenvectors in eqn. (4.3) where v_i^l and v_i^r are column vectors of E^l and E^r respectively.

$$
\begin{aligned}
\langle v_1^l \cdot v_1^r \rangle &\approx 0 \\
\langle v_1^l \cdot v_2^r \rangle &\approx 0 \\
\langle v_2^l \cdot v_4^r \rangle &\approx 0 \\
\langle v_1^l \cdot v_2^r \rangle &= 0.6523 \\
\langle v_1^l \cdot v_3^r \rangle &= -0.7579\vdots
\end{aligned}
\tag{4.3}
$$

From this result we can conclude that for a pair of isometric graphs (shapes), that vary in vertex order, there exist sets of eigenvectors within the spectrum of each shape such that elements of these sets are orthogonal to each other. These eigenvectors are essential for establishing correspondence between the isometric shapes.

4.3.2 Eigenspectrum Orthogonality under Isometric Transformation

For the second experiment we illustrate the setting in Fig. 4.2 where Fig. 4.2(b) represents an isometric rigid transformation (anticlockwise rotation of $\frac{\pi}{4}$) of the shape in Fig. 4.2(a). The vertices of the square in Fig. 4.2(a) have the same coordinates as of the square in Fig. 4.1(a). However, the transformed shape in Fig. 4.2(b) has coordinates $x_1 = (1, 1), x_2 = (1 + \frac{1}{\sqrt{2}}, 1 - \frac{1}{\sqrt{2}}), x_3 = (1 + \sqrt{2}, 1), x_4 = (1 + \frac{1}{\sqrt{2}}, 1 + \frac{1}{\sqrt{2}})$.

The shape representations for the shapes in Fig. 4.2 following the definitions

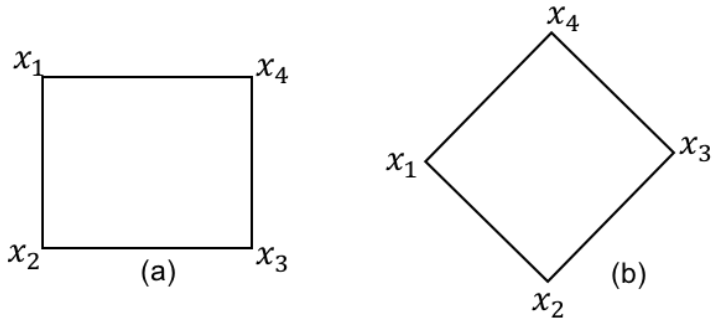

Figure 4.2: Two simple isometric graphs with simple rigid transformations

given in Section 4.3.1, are further decomposed into eigenspectrum described by E^l and E^r in eqn. (4.4).

$$E^l = \begin{bmatrix} 0.5 & 0.7061 & 0.0382 & -0.5 \\ -0.5 & 0.0382 & -0.7061 & -0.5 \\ 0.5 & -0.7061 & -0.0382 & -0.5 \\ -0.5 & -0.0382 & 0.7061 & -0.5 \end{bmatrix}; \quad E^r = \begin{bmatrix} 0.5 & 0.0805 & 0.7025 & -0.5 \\ -0.5 & 0.7025 & -0.0805 & -0.5 \\ 0.5 & -0.0805 & -0.7025 & -0.5 \\ -0.5 & -0.7025 & 0.0805 & -0.5 \end{bmatrix} \tag{4.4}$$

Subsequently, we report the existence of eigenvectors within E^l and E^r that are orthogonal to each other in eqn. (4.5).

$$
\begin{aligned}
&\vdots \\
\langle v_1^l \cdot v_1^r \rangle &\approx 0 \\
\langle v_1^l \cdot v_2^r \rangle &\approx 0 \\
\langle v_2^l \cdot v_4^r \rangle &\approx 0 \\
\langle v_1^l \cdot v_2^r \rangle &= 0.6523 \\
\langle v_1^l \cdot v_3^r \rangle &= -0.7579 \\
&\vdots
\end{aligned}
\tag{4.5}
$$

4.3.3 Common Bases for 3D shapes

The results described in Sections 4.3.1 and 4.3.2 suggest the existence of common bases for pairs of simple shapes those undergo isometric deformation. The results, however, are shown for simple shapes and rigid transformations.

We can, however, extend the results for more complicated shapes under isometric deformation as shown in Fig. 4.3 where two deformable poses of human model are shown. These shapes are also isometric to each other. However, the isometric deformation is non-rigid in nature. One strategy to handle the non-rigid isometric deformation is to adopt an appropriate distance metric, such as geodesic distance, to compute the distance between pairs of vertices on the shape.

Let us assume the shape representations as defined in Section 4.3.1 are computed using the geodesic distance measure between n vertices on the shapes and are represented by $n \times n$ matrices D^X, D^Y for shape X he subsequent eigen de-

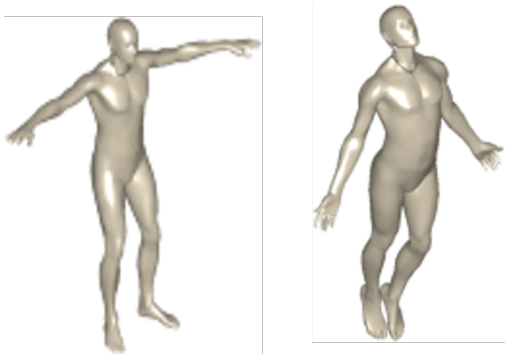

Figure 4.3: Human shape under non-rigid isometric transformations

composition of D^X and D^Y are Φ^X and Φ^Y, respectively.

Therefore, we can expect eigenvectors $\phi_i^X \in \Phi^X$ and $\phi_j^Y \in \Phi^Y$ to exist for shapes X and Y such that $\langle \phi_i^X \cdot \phi_j^Y \rangle \approx 0$.

$$\bar{\Phi}^X, \bar{\Phi}^Y = \underset{\phi_x, \phi_y}{\operatorname{argmin}} \left\{ |{\phi_i^X}^T \Delta_Y \phi_j^Y|_F + |{\phi_i^Y}^T \Delta_X \phi_j^X|_F \right\} \tag{4.6}$$

Following this observation we construct an optimization term in eqn. (4.6) to optimally search for two sets $\bar{\Phi}^X \subset \Phi^X$ and $\bar{\Phi}^Y \subset \Phi^Y$ such that any pair of eigenvectors $\phi_i^X (\in \bar{\Phi}^X)$ and $\phi_i^Y (\in \bar{\Phi}^Y)$ would be orthogonal to each other. Matrices Δ_X and Δ_Y in eqn. (4.6) represents the diagonal eigenvalue matrices for shapes X and Y respectively. The optimization term of eqn. (4.6) use the Frobenius norm $|A|_F$ for matrix A. We emphasize here that existence of such pairs within the spectrum of isometric shape pairs has already been demonstrated

in Sections 4.3.1 and 4.3.2.

4.4 Topological Invariance between Isometric Graphs with Relaxed Vertex Ordering

We inspect in this section the capability of the shape representation S_g^δ to capture graph topological features. For shapes available in the popular shape databases each vertex and faces of one triangulated shape from are represented with unique index. Different shape application pipelines use these indices for the application specific optimization purpose. However, it is desirable that if there exist any topologically invariant feature that can be computationally found it should not be dependent upon the database specific representation such as vertex index, face index etc. We, therefore, specifically apply the spectrum of S_g and S_g^δ to explore whether the representation can capture topological features such as spectral radius and algebraic connectivity between graphs representing isometric deformation of shapes.

We first present the proof of the concept using the following experiment with simple graphs followed by the result of the same experiment over the shape categories available in TOSCA dataset Ovsjanikov et al. [2009].

For the simple experiment we choose two isometrically transformed unit squares with different order of vertices as presented in Fig. 4.4. Due to the relaxation in the order of the vertices there is no particular correspondence between the vertices with the same labels between graphs Fig. 4.4(a) and 4.4(b). Now we represent these

graphs by the pairwise eucliadean distance representation individually following the construction of the shape representation in Chapters 2 and 3 so that the individual graphs are represented by the matrices B_1 and B_2 in eq. 4.7. It is to be noted that for these simple graphs the geodesic distances between non-adjacent vertices is simply the length of shortest sequence of edges connecting them.

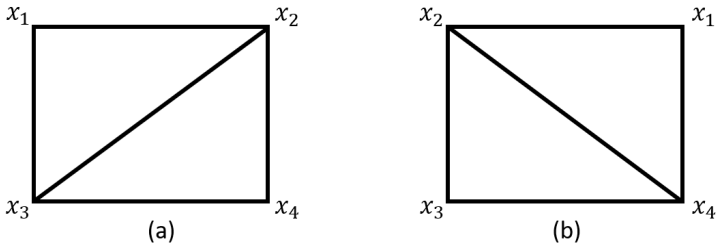

Figure 4.4: Simple isometric graph pairs with topological redistribution of vertices

$$B_1 = \begin{bmatrix} 0 & 1 & 1 & 2 \\ 1 & 0 & \sqrt{2} & 1 \\ 1 & \sqrt{2} & 0 & 1 \\ 2 & 1 & 1 & 0 \end{bmatrix}; \qquad B_2 = \begin{bmatrix} 0 & 1 & 2 & 1 \\ 1 & 0 & 1 & \sqrt{2} \\ 2 & 1 & 0 & 1 \\ 1 & \sqrt{2} & 1 & 0 \end{bmatrix} \tag{4.7}$$

We further decompose the two representations B_1 and B_2 using eigenspectrum to compare the topological features such as spectral radius and algebraic connectivity which are the largest and second largest absolute values of the spectrum respectively. These topological features from the spectrum of B_1 and B_2 are represented in Table 4.2. The equal topological features indicates that the under-

lying shape representation can capture these topological graph invariant features through spectral decomposition.

Table 4.2: Topological features from the simple graph spectra of B_1 and B_2

Spectral Radius		Algebraic Connectivity	
B_1	B_2	B_1	B_2
3.7824	2	3.7824	2

Table 4.3: Topological features for different shape categories from TOSCA dataset. Mean and variance measures are also presented since the meshes considered are discrete and coarse in terms of number of vertices. Parameter values are up to a scale consistent for one shape category.

Shape Categories		Spectral Radius			Algebraic Connectivity		
		Value	μ	σ	Value	μ	σ
Human	Model 1	3.54	3.584	0.275	1.1696	1.1608	0.547
	Model 2	3.6419			1.1785		
	Model 3	3.5695			1.1343		
Dog	Model 1	3.1502	3.203	0.871	1.0581	1.19	0.232
	Model 2	3.3112			1.3543		
	Model 3	3.1487			1.1465		
Horse	Model 1	6.5158	6.5409	0.522	2.3605	2.4056	0.84
	Model 2	6.4846			2.3452		
	Model 3	6.6224			2.5111		
Lioness	Model 1	4.2859	4.232	0.064	1.7332	1.651	0.836
	Model 2	4.2699			1.667		
	Model 3	4.1393			1.5525		

Finally, in this section we represent in Table 4.3 the computed spectral radius and algebraic connectivity features for some of the shape categories from TOSCA dataset. The closeness of both the spectral radius and algebraic connectivity fea-

ture values within one category is reflected by the small variances around the mean values of the feature across different categories. The relatively high variance in the algebraic connectivity parameter could be due to the fact that for the experiment we have considered meshes reduced to more than 87% in terms of number of vertices than its original size. The overall results presented in Table 4.3 emphasize the ability of the proposed geodesic supported shape description scheme to capture graph topological features those remain close under isometric deformation.

4.5 Visual and Quantitative Comparison for Shape Operator Noise Performance

In this section we present a detail analysis of the performance of both shape representations S_g and S_g^δ presented in Chapters 2 and 3 respectively under different noise conditions. Table 4.4 presents in brief the settings for each of the experiment we have considered. The shape correspondence error criterion $C_{X,Y} = \sum_{k=1}^{k_0} |\bar{\Phi}_X^k - \bar{\Phi}_Y^k|_2$ between shapes X and Y with k_0 low order eigenvectors $\bar{\Phi}_X^k$, described in Section 3.5.2 is adopted to quantitatively compare the performance of the operators.

For the noise experiments different scenarios, such as Gaussian noise, Poission noise, shot noise along with holes and micro-holes are considered. A few samples of the noisy meshes we have considered for the experiments are shown in Fig. 4.5. In the following subsections we report the results of each experiment.

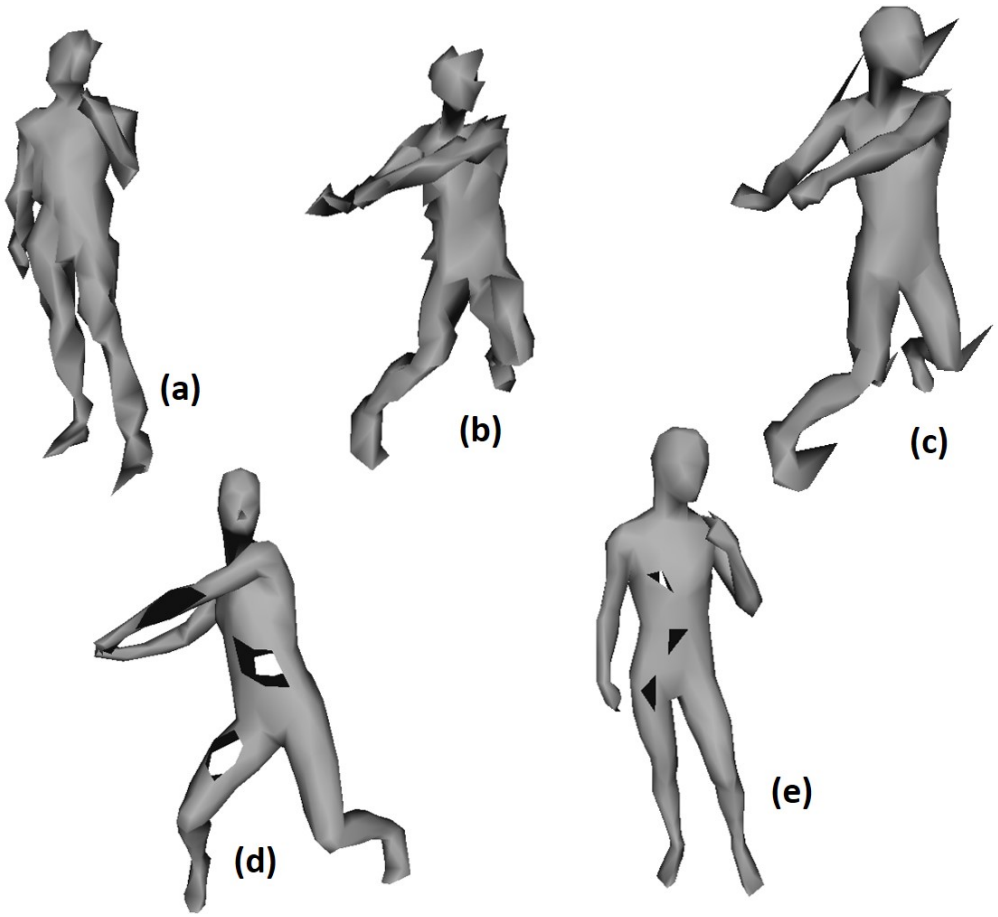

Figure 4.5: Sample noisy meshes used for noise performance evaluation of the shape representation in Chapters 2 and 3. Mesh corrupted with (a) Gaussian noise of zero mean ($\mu = 0$) and variance (σ) = 1.6 added to the mesh vertices, (b) Poisson noise with $\lambda = 5$, (c) shot noise added to 20 randomly selected vertices. Apart from noise, holes and micro holes are also added to the mesh. Two meshes with (d) five holes and (e) five micro holes are shown.

Table 4.4: Description of noise experiments are given in terms of noise power parameter t

Noise Transformation	Description of Noise Power in terms of parameter t. Each transformation repeats for $t = 1, 2, 3, 4, 5$
Gaussian Noise	Noise applied over mesh vertex with mean(μ) and variance(σ) controlled as $\mu = 0, \sigma = 1 + 0.2t$
Poisson Noise	Noise applied over mesh vertex with Poisson distribution parameter t
Shot Noise	High variance in vertex location applied for arbitrarily chose $3t$ vertices.
Holes	Holes of at least one ring width are created around arbitrarily chosen t vertices.
Micro holes	At least one face wide micro holes are crated at arbitrarily chosen t locations.

4.5.1 Gaussian Noise Response

We have considered Gaussian noise $\frac{1}{(1+0.2t)\sqrt[2]{2\pi}} \exp^{-\frac{x^2}{2(1+0.2t)^2}}$ with mean $\mu = 0$ and parametric variance $\sigma = 1 + 0.2t$ for each of the triangulated meshes for the experiment. Furthermore, the noise power has been altered by varying the parameter $t = 1, 2, 3, 4, 5$. For this experiment we have compared the performance of shape representations S_g and S_g^δ and represented the result visually in Fig. 4.6 and Fig. 4.7 respectively. The visual comparison reveals an overall consistency in correspondence determination performance for both the operator under varying degrees of noise power. We may also observe slight degradation in performance for S_g in Fig. 4.6(c) where a small portion of the left leg shows less correspondence

depicted by dissimilar color map.

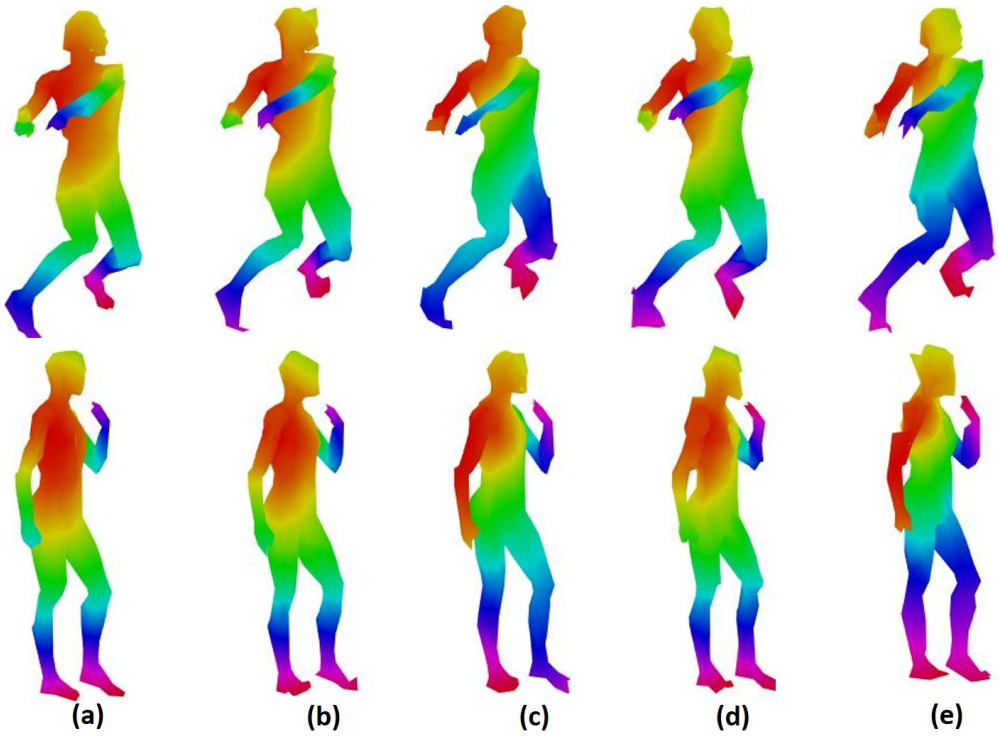

Figure 4.6: Correspondence between isometric human shapes corrupted with additive Gaussian noise for geodesic oriented operator S_g in Chapter 2. The mean of the noise distribution is 0 while the variance is varied gradually from 1.2, 1.4, 1.6, 1.8 to 2 for shapes (a), (b), (c), (d) and (e) respectively.

The quantitative comparison of correspondence performance is presented in Table 4.5. It can be observed from Table 4.5 that the performance is comparable between both the shape representations across different degrees of noise power level. This observation is repeated for the Poisson and shot noise experiment as well. Therefore, for both, Poisson noise and shot noise experiments we have represented only the performance of representation S_g^δ in Sections 4.5.2 and 4.5.3.

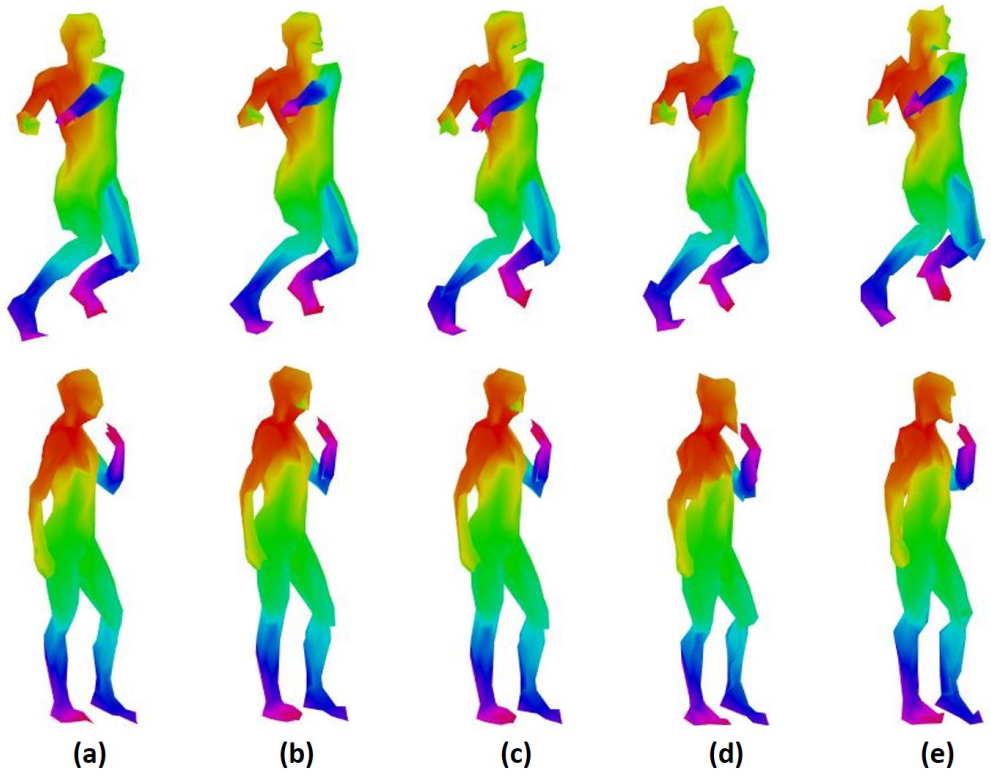

Figure 4.7: Correspondence between isometric human shapes corrupted with additive Gaussian noise for geodesic and differential coordinate supported shape operator S_g^δ in Chapter 3. The mean of the noise distribution is 0 while the variance is varied gradually from 1.2, 1.4, 1.6, 1.8 to 2 for shapes (a), (b), (c), (d) and (e) respectively.

4.5.2 Poisson Noise Response

To parametrically control the noise level at each vertices of the mesh we have considered the Poisson distribution $P(x) = \exp^{-t} \frac{t^x}{x!}$ with mean parameter t varying from $t = 1, 2, 3, 4, 5$. In this section we present the visual and quantitative

Table 4.5: Correspondence performance comparison between S_g and S_g^δ under Gaussian noise.

Shape Representation	Noise level t				
	$t=1$	$t=2$	$t=3$	$t=4$	$t=5$
S_g	0.8254	0.8165	0.8129	0.8206	0.8125
S_g^δ	0.8489	0.8242	0.8414	0.8427	0.8374

performance evaluation for S_g^δ in Fig. 4.8 and Table 4.6 respectively.

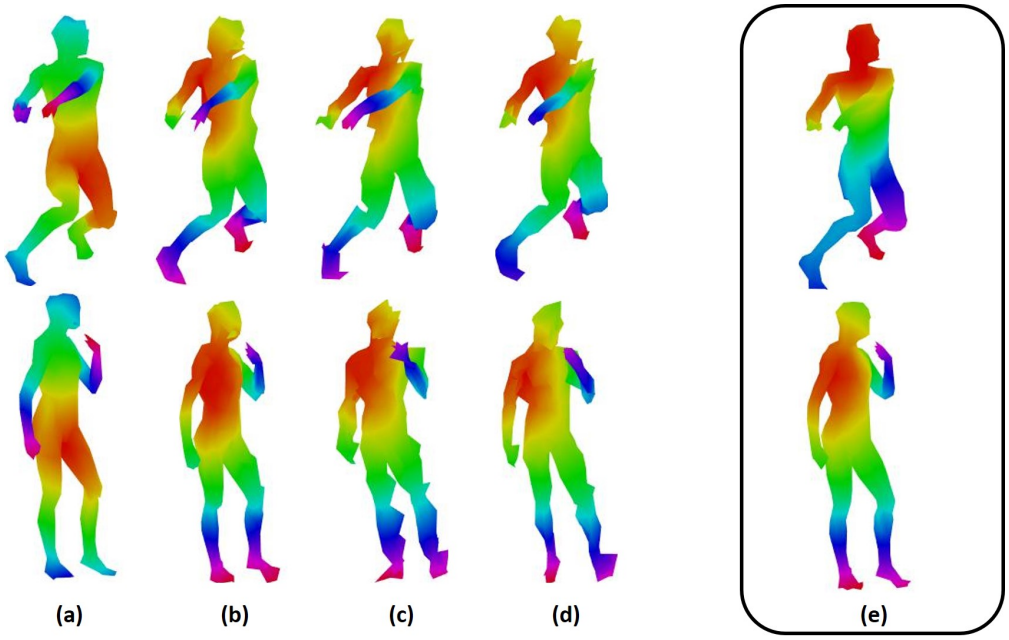

Figure 4.8: Correspondence between isometric human shapes added with Poisson noise with parameter t = (a) 1, (b) 2, (c) 3, (d) 4 and (e) 5. This response is only due to the differential operator presented in Chapter 3. The correspondence shows consistency for (a), (b), (c) and (d) whereas (e) shows a case for $t = 1$ where visual correspondence consistency is less than the other cases.

Table 4.6: Correspondence performance for S_g^δ under Poisson noise.

Shape Representation	Noise level t				
	$t=1$	$t=2$	$t=3$	$t=4$	$t=5$
S_g	0.806	0.8317	0.8182	0.8106	0.8224

Table 4.7: Correspondence performance for S_g^δ under shot noise.

Shape Representation	Noise level t				
	$t=1$	$t=2$	$t=3$	$t=4$	$t=5$
S_g^δ	0.8159	0.8156	0.8164	0.8129	0.8265

The performance evaluation criterion is observed consistent across varying degree of noise in Table 4.6. However, we show a correspondence failure case in Fig. 4.8(e) for mean parameter $t = 1$ for this particular isometric human pair.

4.5.3 Shot Noise Response

Shot noise for 3D meshes is represented by sudden significant changes in locations of the mesh surface vertices. In this experiment with shot noise we parametrically control the maximum change in 3D location of randomly chosen vertices on the surface mesh with $5t$ distance units for parameter $t = 1, 2, 3, 4, 5$. Under the high variance of location the correspondence performance is mostly consistent across varying degrees of noise power as shown in Fig. 4.9 except for a small region around the head in Fig. 4.9(b) and (c).

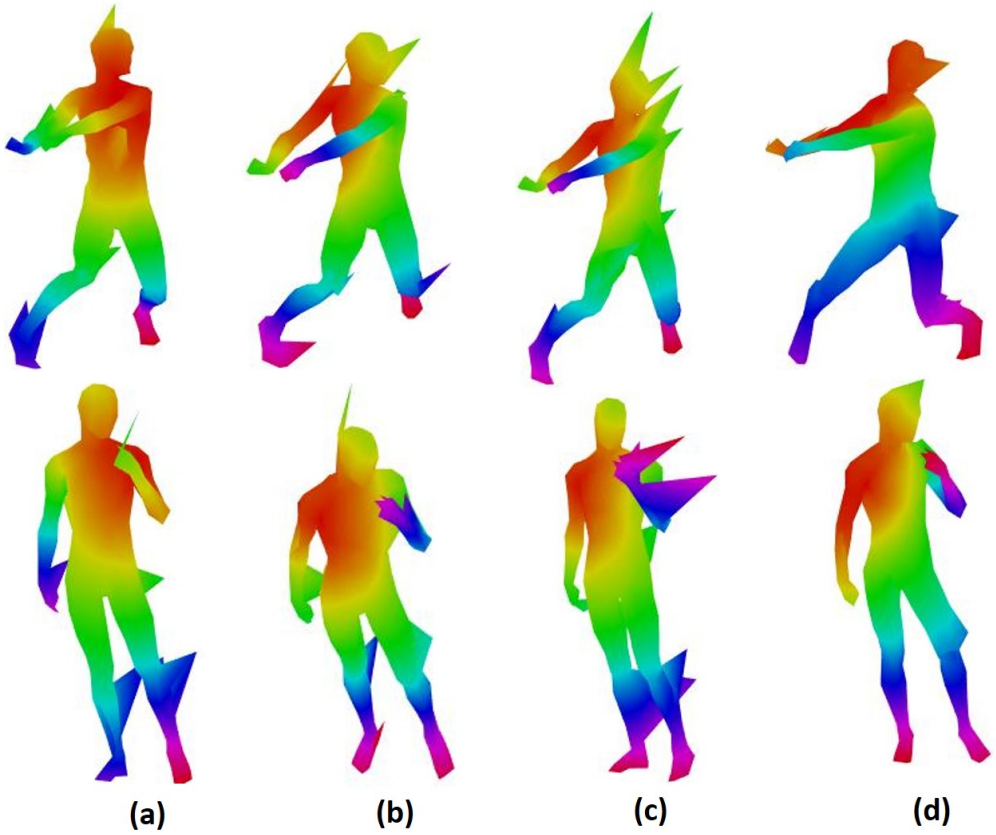

Figure 4.9: Correspondence between isometric shapes under shot noise. The correspondence response is for the differential operator presented in Chapter 3. The maximum amplitude deviation for the randomly selected surface points added with shot noise are (a) 15, (b) 20, (c) 25 and (d) 5 distance units.

The quantitative performance evaluation criterion in Table 4.7 reflects the consistency shown in Fig. 4.9 as well.

Table 4.8: Correspondence performance comparison between S_g and S_g^δ with t holes created on the surface mesh.

Shape Representation	Noise level t				
	$t=1$	$t=2$	$t=3$	$t=4$	$t=5$
S_g	0.8199	0.826	0.8258	0.8213	0.824
S_g^δ	0.8140	0.8123	0.8184	0.8156	0.8226

4.5.4 Noise Response with Holes in the mesh

For this experiment we have considered meshes with varying degrees of surface area. The variation of the mesh surface area is due to different number of punctured holes on the surface. In this experiment we refer the number of holes as the degree of noise. The meshes with holes were created using Meshlab v1.3.2. The average relative variation in the surface area between original mesh and meshes with varying number of holes ranges between 1.6415% to 4.72%.

We have observed that for experiments with holes on the surface, the performance of S_g^δ deteriorates in comparison to representation S_g. In Fig. 4.10 we represent the performance for S_g^δ where we can observe that for the surface area of the meshes with less geometric variation the correspondence is consistent. However, for the extreme part of the surface such as hands and legs the correspondence detection performs poorly. In comparison to the correspondence performance of S_g^δ in Fig. 4.11 we present the correspondence maps obtained for S_g that is more consistent in comparison to Fig. 4.10 across varying number of holes on the surface.

The correspondence evaluation criterion for both the shape representation is

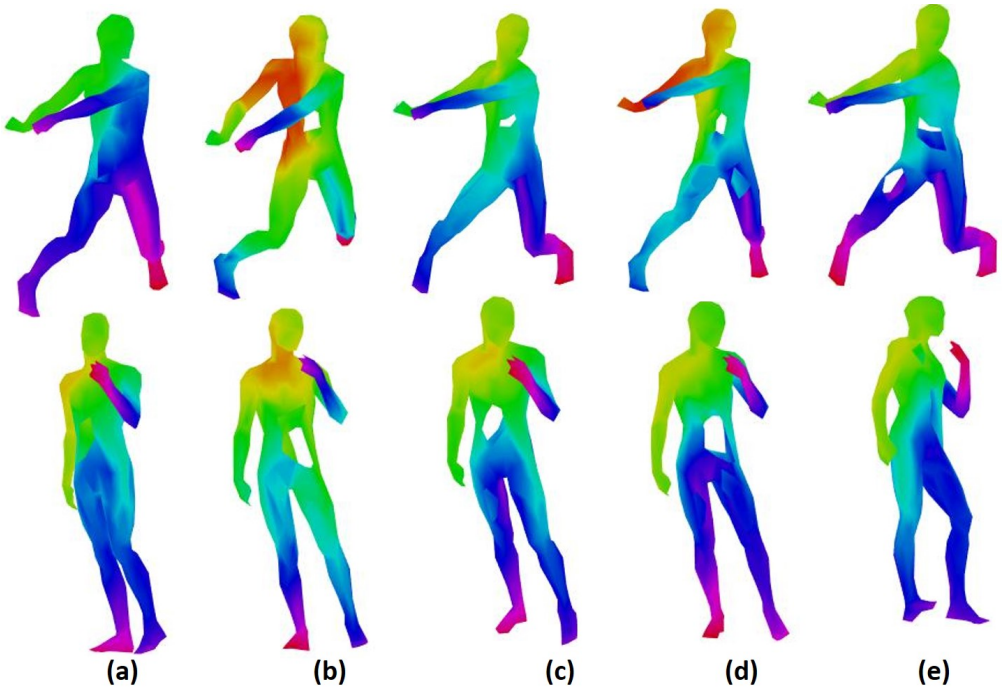

Figure 4.10: Correspondence between isometric human shapes with varying number of holes on the surface. The correspondence maps are for the differential shape operator S_g^δ in Chapter 3. Correspondence maps are for shapes with (a) 1, (b) 2, (c) 3, (d) 4 and (e) 5 holes. The response are inconsistent across varying number of holes though maps (c) and (e) shows higher consistency than the rest of the cases.

presented in Table 4.8.

4.5.5 Noise Response with Micro-Holes in the mesh

Similar to the experimental setup described in Section 4.5.4 we have considered meshes with micro-holes with relative change in surface area from the original mesh

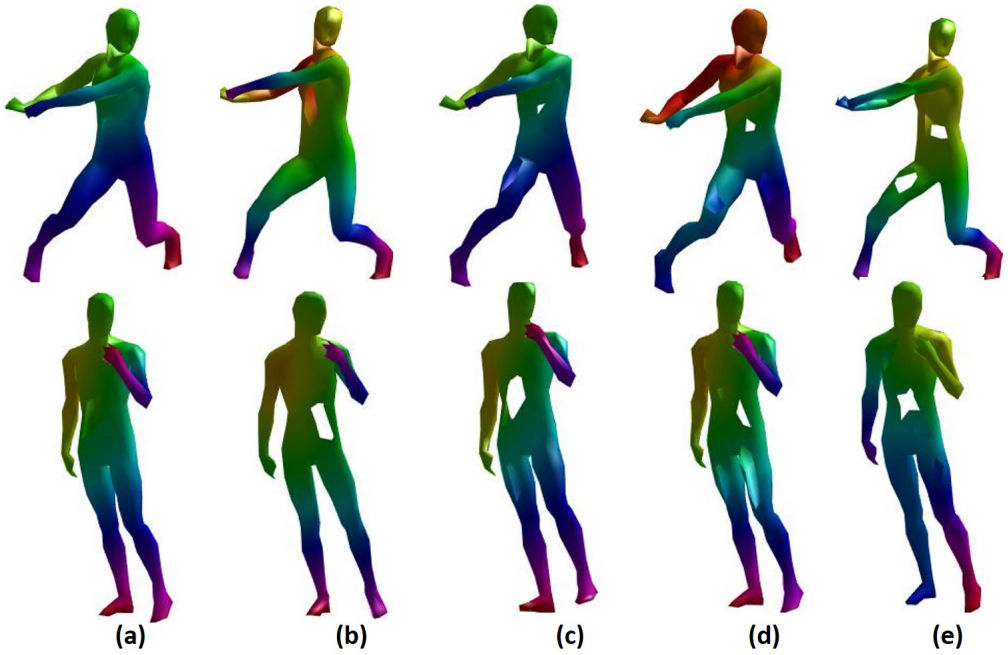

Figure 4.11: Correspondence between isometric human shapes with varying number of holes on the surface. The correspondence maps are for the differential shape operator S_g in Chapter 2. Correspondence maps are for shapes with (a) 1, (b) 2, (c) 3, (d) 4 and (e) 5 holes. The correspondence maps show better visual consistency in comparison to Fig. 4.10

ranging from 0.07% to 1.3954%. The performance of correspondence detection for both the operator S_g and S_g^δ are presented in Fig. 4.13 and Fig. 4.12 respectively. Both the figures show correspondence consistency though for representation S_g the performance deteriorates marginally. This marginal difference can be verified visually from Fig. 4.13 where portion of the left hand was not properly detected by representation S_g whereas in Fig. 4.12 the correspondence consistency is much

prominent.

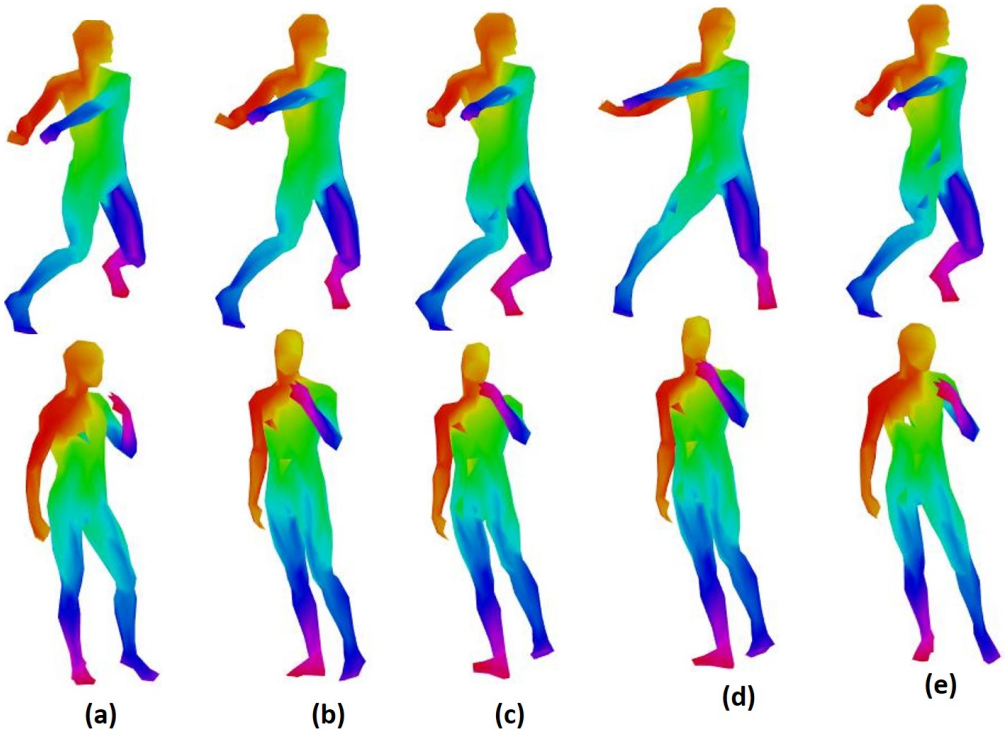

Figure 4.12: Correspondence between isometric human shapes with varying numbers of micro holes. The number of micro holes are (a) 1, (b) 2, (c) 3, (d) 4 and (e) 5 respectively. This response is due to differential surface operator in Chapter 3.

Table 4.9 represents these observations quantitatively where the correspondence error is consistent for both the representations whereas for S_g^δ the correspondence error is marginally less.

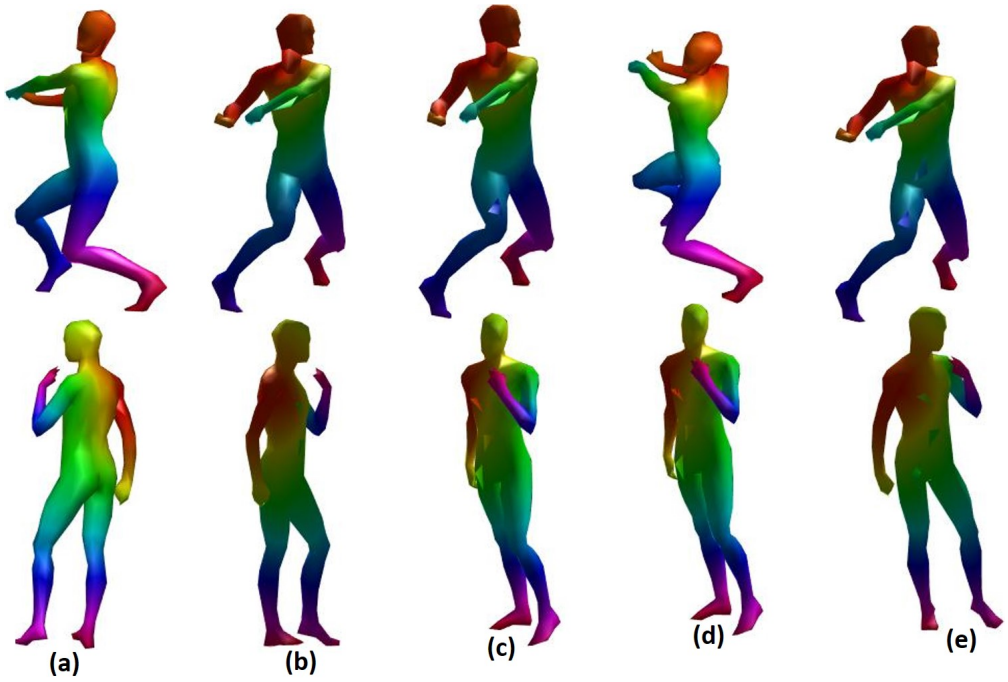

Figure 4.13: Correspondence between isometric human shapes added with with (a) 1, (b) 2 (c) 3, (d) 4 and (e) 5 micro holes, respectively. This correspondence response is generated from the spectrum of geodesic supported operator in Chapter 2. Visually the maps are far more consistent in comparison to the maps of Fig. 4.12

4.6 Geodesic Field based surface features and relevant performance comparison

In this section we propose a shape feature point descriptor based on the geodesic distance field due to surface differential based shape representation S_g^δ. Geodesic fields created around one central surface point (highlighted in red) are shown in Fig. 4.14 for different isometric transformations of human shape. It is to be noted

Table 4.9: Correspondence performance comparison between S_g and S_g^δ with t micro holes created on the surface mesh.

Shape Representation	Noise level t				
	$t=1$	$t=2$	$t=3$	$t=4$	$t=5$
S_g	0.8179	0.8179	0.8179	0.8179	0.8179
S_g^δ	0.8104	0.8104	0.8104	0.8104	0.8104

that the shape operator S_g^δ represents together all such possible geodesic fields over a surface mesh. As previously mentioned in Section 3.5 we further spectrally decompose this composite geodesic field presented by S_g^δ over shape X following eigen decomposition given in eqn. (4.8).

$$S_g^\delta(X)\Phi_X = \Delta_X \Phi_X \tag{4.8}$$

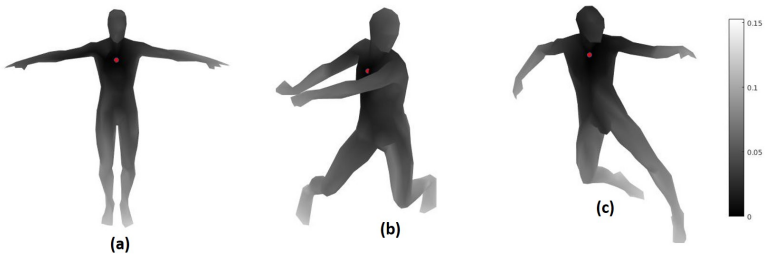

Figure 4.14: Geodesic fields for vertex point marked in red is shown for different isometric transformations (a), (b) and (c) of human model.

Based on the spectral decomposition in eqn. (4.8) we propose the feature

descriptor for a surface point p on shape X as given in eqn. (4.9). The feature descriptor represents a biharmonic density estimate as defined proposed in Mukhopadhyay and Bhandarkar [2017] influenced by biharmonic distance estimate by Lipman et al. [2010b]. However, in the proposed feature descriptor the spectra used to compute the feature value at surface point p is due to the surface representation S_g^δ as mentioned in eqn. (4.8).

$$S_g^\delta(p) = \sum_{k=0}^{k_0} \frac{|\Phi_X^k|^2}{{\Lambda_X^k}^2} \tag{4.9}$$

where Φ_X^k is the k^{th} eigen vector from the spectrum of S_g^δ applied over shape X and Λ_X^k is the corresponding k^{th} eigenvector from the spectrum. We have restricted to lower order $k_0 = 20$ eigenvectors. The lower order vectors tend to characterize global shapes more accurately. Therefore, this constraint over lower order vector should give us top feature points well distributed over the shape that represents collectively the global surface geometry of the shape. We refer to this shape point feature as Differential Surface based Biharmonic Density Estimate Signature (DSBDE).

4.6.1 Repeatability Comparison

We have considered TOSCA and SHREC 2011 databases for shape feature comparison with other well known shape features such as HKS ([Ovsjanikov et al., 2010]) and WKS (Aubry et al. [2011]) under different noise and geometry conditions.

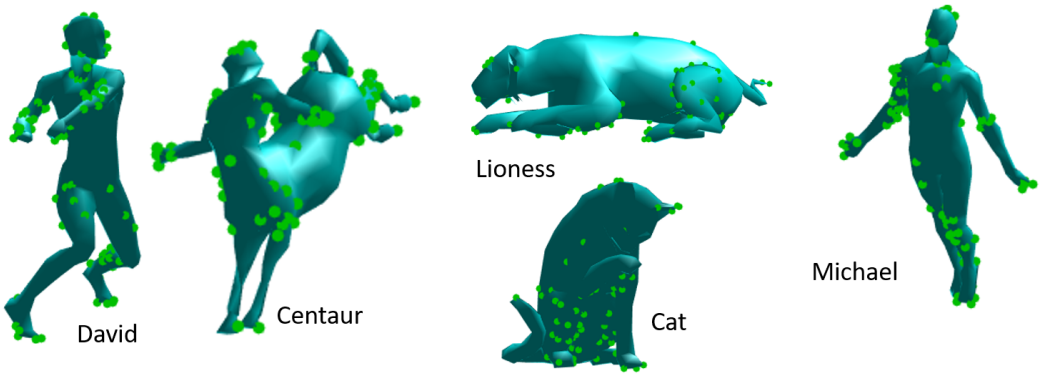

Figure 4.15: Top feature detected by biharmonic density based feature descriptor described in eqn. (4.9) for different shape category. The top detected points tend to concentrate around a region with high local variation in Geometry.

For the comparison repeatability measure was considered. Repeatability of feature point detection is the percentage of detected feature points on the test shape those lie within a ball of radius of 1% of the surface area around the corresponding points on the baseline shape of the category.

Some top feature points detected by this feature descriptor is shown in Fig. 4.15. These top feature points are found concentrated around regions with high variation in local geometry. We further compare the performance of the proposed shape representations S_g and S_g^δ with other state-of-the-art shape feature descriptors such as Heat kernel signature (Ovsjanikov et al. [2010]), Wave kernel signature (Aubry et al. [2011]) etc. For performance comparison experiments we have considered different criterion such as performance evaluation under noise conditions that we

Table 4.10: Repeatability Comparison for detected shape features with HKS (Ovsjanikov et al. [2010]) and WKS (Aubry et al. [2011])

Transform	Type	Shape Features	Noise Power				
Isometric	Geometry	HKS	100	100	100	100	100
		WKS	100	100	100	100	100
		DSBDE	100	100	100	100	100
Gaussian	Noise	HKS	100	95.19	93.16	89.37	85.77
		WKS	100	98.31	92.64	87.57	84.90
		DSBDE	100	99.69	98.74	98.29	95.25
Poisson	Noise	HKS	-	-	-	-	-
		WKS	-	-	-	-	-
		DSBDE	100	99.46	99.04	98.52	97.37
Shot	Noise	HKS	100	95.30	90.03	82.10	74.38
		WKS	100	97.64	94.55	91.32	87.30
		DSBDE	100	99.98	99.95	98.26	96.98
Holes	Noise	HKS	80.54	79	75.25	72.1	69.99
		WKS	88.50	82.65	78.62	72.82	71.40
		DSBDE	92.977	91.56	90.36	89.81	86.49
Micro-holes	Noise	HKS	100	100	99.45	97.58	97.12
		WKS	100	100	99.32	96.91	96.03
		DSBDE	100	100	100	100	100

presented in Section 4.5.

4.7 Application of Shape Representation for Deformation Transfer between Isometric Shapes

4.7.1 Introduction and Problem Statement

In computer graphics and animation industry deformation transfer refers to an application of fundamental importance that is primarily applied over shape meshes to produce their varying deformations. Formally, given two shape meshes S and S_e of some given character the deformation transfer model computes and transfers the deformation variation between them to a target mesh T to generate a deformation T_e that qualitatively resembles to that of mesh S_e. A few examples of sample deformation transfers is shown in Fig. 4.18 where different expressions of source mesh is transferred to the target mesh to produce the matching expressions for the target mesh. One of the most influential paper in this field by Sumner et al. [2005] addresses the problem using an affine transformation minimization framework. This approach attempts to minimize variance of the affine transformation of each face on the deformed mesh in comparison to it's neighborhood. This principle is shown visually in Fig. 4.16(a) where the affine transformation T_i and displacement d_i applied over a triangular face i takes the vertex v of the face to a new deformed vertex position $\tilde{v} = T_i v + d_i$. By minimizing the position variation of $\tilde{v}$ with respect to its neighbors the optimization approach minimize the surface reconstruction

error of the deformed mesh. For efficiency improvement and ease of computation Sumner et al. [2005] adds auxiliary vertices x and $\tilde{x}$ to faces i and $\tilde{i}$ respectively to guide the transformation. This modification helps redefine the optimization process to be applied over surface vertices rather than on faces.

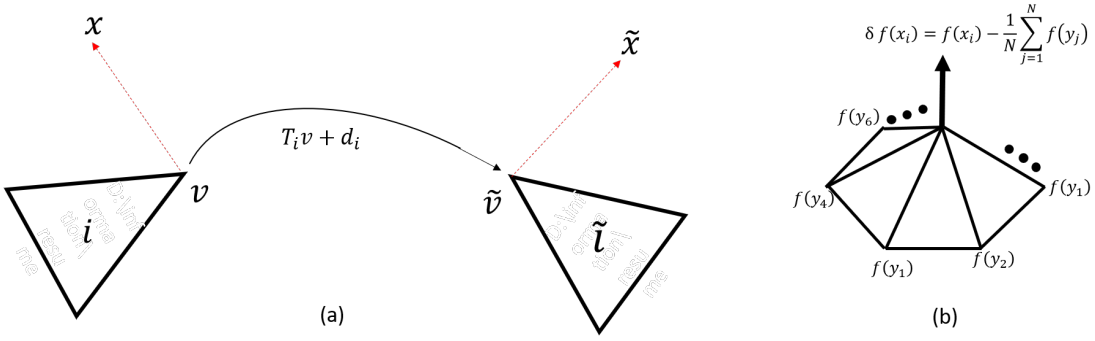

Figure 4.16: Deformation schemes by Sumner et al. [2005] that encodes affine deformation between face i and $\tilde{i}$. To facilitate optimization each triangular face was added with an additional vertex x and $\tilde{x}$ as shown in figure (a). The shape representation due to S_g^{δ} in Chapter 3 due to it's construction naturally encodes the surface differential at each vertex as shown in (b) and no further addition of vertex per face (as opposed to Sumner et al. [2005]) is required.

One implicit advantage the proposed deformation transfer method has over framework proposed by Sumner et al. [2005] is that the surface is defined by the surface differential as shown in Fig. 4.16 (b). Due to this representation vertex coordinates aligns with the normal direction at the vertex and therefore the surface representation naturally lends itself to the deformation transfer optimization without the requirement of an additional mechanism of auxiliary vertices added to the faces as shown in Fig. 4.16(a).

4.7.2 Model

In this section we explain the deformation transfer pipeline using the model described in Fig. 4.17. The framework first (A) computes the deformation between source mesh reference and source mesh final deformation using the optimization criteria given in eqn. (4.10).

$$\tilde{V} = \underset{\tilde{v}_{s_1},\tilde{v}_{s_2},...,\tilde{v}_{s_N}}{\operatorname{argmin}} \sum_{i=1}^{N} ||S_{s_i} - \bar{S}_{s_i}||_F \tag{4.10}$$

where s_is are sample vertices chosen over source mesh S and source expression $\bar{S}$. The deformation is represented by $\tilde{V}$ that essentially represents the deformation in terms of affine transformations present at sample vertices $\tilde{v}_{s_1}, \tilde{v}_{s_2}, ..., \tilde{v}_{s_N}$.

Finally, through the given N correspondences (shown by B in Fig. 4.17) between source shape S and target shape T we transfer the deformation represented by $\tilde{V}$ to the target shape following a surface registration process (C) by minimizing optimization term in eqn. (4.11). The final deformed target shape is represented by block D in Fig. 4.17.

$$min_{\tilde{v}_{t_1},\tilde{v}_{t_2},...,\tilde{v}_{t_N}} \sum_{i=1}^{N} ||\bar{S}_{s_i} - T_{t_i}||_F \tag{4.11}$$

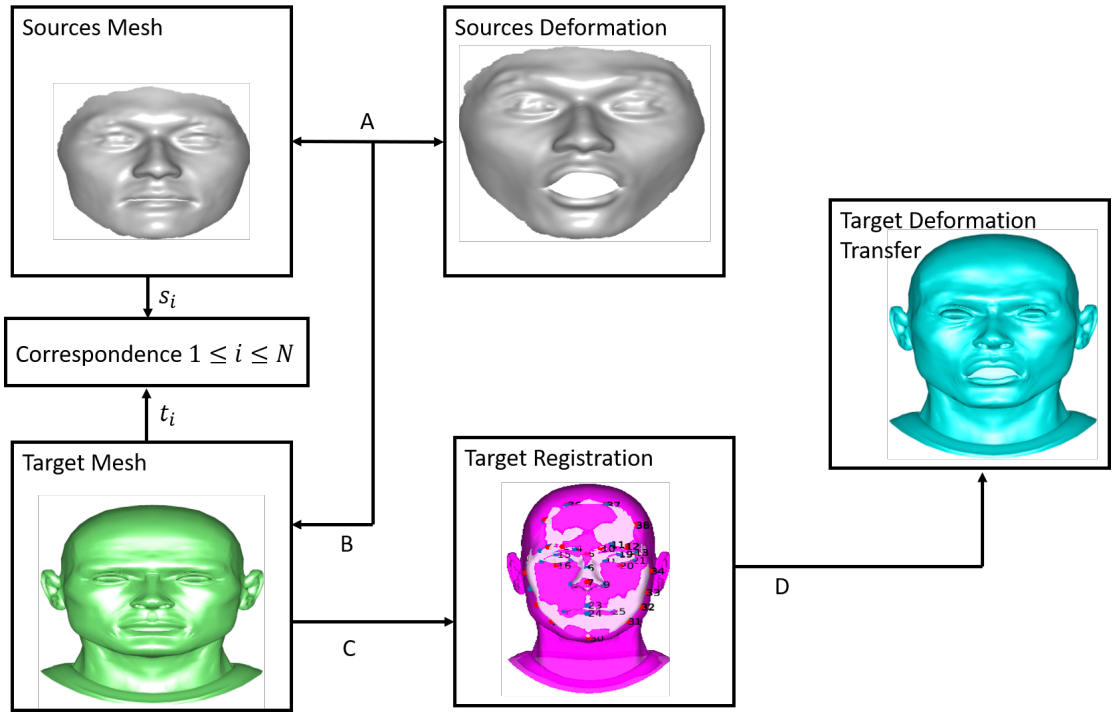

Figure 4.17: A Deformation Transfer Pipeline

4.7.3 Qualitative Results

The model is applied over different facial expressions provided in dataset pop [2004]. The average vertices and faces on the face meshes are 29299 and 58836 respectively.

The qualitative results for some facial expressions such as surprise, laugh, cry and sad faces are shown in Fig. 4.18. The results verify the effectiveness of the shape representation S_g^δ for deformation transfer.

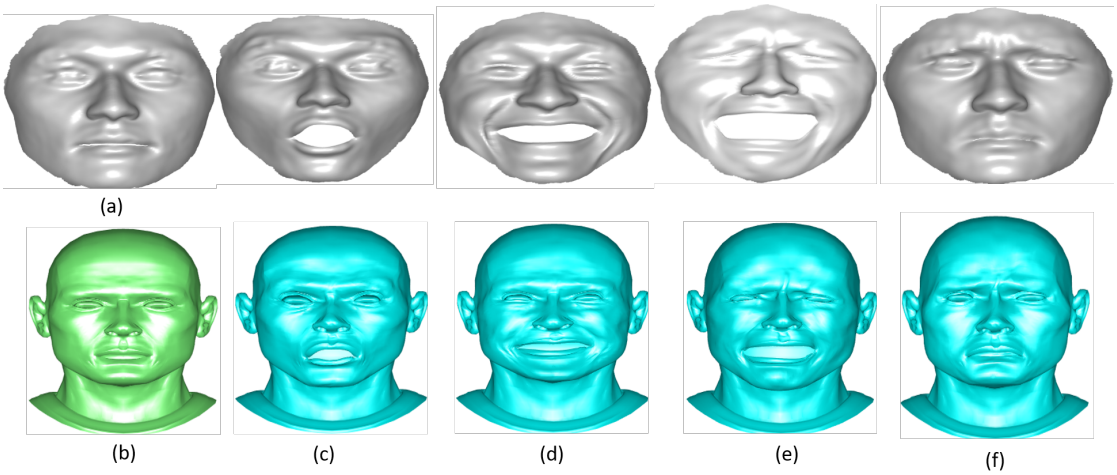

Figure 4.18: Final deformation transfer between (a) source reference to (b) target reference across (c) surprise (d) laugh (e) cry and (f) sad faces.

Acknowledgements

The authors wants to thank web library suw [2018] for providing Matlab libraries to support deformation transfer.

Chapter 5

A Motion Guided Adaptive Approach for Factorization Based NRSfM

Somenath Das[1], Dr. Suchendra M. Bhandarkar

[1]First Author. To be submitted to IEEE Transactions of Pattern Analysis and Machine Intelligence (TPAMI)

5.1 Abstract

Non-Rigid Structure from Motion (NRSfM) is one open ended problem for researchers in the computer vision community that seeks to perceive a movement of a non-rigid moving object from a video sequence like humans do. Vision community refers to wide ranges of movement as non-rigid. They may be movement of a human being, wild horse, running dog etc. or simply folding of a paper etc. Researchers from different schools of thought tries to implement their perception of the non-rigid motion capture problem through a set of hypothesis. In this chapter, we propose a novel optimization term for NRSfM that imposes motion constraint over non-rigid deformation across frames. The proposed optimization jointly solves for 3D shape and camera pose sub-space using Singular Value Decomposition (SVD) based factorization method, combined with motion constraint model.

5.2 Introduction

A wide range of applications in computer vision critically depends on approximate estimation of 3D shape from 2D images using motion information. This problem is more commonly known as Structure from Motion (SfM) or monocular simultaneous localization and mapping (SLAM). SfM typically aims at jointly optimizing 3D locations and camera motion trajectories from a set of observation points over temporally related image stream. Many stable schemes such as factorization applied over monocular image streams (Tomasi and Kanade [1992]) use

camera orthographic constrains for an optimized solutions. Modern approaches to SfM aims at 3D shape recovery from multi-view images by minimizing camera re-projection error for multiple images, a technique commonly known as bundle adjustment. Some prominent works in this direction are by Wilson and Snavely [2014]; Crandall et al. [2011]. However, the scope of applicability of SfM lies mainly within the domain of rigid shapes going through affine or linear transformations between images and therefore, cannot address non-rigid shape deformations that is more commonplace in human experience.

Non-Rigid structure from motion (NRSfM) refers to the problem of extracting 3D non-rigid deformation from the 2D image sequences. Well studied standard solutions for structure from motion (SfM) are not suitable for NRSfM setting since the temporally varying target points across the image sequences are allowed deform in pose and motion. This flexibility in deformation makes NRSfM an ill-posed problem due to many existing ambiguities. These ambiguities can occur due to linear transformations such as rotation or reflection over non-rigid deformation may result in non-unique correspondence between frames. Similarly, non-rigid deformation may not give a fixed shape basis that can be applied for all deformations across frames to extrapolate final 3D shape. Due to these natural ambiguities additional constraints are necessary to solve the problem within a well-posed problem setting where constraint set is at least same as large as the unknowns.

Amongst other solutions for NRSfM a large variety implements camera orthographic projection oriented approaches, otherwise popular in SfM settings, combined with additional constraints. One of the earlier practical solution in NRSfM

(Torresani et al. [2008]) effectively used orthography based factorization method due to Tomasi and Kanade [1992] combined with a lower rank basis shape assumption. Likewise many state-of-the-art solutions to NRSfM enforce spatial or temporal constraints viz. shape prior by Tao et al. [2012]; Tao and Matuszewski [2013], trajectory priors (Akhter et al. [2011]; Gotardo and Martinez [2011a]) etc. for optimizing a practical solution for NRSfM.

In this work we combine camera orthographic projection based factorization combined with temporally related spectral shape priors to impose a motion and local shape constraint over the 2D shape correspondences across frames. Factorization based approach impose a low-rank shape constraint for each frame to extrapolate 3D shape across frames following the seminal work in NRSfM by Bregler et al. [2000]. In addition we exploit the possible orthogonality between shape basis across frames that function as a motion (and shape) constraint over the image streams. Our motivation behind his framework is the observation that temporally deforming shape cannot deform arbitrarily. However, in comparison to some related approaches by Bartoli et al. [2008]; Del Bue [2008]; Akhter et al. [2009a] the present method can address large deformations due to the flexibility of the spectral structure imposed upon the final optimization.

The rest of the chapter is arranged as follows. In Section. 5.3 we cite the most prominent work in this field with a motivation to provide a brief taxonomy of the literature. Section. 5.4 the present approach is elaborated followed by the result on standard dataset in Section. 5.5. We conclude this chapter in Section. 5.6 with the possible extension of this work.

5.3 Related Work

The state-of-the-art approaches for NRSfM problem typically impose prior constraints over the feature point distribution across image frames. These constraints can be viewed as different types of deformable models adopted for the final 3D reconstruction. The seminal work in this field was by Bregler et al. [2000] where correspondence across the video frames were factorized further into camera pose and 3D shape subspace to aid final reconstruction of 3D shape. This work was an analogous implementation of the factorization technique for SfM proposed by Tomasi and Kanade [1992]. Due to the inherent simplicity for implementation and robustness to noise, factorization methods, supported by singular value decomposition (SVD) (Akhter et al. [2009a]; Yan and Pollefeys [2008]; Bartoli et al. [2008]) have gained much attention. The underlying assumption exploited by this class of methods is that temporally related object deformation cannot be arbitrary across consecutive frames. Specialization of these methods have been proposed to recover shape data for articulated objects such as human model (Tresadern and Reid [2005]; Paladini et al. [2009]).

To facilitate shape recovery from non-rigid deformation under high spatial variance factorization based approach has been combined further with statistical(Torresani et al. [2008]), shape basis (Xiao et al. [2006]), 3D affine (Del Bue [2008]) priors. However, factorization based low rank shape basis model typically constraints the spatial variation of shape disregarding the temporal variation across frames. Solution due to Akhter et al. [2009b] tackled this limitation by discrete cosine transform (DCT) bases to represent the temporal variation sub-

space. In a related work Gotardo and Martinez [2011a] adopted a DCT based subspace model for camera pose to model the temporal variation. This approach was further extended by representing the shape space with radial basis functions to address more diverse deformations(Gotardo and Martinez [2011b]). Low frequency variation for the feature point trajectories across frames was modeled using DCT basis by Valmadre and Lucey [2012] to formulate a cost function that penalizes trajectory variation response to high pass filters. More recent advancement in the prior based approaches for NRSfM is proposed by Simon et al. [2017] where a Kronecker-Markov based prior constraining the temporal variation of a feature point was shown to perform very competitively over all the other state-of-the-art prior based approaches.

An alternative class of solutions for NRSfM problem employ physical models and associated constraints to achieve practical solution. A common practice within approaches of this class is to impose a rigidity constraint over the point distributions between frames. In this context Varol et al. [2009] apply a segmentation to the distribution and assume affine rigidity for each segmented patch. This limiting assumption is relaxed in Fayad et al. [2010] where a quadratic function is used to model each segmented patch. An alternative solution to this approach is due to Lee et al. [2016] where multiple solutions to 3D reconstruction from each segmented patch is further filtered by a computing a consensus between different patches. Apart from segmentation the rigidity constraint can also be imposed by assuming an underlying triangulation for feature point distributions across frames(Taylor et al. [2010]; Varol et al. [2009]). A geometric consistency

can be imposed between successive deformation across frames assuming isometric deformation where a distance metric over the temporally deformed surface across frames remain constant. Some important work from this class are proposed by Chhatkuli et al. [2014]; Parashar et al. [2017] that can address the reconstruction under missing data by exploiting differential geometry supported constraints for each segmented patch. Convex optimization based approaches proposed by Chhatkuli et al. [2017]; Vicente and Agapito [2012] imposes inextensibility on the patches to minimize a global energy term for shape deformation across frames. An extensive survey of these methods is given in Hoppe Nesgaard Jensen et al. [2018] along with a newly proposed benchmark for the NRSfM evaluation.

In the present work we explore a novel factorization method based solution combined with motion constraints imposed upon the deformable object to enhance accuracy of the final 3D shape reconstruction. In principle the proposed method combines statistical and physical model based assumptions to impose spatio-temporal constraint on the non-rigid deformation across frames. The proposed method impose triangulation over for 2D feature points and represents the distribution per frame by a pairwise geodesic distance matrix computed from the 2D data. We further decompose the distance based distribution into an equivalent spectral components. Finally, we combine the standard factorization (Bregler et al. [2000]) based statistical optimization term with the inter-frame spectral variation of the distribution shape priors to form our final optimization. Following principle of factorization based approach we assume gradual change in deformation. Furthermore, we do not assume independence of bases across frames unlike re-

lated methods by Bartoli et al. [2008]; Brandt et al. [2009]. Therefore, due to the imposed triangular structure over the point distribution the proposed method assumes local rigidity but at the same time the spectral structure allows for flexibility of the solution to address higher variability in spatial and temporal domain.

5.4 Solution Model

In this section we discuss the most salient components of the proposed NRSfM optimization framework. One of these components is the factorization supported subspace decomposition for the observation matrix. Due to the limitation of factorization to address NRSfM solution we further impose motion constraints over the 2D point distribution across frames by imposing a spectral structure over the points per frame.

5.4.1 Factorization for Empirical Subspace Solution

Given a video sequence consisting of F frames we construct a matrix $[W_t]_{2\times P}$ for all frames $1 \leq t \leq F$ with the rows representing P 2D points per frame. In this optimization framework the 2×3 camera model R_t is used for all frames along with matrix $[S_t]_{3\times P}$ that represents the hypothesized 3D locations for all 2D point samples per frame. Given this setting the observation matrix W is related to camera and shape spaces as given in eqn. (5.1).

$$W_{2F\times P} = \begin{bmatrix} W_1 \\ W_2 \\ \vdots \\ W_F \end{bmatrix} = U\Delta V^T = U\Delta^{\frac{1}{2}}\Delta^{\frac{1}{2}}V^T = \begin{bmatrix} R_1^1 & R_1^2 & \cdots & R_1^{3K} \\ \vdots & & & \\ R_F^1 & R_F^2 & \cdots & R_F^{3K} \end{bmatrix} \begin{bmatrix} S_1 \\ S_2 \\ \vdots \\ S_{3K} \end{bmatrix} \quad (5.1)$$

$$= R_{2F\times 3K} S_{3K\times P}$$

Equation 5.1 summarizes the principle of factorization widely used for the NRSfM solution. Observation matrix W comprised of 2D coordinates of P points across F frames of input image sequence is constructed by accumulating matrices W_ts across frames and as a consequence is of dimension $2F \times P$. This observation matrix is further decomposed using standard singular value decomposition (SVD) into unitary matrices U and V and diagonally dominant matrix Δ. Since U and V are unitary matrices their column vectors are orthonormal and therefore, span a solution subspace that factorizes observation matrix W. Conceptually, since 2D points observed within matrix W are actually the projections of 3D points through camera onto image plane, the subspaces spanned by U and V can be viewed to represent the camera and 3D shape spaces respectively. Subsequently, the solution for the observation can be represented by the column vectors of U and V acting as bases for these spaces. The combination of basis vectors are determined by the scales of diagonal matrix Δ. As shown in eqn. (5.1) the combination for basis vectors are represented by the terms $U\Delta^{\frac{1}{2}}$ and $\Delta^{\frac{1}{2}}V^T$ respectively to denote solution for camera and shape space.

For the camera model, we assume camera orthographic projection. In their seminal work on SfM Tomasi and Kanade [1992] showed that under orthography W has a rank 3. However, since for NRSfM the allowed deformation is non rigid, the assumption does not hold. As a consequence the standard assumption is to consider rank $3K$ instead of 3 that will give a solution space for camera and shape parameters with dimension $3K$. It is to be emphasized here that the number of basis shapes spanning the shape subspace is K, however, since each point of the 3D shape space have 3 coordinates, the rank of the final solution matrix is $3K$. This low rank shape space assumption follows from one of the earliest work by Bregler et al. [2000].

With this assumption of solution space of dimension $3K$ the subspaces R and S representing camera and shape spaces respectively will have K bases each. The weighted decomposition of R is shown in eqn. (5.1) using components R_f^i that represent i^{th} camera matrix solution for frame f. Subsequently, the solution for the 3D shape S is represented by S_is i.e. the P dimensional basis vectors with $1 \leq i \leq K$.

5.4.2 Motion constraint Model

Though factorization method mentioned in Section. 5.4.1 can give solution for NRSfM under very low variability of deformation it is limiting in most practical scenarios. The ill-posedness of the NRSfM problem where unknown variable space is larger than the control parameter space, to achieve a practical solution additional constraints are necessary. In this work we propose a motion constrained model that

is visually represented in Fig. 5.1. From the input image sequence we construct a standard Delaunay triangulation defined over the 2D corresponding points per frame. Based on the triangulation, the constraint model represents the point distribution at frame t by the pairwise distance computed between all P 2D feature points per frame. For a frame t this pairwise distance for all points is represented by the square matrix D_t of dimension $P \times P$.

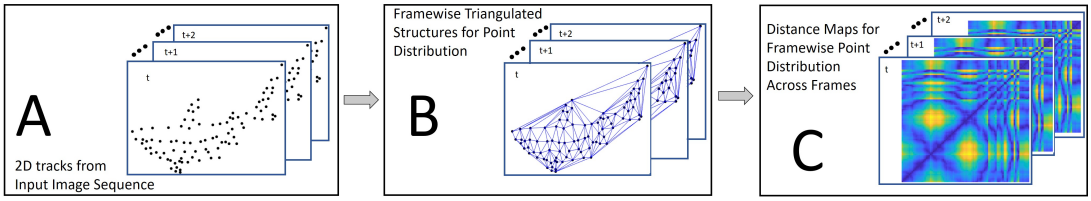

Figure 5.1: Model for motion constraint imposed over frame wise points distribution. The triangulation imposed in block B assumes rigidity constraints. However, the spectral distance maps shown in block C can be efficiently manipulated in the final optimization to address high spatial distribution variance caused from various degree of non-rigid deformation.

This distribution D_t for frame t is further decomposed using standard spectrum decomposition shown by eqn. (5.2) to obtain spectrum Ψ_t per frame. It is interesting to observe that both temporal distance representation D_t and its spectral equivalence Ψ_t exhibits symmetry as shown in Fig. 5.2 for different frames of the walking sequence. Therefore, the eigenvectors of Ψ_t at frame t can be used for spectral subspace representation for point distribution at frame t.

$$D_t \Psi_t = \Delta_t \Psi_t \tag{5.2}$$

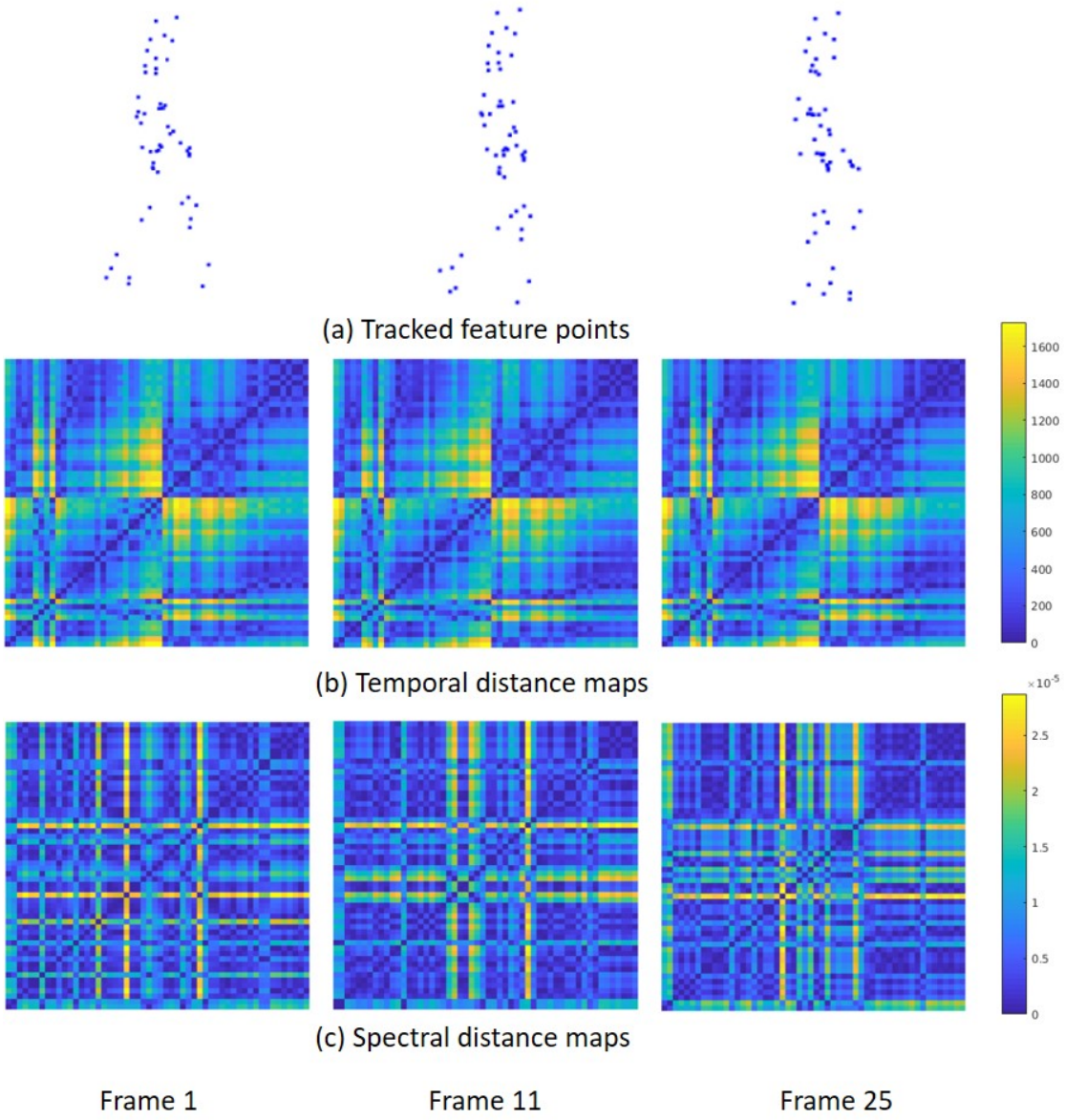

Figure 5.2: Visualization of distance maps computed for (a) image streams from walking data in (b) temporal and (c) spectral domain.

This observation is further extended to explore existing orthogonality of basis vectors across frames. The motivation behind this key observation is the hypoth-

esis that if there exists i^{th} and j^{th} candidate eigenvectors Ψ_{t-1}^{i} and Ψ_{t}^{j} between consecutive frames $t-1$ and t respectively such that the $\langle \Psi_{t-1}^{i} \cdot \Psi_{t}^{j} \rangle = 0$ or in other words they exhibits orthogonality between them then such combination of vectors span the solution subspace for spatio-temporal deformation across frames. This deformation is represented by the spatial variability of point distributions across frames. Some examples of such orthogonal candidates are mentioned in Table 5.1 those were obtained for the shark sequence from nrs [2004] dataset.

Table 5.1: Orthogonal eigenvector Candidates for shark sequence. The orthogonal candidates are from consecutive frames.

Frame t	Frame $t-1$	Vector index i from spectrum Ψ_t	Vector index j from spectrum Ψ_{t-1}	$\langle \Psi_t^i \cdot \Psi_{t-1}^j \rangle$
18	17	1	5	9.5×10^{-5}
		3	4	4.47×10^{-5}
		4	3	-7.2×10^{-5}
		5	1	-8.6×10^{-5}
19	18	1	3	-0.16×10^{-5}
		2	4	-9.87×10^{-5}
		3	1	1.69×10^{-5}
		4	2	7.86×10^{-5}

It is to be emphasized that the orthogonality measures in Table 5.1 are not exactly equal to zero due to the inherent noise within the point distributions, and the sparse point distribution considered for the experiments. Due to sparsity of the 2D points the error margin due to deformation between successive frames are higher. However, this setting also provides an opportunity to test the robustness of the proposed solution under noise as well. Another source of noise in the experiments

are due to the Delaunay triangulation that tend to add additional affine projected points to give the final triangulation a shape close to a convex hull. These points correspond to the yellow rows (and columns) of the spectral distance maps shown in Fig. 5.2(c). However, we report that the optimization proposed in this work can handle effect of such noisy artifacts and shows competitive performance for 3D reconstruction in comparison to the state-of-the-art methods.

Finally, we combine these matrices together to form the final cost function in eqn. (5.3) that optimizes the final 3D locations of the dynamic 2D points across the video frames. It is to be noted that we have also imposed the orthonormality constraint for camera model $R_t R_t^T = I$, $I_{2\times 2}$ being the identity matrix in the final optimization term in eqn. (5.3). This orthonormality constraint removes any affine Euclidean ambiguity and increase the accuracy of the final 3D reconstruction. The optimization solves the final reconstruction for a camera and shape subspace of dimension $3K$ as mentioned in the context of factorization in eqn. (5.1). We present the final optimization term in eqn. (5.3) as follows.

$$\begin{aligned} \underset{R_t, S_t, \bar{\Psi}_t}{\operatorname{argmin}} \sum_{t=1}^{F} ||W_t - R_t S_t||^2 + \gamma \sum_{t=2}^{F} |||[\bar{\Psi}_t] - [\bar{\Psi}_{t-1}]||^2 + ||\bar{\Psi}_t \bar{\Psi}_{t-1}^T - I_n|| \\ + \alpha \sum_{t=1}^{F} ||R_t R_t^T - I||^2 \end{aligned} \tag{5.3}$$

$$\sum_{\substack{i=1 \\ x_j \in N(x_i)}}^{p} ||\Psi_t^f(x_i, x_j) - \Psi_{t-1}^f(x_i, x_j)|| \leq \varepsilon \tag{5.4}$$

Constants γ, β and α in eqn. (5.3) are hyper-parameters used to regularize the final optimization. For the optimization the temporal orthogonality between consecutive frames is computed using the third component of eqn. (5.3) where $\bar{\Psi}_t \subset \Psi_t$. The term $\bar{\Psi}_t$ is computed by incrementally by adding candidate eigenvectors over successive iteration for both frames t and $t-1$. Parameter n denotes this incrementally varying size of $\bar{\Psi}_t$ and consequently I_n denotes identity matrix of order n to facilitate the temporal orthogonality check. In addition to the temporal orthogonality constraint we simultaneously minimize the norm difference between candidate spectrum vectors. In optimization 5.3 the term $[\bar{\Psi}_t]$ denotes the combined norm of spectral candidates at frame t.

The optimization in eqn. (5.3) is further subjected to a constraint that, 2D point distribution in one frame t satisfies the motion constraint mentioned in eqn. (5.4) where $N(x_i)$ is the neighborhood of point x_i. The term $\Psi_t^f(x_i, x_j)$ computes the difference of spectral component between points x_i and x_j at frame t where the distance between the points was computed using metric f. For our experiments the function f is a geodesic distance metric applied over the triangulation for frame t. It is to be noted that if we compute shortest distances between points considering point cloud data instead using a 2D triangulation then f would simply be Euclidean metric. Essentially, the constraint in eqn. (5.4) limits the spatial

deformation variance of corresponding points between consecutive frames using the spectral measure.

5.5 Results

To evaluate the proposed scheme 5.3 we have used a dataset from nrs [2004] with known ground truth. The video sequences in the dataset have $240 - 316$ frames per sequences. Our experiments considered walking, shark, face, cardboard, cloth, dance, and stretch sequences those vary in degrees of deformation expressed in terms of the temporal 2D correspondences. Some sample input 2D tracks for the shark sequence is shown in Fig. 5.3 where the corresponding points across different data sequence are shown to deform dynamically.

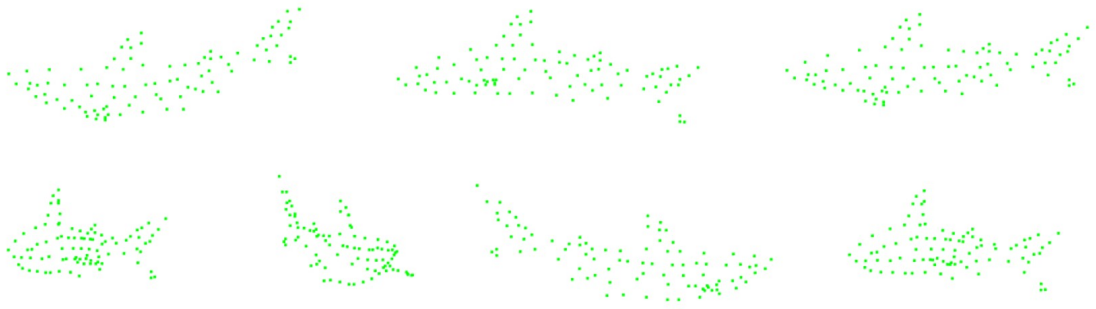

Figure 5.3: Sample input 2D track from the shark sequence nrs [2004] used for the experiments.

We present in Fig. 5.4 the 3D reconstruction results for shark sequence. The close proximity of the reconstructed result (in red) with the ground truth (in blue) suggests the effectiveness of the proposed optimization. It is to be emphasized here that the proposed solution does not consider dense trajectories between cor-

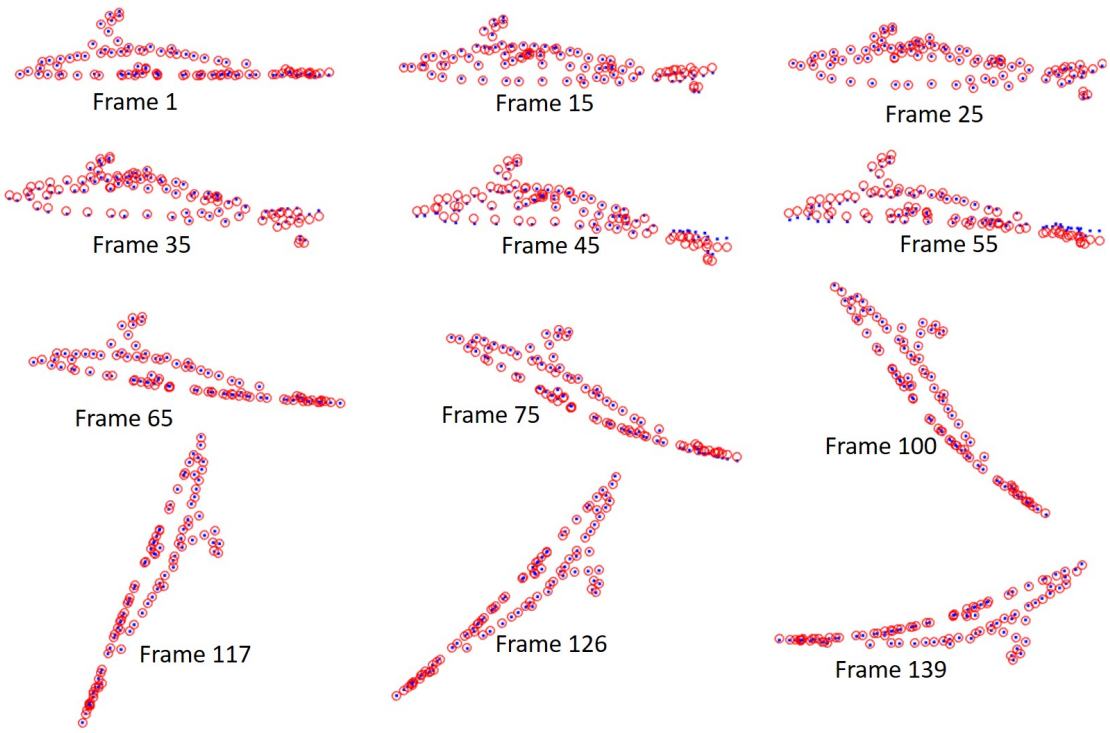

Figure 5.4: Performance of the proposed model on the shark sequence. 3D mapping error can be visualized by the discrepancy between ground truth (in blue) and the model output (in red).

responding points across frames. Furthermore, the motion constraint does not over constrain the solution space by assuming additional rigidity similar to relevant physical model based solutions.

To compare the performance quantitatively the 3D reconstruction result the following methods were chosen. These methods are referred to by their acronym hereafter.

MP: Metric Projection Method (Paladini et al. [2009])

Table 5.2: 3D mapping error for the shark, face and walking sequence in the CMU NRSfM database nrs [2004].

Sequence	MP	PTA	CSF	KSFM	IPCA	DM	TB	Proposed
Walking	0.4144	0.3948	0.1675	0.1029	0.3264	0.0265	0.3381	**0.1012**
Shark	0.4023	0.4012	0.1755	0.1821	0.1894	0.1318	0.1294	**0.1218**
Face	0.3988	0.3526	0.2855	0.2841	0.1894	**0.1318**	0.1294	0.1518
Cardboard	0.4185	0.2894	0.3237	0.2753	0.2445	0.1064	0.2131	0.1013
Cloth	0.3997	0.3526	0.2609	0.1806	0.1909	**0.0287**	0.2148	0.877
Dance	0.2210	0.2935	0.2684	0.2369	0.3058	0.1676	0.2548	**0.1045**
Stretch	0.3988	0.1087	0.0709	0.0736	0.1918	**0.0687**	0.2117	0.0718

PTA: Trajectory space model (Akhter et al. [2011])

CSF: Smooth Trajectory based model (Gotardo and Martinez [2011a])

KSFM: Kernel based NRSfM (Gotardo and Martinez [2011b])

IPCA: Incremental PCA (Tao et al. [2012])

DM: Diffusion prior based NRSfM model (Tao and Matuszewski [2013])

HP: Low rank matrix based factorization based NRSfM (Torresani et al. [2008])

The experiment considers the aforementioned sequences from nrs [2004] dataset. The performance comparison result is presented in Table 5.2 where the proposed method is shown to perform competitively well with the other state-of-the-art methods. Amongst other methods **DM**, **KSFM** and **TB** performs considerably well whereas the highest reconstruction error was obtained for method **MP** and **PTA**.

5.6 Conclusions

We proposed a solution to the problem of NRSfM by enforcing a constraint on the relative motion on the 2D point trajectories in addition to the low rank factorization based Tomasi and Kanade [1992]; Torresani et al. [2008] method. The proposed method is tested with different motion captured (MoCap) sequences and the performance in terms of final 3D reconstruction error is compared with relevant the state-of-the-art methods. The method is found to perform comparatively well.

We propose to extend the result to other available datasets under different noise condition to test the robustness of the proposed method. Further, we wish to extend the optimization criteria by utilizing the spectrum of the distance matrices D_t in addition to other suitable shape and/or trajectory priors to further increase the robustness of the method.

Chapter 6

Conclusions and Future Work

In this chapter we cite possible future directions for the frameworks proposed in each of the previous chapters.

6.1 Future Extension for Shape Representation

The driving motivation behind the shape representations proposed in Chapters 2 and 3 is to explore human ability behind shape recognition. The modality chosen to establish correspondence between shapes involved spectral techniques due to their implicit ability of abstraction that is robust to noise. Another technical advantage of spectral techniques is their compatibility with mathematical and functional mapping technique (Ovsjanikov et al. [2012]) that can lead to more general solutions for the shape correspondence problem. In future, we intend to combine the proposed mechanism with angle preserving conformal maps on shapes that can preserve the local geometric properties of shapes undergoing isometric

transformation.

In this dissertation we proposed a global shape representation scheme using quasi-geodesics computed over the entire discrete shape manifold. The eigen-spectral decomposition of this representation is used effectively to identify self-symmetric regions on the discrete shape manifold. By exploiting the commutative property of the eigenbases of the proposed representation, we successfully demonstrated its use in correspondence determination between isometric shapes. We also proposed characterization metrics for self-symmetry identification and correspondence determination. Furthermore, as associated applications of the proposed representations stable surface regions within 3D shapes were identified for shape pairs that differed from each other by a high degree of isometry deformation. The spectrum of the surface differential based shape representation was applied to address deformation transfer. Based on the spectrum of surface differential based representation we proposed a novel surface signature that is shown to perform better than the otherwise popular *Heat Kernel* or *Wave kernel* based signature. The results of correspondence determination obtained via the proposed representation scheme were compared with those from relevant state-of-the-art representation schemes and shown to perform competitively.

A key contribution of this work is the fact that no prior knowledge, in the form of user-specified mappings, was used for correspondence determination and self-symmetry detection. As an extension of the current scheme, we intend to explore and combine functional maps (Ovsjanikov et al. [2012]) based conformal mapping technique with the proposed representation that may prove critical in exploring

the group structure within isometric shapes. Furthermore, we intend to use this combined scheme to address correspondence determination between near-isometric shapes (Kovnatsky et al. [2013]). We briefly outline these possible extensions for shape correspondence in Section 6.1.1.

6.1.1 Functional Map based Shape Correspondence

A majority of existing spectral analysis methods for correspondence determination address the problem by limiting the search for correspondences between a small set of landmark points and extending the results to a dense set of correspondences defined on the entire 3D shape as a final post-processing step (Bronstein et al. [2006]; Huang et al. [2008]; Lipman and Funkhouser [2009]; Kin-Chung Au et al. [2010]; Ovsjanikov et al. [2010]; Kim et al. [2011]; Tevs et al. [2011]; Sahilliolu and Yemez [2011]). This strategy has also been justified theoretically, since under general conditions, a small set of landmark correspondences is known to be sufficient to obtain a unique dense mapping between isometric surfaces (Lipman and Funkhouser [2009]; Ovsjanikov et al. [2010]). Although this landmark-based approach reduces the complexity of the search through the solution space it still relies on representing shape maps as point-to-point correspondences. This makes it difficult to incorporate global constraints or return meaningful results when establishing point-to-point correspondences in the presence of coarse similarities or symmetry ambiguities. An alternative technique, namely functional maps has been demonstrated to be suitable for establishing correspondence between shapes in a fundamentally different manner. This technique first maps the spectrum of

candidate shapes to 2D real Euclidean space and subsequently establishes correspondence by extracting signatures corresponding to the shapes. Thus rather than establishing correspondence between points on the shapes, it proposes to compute mappings between functions defined over the shapes. This notion of correspondence generalizes the standard point-to-point correspondence map since every point-wise correspondence induces a mapping between function spaces, while the opposite, in general, is not true. However, this generalized representation is: (a) flexible, since it allows one to choose a basis for the function space on each 3D shape and consequently represent the mapping as a change of basis matrix and, (b) well-suited for shape matching, since many natural constraints on the point-to-point correspondence map become linear constraints under the functional map formulation. This representation works especially well when combined with the eigenfunctions of the Laplace-Beltrami operator, since it benefits from the multi-scale and geometry-aware nature of the eigenfunctions. This representation, in particular, achieves a state-of-the art results on an isometric shape matching benchmark which is essentially implemented using a single linear solve procedure. Functional maps are also suitable for segmentation transfer and joint analysis of shape collections without requiring one to establish point-to-point correspondences.

The functional map framework processes shapes as follows. First, it translates each 3D shape into a corresponding scalar function. Subsequently the correspondences between regions belonging to these shapes are represented as maps of functions. This framework addresses the problem of correspondence determination

between shapes when the deformation between shapes is within an addressable limit, i.e., shapes with approximate isometry. We briefly mention some of the mathematical foundation for functional map in Section 6.1.1).

Mathematical foundations of functional maps

In this section the functional map technique is discussed formally. Let M and N be two shape manifolds and let $T : M \rightarrow N$ be a bijective (one-to-one and onto) map between them. T being bijective naturally induces a transformation on surface points between these manifolds. Surface points are often expressed in terms of scalar functions over them. Lets consider two such derived scalar functions $f : M \rightarrow \mathbb{R}$ and $g : N \rightarrow \mathbb{R}$ defined over shapes M and N. Due to the existence of map T maps f and g would be related such that $g = f \circ T^{-1}$. The functional map T_F, represents a mapping between these two derived scalar functions, i.e., $T_F : f \rightarrow g$. Region specific mapping between shapes can be represented by functional map T_F. Functional maps can be further decomposed into spectrum where the functional space can be represented using eigenvectors $\{\varphi_i^M\}$ described over shape manifold M. eqn. (6.1) expresses the spectral decomposition.

$$T_F(f) = T_F\left(\sum_i a_i \varphi_i^M\right) = \sum_i a_i T_F(\varphi_i^M) \tag{6.1}$$

$T_F(\phi_i^M)$ can further be represented as combination of eigenbases $\{\varphi_i^N\}$ on the manifold N as $T_F(\varphi_i^M) = \sum_j c_{ij}\varphi_i^N$ giving us the final combined representation of

functional map T_F as given in eqn. (6.2).

$$T_F(f) = T_F\left(\sum_i a_i \varphi_i^M\right) = \sum_i a_i T_F(\varphi_i^M) = \sum_j \sum_i a_i c_{ij} \phi_j^N \tag{6.2}$$

Thus, if scalar function f defined for manifold M is represented as vector of coefficients $\mathbf{a} = (a_0, a_1, \ldots, a_i, \ldots)$ defined over each surface vertex and $g = T_F(f)$ is represented as a vector $\mathbf{b} = (b_0, b_1, \ldots, b_i, \ldots)$ then following the formal description given above, surface point j can be expressed as $b_j = \sum_i c_{ij} a_i$ where c_{ij} is independent of any choice of f. Formally, coefficient matrix $c_{ij} =< T_F(\varphi_i^M), \varphi_j^N >$ (where $< ., . >$ denotes the inner product of the vector arguments) would best describe mapping between manifold M and N in terms of relative weight matrix C_{ij} that represents the relationship between the eigenvectors defined on the manifolds M and N. Intuitively, it is within these weights that the geometric deformation-specific correspondence is encoded.

This flexible representation can be further extended for shapes with topological deformation where preservation of isometry between deformation may not be guaranteed. The proposed work on shape correspondence can be combined with functional maps to cover several important aspects of shape analysis listed as follows.

1. Independent spectral study of shape operators other than the Laplace-Beltrami operator with applications to 3D shape analysis. The resulting spectrum can be decomposed using standard techniques to yield a salient eigenbases for

shape representation.

2. Combining the principal eigenvectors of functional maps supported shape spectrum to construct surface features that could define robust shape descriptors on 3D shapes.

3. Study of persistent homology features for robust characterization of shapes under topological deformation. This study is aimed at tracking and/or estimating a specific region of a shape that has undergone various combinations of continuous or aberrant topological deformations.

6.1.2 Support of Conformal Mapping Based Techniques

Conformal map refers to mathematical mapping between objects such that a geometric measure at corresponding points between objects remain within bound or preferably same. Very often this measure is a geometric angle at corresponding points computed using standard mathematical mathematical techniques such as level sets. This angle preserving conformal map can be exploited to address global shape similarity a problem central to many computer graphics related applications. Following the shape representation presented in this work we intend to explore whether the representation spectrum can be combined with conformal map based techniques. Our motivation behind exploring this direction of study is to add a flexibility to the present framework so that correspondence between shape that varying from point-to-point to region wise correspondence can be performed using a unified mechanism. Some of the foundational works in the field of

conformal maps and its applications in vision and graphics were proposed by Gu et al. [2010]; Zeng et al. [2010].

6.1.3 Discovering Group Structure from Shape

One fundamental problem within computer vision and graphics is to retrieve repetitive structures from images and shapes. Examples of repetitive structure could be motifs within an image, regions with similar textures, pose of a shape models etc that can be employed for different applications such as discovering skewed symmetry within images, statistical bilateral structure, human gait analysis etc. to name a few.

This class of applications need to consider robust feature detection over images or shapes that remain invariant under topological transformations. Topological transformations in computer vision and graphics have been addressed using specialized groups structures such as Lie group (Murray [2017]; Huang et al. [2017]), symmetry groups(Liu et al. [2010]) etc. However, topological data analysis is a newly emerging field that aims at extracting features those are topology invariant from more noisy data such as geometric point cloud data scanned from 3D sensors. Being topology independent these feature are very robust to noise and can provide state-of-the-art solution for problems such as correspondence under various geometry, noise and topology transformation. We intend to combine the spectral framework based correspondence method proposed in this dissertation with conformal maps mentioned in Section 6.1.2 to extract robust shape features to produce advanced results in correspondence between shapes under a wide ranges

of transformation varying in principle and degree.

6.2 Non-Rigid Structure from Motion

For estimation of 3D point information from 2D stream of images we proposed a solution to the problem of NRSfM in Chapter 5, that finds a solution by enforcing a constraint on the relative motion on the 2D point trajectories in addition to the low rank factorization based method (Tomasi and Kanade [1992]; Torresani et al. [2008]). The proposed method is tested with different motion captured (MoCap) sequences and the performance in terms of final 3D reconstruction error is compared with relevant the state-of-the-art methods. The method is found to perform comparatively well.

In summery this proposed method is not explicitly trained on NRSfM datasets. Rather the solution fits a spectral model by assuming gradual deformation between frames that is realistic under practical scenario. However, the spectral decomposition of the distance maps helps converge the solution using subspace representation for camera and shape spaces. The spectral parametric control for the final solution, therefore, does not over constrain the solution space by imposing the hard rigidity assumption. We intend to explore this flexibility provided be this solution in future to propose a learning model with state-of-the-art databases along the lines of Hoppe Nesgaard Jensen et al. [2018]. We initially expect to run into issues regarding hyper-parameter tuning for the learning model. However, this apparent disadvantage can simultaneously provide opportunity to explore further

the robustness of spectral subspace representation for the NRSfM solution space.

Bibliography

Oliver Van Kaick, Hao Zhang, Ghassan Hamarneh, and Daniel Cohen-Or. A survey on shape correspondence. *Computer Graphics Forum*, 30(6):1681–1707, 2011a.

Robert W Sumner, Matthias Zwicker, Craig Gotsman, and Jovan Popović. Mesh-based inverse kinematics. *ACM transactions on graphics (TOG)*, 24(3):488–495, 2005.

Nrsfm cmu data, 2004. URL `http://www.cs.dartmouth.edu/~lorenzo/nrsfm.html`.

Vladimir G Kim, Yaron Lipman, and Thomas Funkhouser. Blended intrinsic maps. *ACM Transactions on Graphics (TOG)*, 30(4):79:1–79:12, 2011.

Y Sahillioglu and Yücel Yemez. Coarse-to-fine combinatorial matching for dense isometric shape correspondence. *Computer Graphics Forum*, 30(5):1461–1470, 2011.

Maks Ovsjanikov, Mirela Ben-Chen, Justin Solomon, Adrian Butscher, and Leonidas Guibas. Functional maps: a flexible representation of maps between shapes. *ACM Transactions on Graphics (TOG)*, 31(4):30, 2012.

Somenath Das and Suchendra M Bhandarkar. Local geometry inclusive global shape representation. *Proceedings of IEEE International Conference on Computer Vision Workshops (ICCV Workshops)*, pages 1256–1265, 2017.

Somenath Das and Suchendra M. Bhandarkar. Principal curvature guided surface geometry aware global shape representation. In *The IEEE Conference on Computer Vision and Pattern Recognition (CVPR) Workshops*, pages 403–412, June 2018.

Maks Ovsjanikov, Quentin Mérigot, Facundo Mémoli, and Leonidas Guibas. One point isometric matching with the heat kernel. In *Computer Graphics Forum*, volume 29, pages 1555–1564. Wiley Online Library, 2010.

Mathieu Aubry, Ulrich Schlickewei, and Daniel Cremers. The wave kernel signature: A quantum mechanical approach to shape analysis. *Proceedings of IEEE International Conference on Computer Vision Workshops (ICCV Workshops)*, pages 1626–1633, 2011.

Paul Heider, Alain Pierre-Pierre, Ruosi Li, and Cindy Grimm. Local shape descriptors, a survey and evaluation. In *Proceedings of the 4th Eurographics Conference on 3D Object Retrieval*, 3DOR '11, pages 49–56, Aire-la-Ville, Switzerland, Switzerland, 2011a. Eurographics Association. ISBN 978-3-905674-31-6. doi: 10.2312/3DOR/3DOR11/049-056. URL `http://dx.doi.org/10.2312/3DOR/3DOR11/049-056`.

Evangelos Kalogerakis, Aaron Hertzmann, and Karan Singh. Learning 3d mesh

segmentation and labeling. *ACM Transactions on Graphics (TOG)*, 29(4):102, 2010.

Oliver Van Kaick, Andrea Tagliasacchi, Oana Sidi, Hao Zhang, Daniel Cohen-Or, Lior Wolf, and Ghassan Hamarneh. Prior knowledge for part correspondence. In *Computer Graphics Forum*, volume 30, pages 553–562. Wiley Online Library, 2011b.

Szymon Rusinkiewicz and Marc Levoy. Efficient variants of the icp algorithm. In *3-D Digital Imaging and Modeling, 2001. Proceedings. Third International Conference on*, pages 145–152. IEEE, 2001.

Dragomir Anguelov, Praveen Srinivasan, Hoi-Cheung Pang, Daphne Koller, Sebastian Thrun, and James Davis. The correlated correspondence algorithm for unsupervised registration of nonrigid surfaces. In *Advances in neural information processing systems*, pages 33–40, 2005.

Varun Jain, Hao Zhang, and Oliver van Kaick. Non-rigid spectral correspondence of triangle meshes. *International Journal of Shape Modeling*, 13(01):101–124, 2007.

Benedict J Brown and Szymon Rusinkiewicz. Global non-rigid alignment of 3-d scans. In *ACM Transactions on Graphics (TOG)*, volume 26, page 21. ACM, 2007.

Will Chang and Matthias Zwicker. Automatic registration for articulated shapes. *Computer Graphics Forum*, 27(5):1459–1468, 2008.

Qi-Xing Huang, Bart Adams, Martin Wicke, and Leonidas J Guibas. Non-rigid registration under isometric deformations. In *Computer Graphics Forum*, volume 27, pages 1449–1457. Wiley Online Library, 2008.

Marc Alexa. Recent advances in mesh morphing. In *Computer graphics forum*, volume 21, pages 173–198. Wiley Online Library, 2002.

Vladislav Kraevoy and Alla Sheffer. Cross-parameterization and compatible remeshing of 3D models. *ACM Transactions on Graphics (TOG)*, 23(3):861–869, 2004.

Aleksey Golovinskiy, Joshua Podolak, and Thomas Funkhouser. Symmetry-aware mesh processing. In *IMA International Conference on Mathematics of Surfaces*, pages 170–188. Springer, 2009.

Niloy J Mitra, Leonidas J Guibas, and Mark Pauly. Partial and approximate symmetry detection for 3d geometry. *ACM Transactions on Graphics (TOG)*, 25(3):560–568, 2006.

Joshua Podolak, Philip Shilane, Aleksey Golovinskiy, Szymon Rusinkiewicz, and Thomas Funkhouser. A planar-reflective symmetry transform for 3d shapes. *ACM Transactions on Graphics (TOG)*, 25(3):549–559, 2006.

Kai Xu, Hao Zhang, Andrea Tagliasacchi, Ligang Liu, Guo Li, Min Meng, and Yueshan Xiong. Partial intrinsic reflectional symmetry of 3d shapes. In *ACM Transactions on Graphics (TOG)*, volume 28, page 138. ACM, 2009.

Vladimir G Kim, Yaron Lipman, Xiaobai Chen, and Thomas Funkhouser. Möbius transformations for global intrinsic symmetry analysis. In *Computer Graphics Forum*, volume 29, pages 1689–1700. Wiley Online Library, 2010.

Maks Ovsjanikov, Jian Sun, and Leonidas Guibas. Global intrinsic symmetries of shapes. In *Computer graphics forum*, volume 27, pages 1341–1348. Wiley Online Library, 2008.

Yaron Lipman, Xiaobai Chen, Ingrid Daubechies, and Thomas Funkhouser. Symmetry factored embedding and distance. In *ACM Transactions on Graphics (TOG)*, volume 29, page 103. ACM, 2010a.

Kai Xu, Honghua Li, Hao Zhang, Daniel Cohen-Or, Yueshan Xiong, and Zhi-Quan Cheng. Style-content separation by anisotropic part scales. In *ACM Transactions on Graphics (TOG)*, volume 29, page 184. ACM, 2010.

Huong Quynh Dinh, Anthony Yezzi, and Greg Turk. Texture transfer during shape transformation. *ACM Transactions on Graphics (TOG)*, 24(2):289–310, 2005.

David A Forsyth and Jean Ponce. A modern approach. *Computer vision: a modern approach*, pages 88–101, 2003.

Thomas Funkhouser and Philip Shilane. Partial matching of 3 d shapes with priority-driven search. In *ACM International conference proceeding series*, volume 256, pages 131–142. Citeseer, 2006.

Niloy J Mitra, Simon Flöry, Maks Ovsjanikov, Natasha Gelfand, Leonidas J

Guibas, and Helmut Pottmann. Dynamic geometry registration. In *Symposium on geometry processing*, pages 173–182, 2007.

Michael Wand, Philipp Jenke, Qixing Huang, Martin Bokeloh, Leonidas Guibas, and Andreas Schilling. Reconstruction of deforming geometry from time-varying point clouds. In *Symposium on Geometry processing*, pages 49–58. Citeseer, 2007.

Andrei Sharf, Dan A Alcantara, Thomas Lewiner, Chen Greif, Alla Sheffer, Nina Amenta, and Daniel Cohen-Or. Space-time surface reconstruction using incompressible flow. *ACM Transactions on Graphics (TOG)*, 27(5):110, 2008.

Yuri Pekelny and Craig Gotsman. Articulated object reconstruction and markerless motion capture from depth video. *Computer Graphics Forum*, 27(2): 399–408, 2008.

Hao Li, Bart Adams, Leonidas J Guibas, and Mark Pauly. Robust single-view geometry and motion reconstruction. In *ACM Transactions on Graphics (TOG)*, volume 28, page 175. ACM, 2009.

Will Chang and Matthias Zwicker. Range scan registration using reduced deformable models. In *Computer Graphics Forum*, volume 28, pages 447–456. Wiley Online Library, 2009.

Art Tevs, Martin Bokeloh, Michael Wand, Andreas Schilling, and Hans-Peter Seidel. Isometric registration of ambiguous and partial data. In *Computer Vision*

and Pattern Recognition, 2009. CVPR 2009. IEEE Conference on, pages 1185–1192. IEEE, 2009.

Qian Zheng, Andrei Sharf, Andrea Tagliasacchi, Baoquan Chen, Hao Zhang, Alla Sheffer, and Daniel Cohen-Or. Consensus skeleton for non-rigid space-time registration. In *Computer Graphics Forum*, volume 29, pages 635–644. Wiley Online Library, 2010.

Hengameh Mirzaalian, Ghassan Hamarneh, and Tim K Lee. A graph-based approach to skin mole matching incorporating template-normalized coordinates. 2009.

Yvan G Leclerc, Q-T Luong, Pascal V Fua, and Koji Miyajima. Detecting changes in 3-d shape using self-consistency. In *Computer Vision and Pattern Recognition, 2000. Proceedings. IEEE Conference on*, volume 1, pages 395–402. IEEE, 2000.

Rhodri Davies, Carole Twining, and Chris Taylor. *Statistical models of shape: Optimisation and evaluation*. Springer Science & Business Media, 2008.

Nils Hasler, Carsten Stoll, Martin Sunkel, Bodo Rosenhahn, and H-P Seidel. A statistical model of human pose and body shape. In *Computer Graphics Forum*, volume 28, pages 337–346. Wiley Online Library, 2009.

Aaron Ward and Ghassan Hamarneh. Statistical shape modeling using mdl incorporating shape, appearance, and expert knowledge. *Medical Image Computing and Computer-Assisted Intervention–MICCAI 2007*, pages 278–285, 2007.

Michela Mortara, Giuseppe Patané, Michela Spagnuolo, Bianca Falcidieno, and Jarek Rossignac. Blowing bubbles for multi-scale analysis and decomposition of triangle meshes. *Algorithmica*, 38(1):227–248, 2004.

Helmut Pottmann, Johannes Wallner, Qi-Xing Huang, and Yong-Liang Yang. Integral invariants for robust geometry processing. *Computer Aided Geometric Design*, 26(1):37–60, 2009a.

Timothy Gatzke, Cindy Grimm, Michael Garland, and Steve Zelinka. Curvature maps for local shape comparison. *Proceedings of the International Conference on Shape Modeling and Applications*, pages 244–253, 2005.

Fridtjof Stein and Gérard Medioni. Structural indexing: Efficient 3-D object recognition. *IEEE Transactions on Pattern Analysis & Machine Intelligence*, (2): 125–145, 1992.

Ju Lynn Ong and Abd-Krim Seghouane. From point to local neighborhood: polyp detection in ct colonography using geodesic ring neighborhoods. *IEEE Transactions on Image Processing*, 20(4):1000–1010, 2011a.

Sameh M Yamany and Aly A Farag. Free-form surface registration using surface signatures. *The Proceedings of the Seventh IEEE International Conference on Computer Vision*, 2:1098–1104, 1999.

Chin Seng Chua and Ray Jarvis. Point signatures: A new representation for 3D object recognition. *International Journal of Computer Vision*, 25(1):63–85, 1997.

Sameh M Yamany and Aly A Farag. Surface signatures: an orientation independent free-form surface representation scheme for the purpose of objects registration and matching. *IEEE Transactions on Pattern Analysis and Machine Intelligence*, 24(8):1105–1120, 2002.

J.L. Ong and A.-K. Seghouane. From point to local neighborhood: Polyp detection in ct colonography using geodesic ring neighborhoods. *IEEE Transactions on Image Processing*, 20(4):1000–1010, April 2011b. ISSN 1057-7149. doi: 10.1109/TIP.2010.2076295.

Gregory Cipriano, George N Phillips, and Michael Gleicher. Multi-scale surface descriptors. *IEEE Transactions on Visualization and Computer Graphics*, 15 (6):1201–1208, 2009.

Michael L Connolly. Measurement of protein surface shape by solid angles. *Journal of Molecular Graphics*, 4(1):3–6, 1986.

Helmut Pottmann, Johannes Wallner, Qi-Xing Huang, and Yong-Liang Yang. Integral invariants for robust geometry processing. *Computer Aided Geometric Design*, 26(1):37–60, 2009b.

Xinju Li and Igor Guskov. Multiscale features for approximate alignment of point-based surfaces. *Proceedings of Symposium on Geometry Processing*, 255:217–226, 2005.

Chang Ha Lee, Amitabh Varshney, and David W. Jacobs. Mesh saliency. *ACM Transactions on Graphics (TOG)*, 24(3):659–666, July 2005. ISSN 0730-0301.

doi: 10.1145/1073204.1073244. URL http://doi.acm.org/10.1145/1073204.1073244.

Alexander M Bronstein, Michael M Bronstein, Ron Kimmel, Mona Mahmoudi, and Guillermo Sapiro. A Gromov-Hausdorff framework with diffusion geometry for topologically-robust non-rigid shape matching. *International Journal of Computer Vision*, 89(2-3):266–286, 2010.

Raif M Rustamov. Laplace-Beltrami eigenfunctions for deformation invariant shape representation. *Proceedings of the Fifth Eurographics Symposium on Geometry Processing*, pages 225–233, 2007.

Dirk Smeets, Jeroen Hermans, Dirk Vandermeulen, and Paul Suetens. Isometric deformation invariant 3D shape recognition. *Pattern Recognition*, 45(7):2817–2831, 2012.

Jian Sun, Maks Ovsjanikov, and Leonidas Guibas. A concise and provably informative multi-scale signature based on heat diffusion. *Computer Graphics Forum*, 28(5):1383–1392, 2009.

Michael M Bronstein and Iasonas Kokkinos. Scale-invariant heat kernel signatures for non-rigid shape recognition. *Proceedings of IEEE Conference on Computer Vision and Pattern Recognition (CVPR)*, pages 1704–1711, 2010.

Davide Boscaini, Jonathan Masci, Emanuele Rodolà, Michael M Bronstein, and Daniel Cremers. Anisotropic diffusion descriptors. *Computer Graphics Forum*, 35(2):431–441, 2016.

Christoph Bregler, Aaron Hertzmann, and Henning Biermann. Recovering non-rigid 3d shape from image streams. In *Computer Vision and Pattern Recognition, 2000. Proceedings. IEEE Conference on*, volume 2, pages 690–696. IEEE, 2000.

Ijaz Akhter, Yaser Sheikh, and Sohaib Khan. In defense of orthonormality constraints for nonrigid structure from motion. 2009a.

Jingyu Yan and Marc Pollefeys. A factorization-based approach for articulated nonrigid shape, motion and kinematic chain recovery from video. *IEEE Transactions on Pattern Analysis and Machine Intelligence*, 30(5):865–877, 2008.

Adrien Bartoli, Vincent Gay-Bellile, Umberto Castellani, Julien Peyras, Søren Olsen, and Patrick Sayd. Coarse-to-fine low-rank structure-from-motion. In *Computer Vision and Pattern Recognition, 2008. CVPR 2008. IEEE Conference on*, pages 1–8. IEEE, 2008.

Phil Tresadern and Ian Reid. Articulated structure from motion by factorization. In *Computer Vision and Pattern Recognition, 2005. CVPR 2005. IEEE Computer Society Conference on*, volume 2, pages 1110–1115. IEEE, 2005.

Marco Paladini, Alessio Del Bue, Marko Stosic, Marija Dodig, Joao Xavier, and Lourdes Agapito. Factorization for non-rigid and articulated structure using metric projections. In *Computer Vision and Pattern Recognition, 2009. CVPR 2009. IEEE Conference on*, pages 2898–2905. IEEE, 2009.

Lorenzo Torresani, Aaron Hertzmann, and Chris Bregler. Nonrigid structure-from-

motion: Estimating shape and motion with hierarchical priors. *IEEE transactions on pattern analysis and machine intelligence*, 30(5):878–892, 2008.

Jing Xiao, Jinxiang Chai, and Takeo Kanade. A closed-form solution to non-rigid shape and motion recovery. *International Journal of Computer Vision*, 67(2): 233–246, 2006.

Alessio Del Bue. A factorization approach to structure from motion with shape priors. In *Computer Vision and Pattern Recognition, 2008. CVPR 2008. IEEE Conference on*, pages 1–8. IEEE, 2008.

Natasha Gelfand, Niloy J Mitra, Leonidas J Guibas, and Helmut Pottmann. Robust global registration. *Symposium on Geometry Processing*, 2(3):5, 2005.

Ran Gal and Daniel Cohen-Or. Salient geometric features for partial shape matching and similarity. *ACM Transactions on Graphics (TOG)*, 25(1):130–150, 2006.

Robert W Sumner and Jovan Popović. Deformation transfer for triangle meshes. *ACM Transactions on Graphics (TOG)*, 23(3):399–405, 2004.

Varun Jain and Hao Zhang. A spectral approach to shape-based retrieval of articulated 3D models. *Computer Aided Design*, 39(5):398–407, 2007.

Dimas Martínez, Luiz Velho, and Paulo C Carvalho. Computing geodesics on triangular meshes. *Computers & Graphics*, 29(5):667–675, 2005.

Artiom Kovnatsky, Michael M Bronstein, Alexander M Bronstein, Klaus Glashoff, and Ron Kimmel. Coupled quasi-harmonic bases. *Computer Graphics Forum*, 32(2pt4):439–448, 2013.

Paul Heider, Alain Pierre-Pierre, Ruosi Li, and Cindy Grimm. Local shape descriptors, a survey and evaluation. *Proceedings of the 4th Eurographics Conference on 3D Object Retrieval*, pages 49–56, 2011b. doi: 10.2312/3DOR/3DOR11/049-056. URL http://dx.doi.org/10.2312/3DOR/3DOR11/049-056.

Iasonas Kokkinos, Michael M Bronstein, Roee Litman, and Alex M Bronstein. Intrinsic shape context descriptors for deformable shapes. *Proceedings of IEEE Conference on Computer Vision and Pattern Recognition (CVPR)*, pages 159–166, 2012.

Blake C Lucas, Michael Kazhdan, and Russell H Taylor. Spring level sets: A deformable model representation to provide interoperability between meshes and level sets. *IEEE Transactions on Visualization and Computer Graphics*, 19(5): 852–865, 2013.

Jean-Fran Cois Cardoso. Perturbation of joint diagonalizers. 1995.

Arie Yeredor. Non-orthogonal joint diagonalization in the least-squares sense with application in blind source separation. *IEEE Transactions on Signal Processing*, 50(7):1545–1553, 2002.

Artiom Kovnatsky, Michael M Bronstein, Xavier Bresson, and Pierre Vandergheynst. Functional correspondence by matrix completion. *Proceedings of the IEEE Conference on Computer Vision and Pattern Recognition (CVPR)*, pages 905–914, 2015.

Mark Meyer, Mathieu Desbrun, Peter Schröder, and Alan H Barr. Discrete

differential-geometry operators for triangulated 2-manifolds. *Visualization and Mathematics III*, pages 35–57, 2003.

Omri Azencot, Steffen Weißmann, Maks Ovsjanikov, Max Wardetzky, and Mirela Ben-Chen. Functional fluids on surfaces. *Computer Graphics Forum*, 33:237–246, 2014.

Janick Martinez Esturo, Christian Rössl, and Holger Theisel. Smoothed quadratic energies on meshes. *ACM Transactions on Graphics (TOG)*, 34(1):2, 2014.

Nelson Dunford and Jacob T Schwartz. *Linear operators: Part II: Spectral Theory: Self Adjoint Operators in Hilbert Space*. Interscience Publishers, 1963.

Andy Nguyen, Mirela Ben-Chen, Katarzyna Welnicka, Yinyu Ye, and Leonidas Guibas. An optimization approach to improving collections of shape maps. *Computer Graphics Forum*, 30:1481–1491, 2011.

Maks Ovsjanikov, Alexander M Bronstein, Michael M Bronstein, and Leonidas J Guibas. Shape Google: a computer vision approach to isometry invariant shape retrieval. pages 320–327, 2009.

Bruno Lévy. Laplace-beltrami eigenfunctions towards an algorithm that " understands" geometry. In *Shape Modeling and Applications, 2006. SMI 2006. IEEE International Conference on*, pages 13–13. IEEE, 2006.

Gerard Pons-Moll, Javier Romero, Naureen Mahmood, and Michael J Black. Dyna: A model of dynamic human shape in motion. *ACM Transactions on Graphics (TOG)*, 34(4):120, 2015.

Michael Zollhöfer, Matthias Nießner, Shahram Izadi, Christoph Rehmann, Christopher Zach, Matthew Fisher, Chenglei Wu, Andrew Fitzgibbon, Charles Loop, Christian Theobalt, et al. Real-time non-rigid reconstruction using an rgb-d camera. *ACM Transactions on Graphics (TOG)*, 33(4):156, 2014.

Anirban Mukhopadhyay and Suchendra M Bhandarkar. Biharmonic density estimate: a scale-space descriptor for 3-d deformable surfaces. *Pattern Analysis and Applications*, 20(4):1261–1273, 2017.

Yaron Lipman, Raif Rustamov, and Thomas Funkhouser. Biharmonic distance. *ACM Transactions on Graphics*, 29(3), June 2010b.

Deformation transfer for triangle meshes, 2004. URL `http://people.csail.mit.edu/sumner/research/deftransfer/`.

Deformation transfer matlab, 2018. URL `https://github.com/SuwoongHeo/Deformation-Transfer-Matlab`.

Carlo Tomasi and Takeo Kanade. Shape and motion from image streams under orthography: a factorization method. *International Journal of Computer Vision*, 9(2):137–154, 1992.

Kyle Wilson and Noah Snavely. Robust global translations with 1dsfm. In *European Conference on Computer Vision*, pages 61–75. Springer, 2014.

David Crandall, Andrew Owens, Noah Snavely, and Dan Huttenlocher. Discrete-continuous optimization for large-scale structure from motion. In *Computer Vi-*

sion and Pattern Recognition (CVPR), 2011 IEEE Conference on, pages 3001–3008. IEEE, 2011.

Lili Tao, Bogdan J Matuszewski, and Stephen J Mein. Non-rigid structure from motion with incremental shape prior. In *Image Processing (ICIP), 2012 19th IEEE International Conference on*, pages 1753–1756. IEEE, 2012.

Lili Tao and Bogdan J Matuszewski. Non-rigid structure from motion with diffusion maps prior. In *Computer Vision and Pattern Recognition (CVPR), 2013 IEEE Conference on*, pages 1530–1537. IEEE, 2013.

Ijaz Akhter, Yaser Sheikh, Sohaib Khan, and Takeo Kanade. Trajectory space: A dual representation for nonrigid structure from motion. *IEEE Transactions on Pattern Analysis and Machine Intelligence*, 33(7):1442–1456, 2011.

Paulo FU Gotardo and Aleix M Martinez. Computing smooth time trajectories for camera and deformable shape in structure from motion with occlusion. *IEEE Transactions on Pattern Analysis and Machine Intelligence*, 33(10):2051–2065, 2011a.

Ijaz Akhter, Yaser Sheikh, Sohaib Khan, and Takeo Kanade. Nonrigid structure from motion in trajectory space. In *Advances in neural information processing systems*, pages 41–48, 2009b.

Paulo FU Gotardo and Aleix M Martinez. Kernel non-rigid structure from motion. In *Computer Vision (ICCV), 2011 IEEE International Conference on*, pages 802–809. IEEE, 2011b.

Jack Valmadre and Simon Lucey. General trajectory prior for non-rigid reconstruction. In *Computer Vision and Pattern Recognition (CVPR), 2012 IEEE Conference on*, pages 1394–1401. IEEE, 2012.

Tomas Simon, Jack Valmadre, Iain Matthews, and Yaser Sheikh. Kronecker-markov prior for dynamic 3d reconstruction. *IEEE transactions on pattern analysis and machine intelligence*, 39(11):2201–2214, 2017.

Aydin Varol, Mathieu Salzmann, Engin Tola, and Pascal Fua. Template-free monocular reconstruction of deformable surfaces. In *Computer Vision, 2009 IEEE 12th International Conference on*, pages 1811–1818. IEEE, 2009.

João Fayad, Lourdes Agapito, and Alessio Del Bue. Piecewise quadratic reconstruction of non-rigid surfaces from monocular sequences. In *European conference on computer vision*, pages 297–310. Springer, 2010.

Minsik Lee, Jungchan Cho, and Songhwai Oh. Consensus of non-rigid reconstructions. In *Proceedings of the IEEE Conference on Computer Vision and Pattern Recognition*, pages 4670–4678, 2016.

Jonathan Taylor, Allan D Jepson, and Kiriakos N Kutulakos. *Non-rigid structure from locally-rigid motion*. IEEE, 2010.

Ajad Chhatkuli, Daniel Pizarro, and Adrien Bartoli. Non-rigid shape-from-motion for isometric surfaces using infinitesimal planarity. In *BMVC*, 2014.

Shaifali Parashar, Daniel Pizarro, and Adrien Bartoli. Isometric non-rigid shape-

from-motion with riemannian geometry solved in linear time. *IEEE transactions on pattern analysis and machine intelligence*, 2017.

Ajad Chhatkuli, Daniel Pizarro, Toby Collins, and Adrien Bartoli. Inextensible non-rigid structure-from-motion by second-order cone programming. *IEEE transactions on pattern analysis and machine intelligence*, pages 1–1, 2017.

Sara Vicente and Lourdes Agapito. Soft inextensibility constraints for template-free non-rigid reconstruction. In *European conference on computer vision*, pages 426–440. Springer, 2012.

Sebastian Hoppe Nesgaard Jensen, Alessio Del Bue, Mads Emil Brix Doest, and Henrik Aanæs. A benchmark and evaluation of non-rigid structure from motion. *arXiv preprint arXiv:1801.08388*, 2018.

Sami S Brandt, Pekka Koskenkorva, Juho Kannala, and Anders Heyden. Uncalibrated non-rigid factorisation with automatic shape basis selection. In *Computer Vision Workshops (ICCV Workshops), 2009 IEEE 12th International Conference on*, pages 352–359. IEEE, 2009.

Alexander M Bronstein, Michael M Bronstein, and Ron Kimmel. Generalized multidimensional scaling: a framework for isometry-invariant partial surface matching. *Proceedings of the National Academy of Sciences of the United States of America*, 103(5):1168–1172, 2006.

Yaron Lipman and Thomas Funkhouser. Möbius voting for surface correspondence. In *ACM Transactions on Graphics (TOG)*, volume 28, page 72. ACM, 2009.

Oscar Kin-Chung Au, Chiew-Lan Tai, Daniel Cohen-Or, Youyi Zheng, and Hongbo Fu. Electors voting for fast automatic shape correspondence. In *Computer Graphics Forum*, volume 29, pages 645–654. Wiley Online Library, 2010.

Art Tevs, Alexander Berner, Michael Wand, Ivo Ihrke, and H-P Seidel. Intrinsic shape matching by planned landmark sampling. In *Computer Graphics Forum*, volume 30, pages 543–552. Wiley Online Library, 2011.

Y Sahilliolu and Yücel Yemez. Coarse-to-fine combinatorial matching for dense isometric shape correspondence. *Computer Graphics Forum*, 30(5):1461–1470, 2011.

David Xianfeng Gu, Feng Luo, and Shing-Tung Yau. Fundamentals of computational conformal geometry. *Mathematics in Computer Science*, 4(4):389, 2010.

Wei Zeng, Dimitris Samaras, and David Gu. Ricci flow for 3d shape analysis. *IEEE Transactions on Pattern Analysis and Machine Intelligence*, 32(4):662–677, 2010.

Richard M Murray. *A mathematical introduction to robotic manipulation*. CRC press, 2017.

Zhiwu Huang, Chengde Wan, Thomas Probst, and Luc Van Gool. Deep learning on lie groups for skeleton-based action recognition. In *Proceedings of the 2017 IEEE Conference on Computer Vision and Pattern Recognition (CVPR)*, pages 1243–1252. IEEE computer Society, 2017.

Yanxi Liu, Hagit Hel-Or, Craig S Kaplan, Luc Van Gool, et al. Computational symmetry in computer vision and computer graphics. *Foundations and Trends® in Computer Graphics and Vision*, 5(1–2):1–195, 2010.